Performance of ordered and disordered nanoporous metals

Punzhin, Sergey

rijksuniversiteit groningen

PERFORMANCE OF ORDERED AND DISORDERED NANOPOROUS METALS

Proefschrift

ter verkrijging van het doctoraat in de
Wiskunde en Natuurwetenschappen
aan de Rijksuniversiteit Groningen
op gezag van de
Rector Magnificus, dr. E. Sterken,
in het openbaar te verdedigen op
vrijdag 25 oktober 2013
om 11.00 uur

door

Sergey Punzhin

geboren op 27 april 1987
te Novgorod, Rusland

Promotor:	Prof. dr. J.Th.M. De Hosson
Beoordelingscommissie:	Prof. dr. P.R. Onck
	Prof. dr. H.A. De Raedt
	Prof. dr. P. Rudolf

Performance of Ordered and Disordered Nanoporous Metals

Sergey Punzhin

PhD thesis

University of Groningen

Zernike Institute PhD thesis series 2013-22

ISSN: 1570-1530

ISBN: 978-90-367-6404-9 (Printed version)

ISBN: 978-90-367-6413-1 (Electronic version)

The research presented in this thesis was performed in the Materials Science group of the Zernike Institute for Advanced Materials at the University of Groningen, The Netherlands. This work was funded by the Zernike Insitute for Advanced Materials.

Cover design by Selma Detsi.

university of groningen / faculty of mathematics and natural sciences / zernike institute for advanced materials

CONTENTS

Chapter 1

INTRODUCTION

1.1 Nanostructured materials

Starting from the second half of the 20th century the world has seen a great amount of attention on the development of progressively miniaturized systems in mechanical and electronic devices. In electronics this development comes as part of the well-known Moore's Law, where computational power is expected to double, on average, every fifteen months. Whilst this particular rate has been observed to decrease, the principle is expected to hold for the foreseeable future [1]. It then becomes a matter of course that, to maintain parity, devices used in processors - transistors, resistors, capacitors, etc. - must continually be miniaturized for more of them to be able to fit in the same operating space compared to their predecessors.

With this emphasis on miniaturization stemming from the electronics industry, the same push has been seen in mechanical systems. In medicine and biology, for example, there is a need for high-precision actuators and manipulators for work on fluid filtration and living cell manipulation [2]. The increasingly-popular lab-on-a-chip technology takes advantage of highly-miniaturized mechanical systems – Micro-Electronic Mechanical Systems or MEMS – to fit efficient analysis systems in a very small space. For progress in these fields there is a necessity for the continuous development of both materials with micro- and nanoscale functions and of tools that can facilitate the production and characterization of these materials.

As a rule, nanomaterials are defined as a material where one the dimensions of its defining feature is lower than 100 nanometres. This dimension is then considered negligible on the macroscale, and is the material's defining property. In this way, a two-dimensional (2D) material has a single dimension that is no larger than 100 nanometres, and such materials are commonly called thin films. Arrays of thin films are commonly seen in the electric and electronic industry as transistors or components in solar cells. Thin films are also used in catalysis and protective coatings for enhanced corrosion resistance [3,4].

Appropriately, a one-dimensional material has two dimensions under 100 nanometres. Common examples are nanowires and nanorods, the most prolific example of which is the carbon nanotube. Arrays of nanowires can form anisotropic films, where properties of the material vary depending on relative direction of influence. We see such behaviour in carbon fiber weave for structural uses [5].

At the lowest end of the scale are zero-dimensional materials, often called nanodots. Of great interest to the electronics industry, they have unique photonic and spin properties for use in the expected next generation of electronic devices: molecular transistors, quantum bits etc. [6]

By appropriately expanding the dimensions of a nanostructured material it is possible to make a material with very specific ordering tailored to suit the needs of a particular function. As mentioned above, stacked thin films form a three-dimensional structure with one-dimensional ordering. This principle can be applied to a zero-dimensional material: by stacking the zero-dimensional unit cell into three dimensions a three-dimensionally-ordered material can be made.

1.2 Actuation

Mechanical displacement that comes as a result of an electric signal passing through a material is called actuation. In materials that produce

an actuation response, the reverse is often possible as well – an electric current can be induced to flow if the material is deformed. The most common type of material that shows such properties is described as piezoelectric, and of this class of materials quartz is the most well-known. Indeed, it is the piezoelectric property of quartz that allows it to be used as an oscillating pace mechanism in the common wristwatch [7]. The typical piezoactuator delivers a ~0.2% strain at a high potential of 150V [8]. Considering that it is desirable to see the use of actuation in low-voltage devices, such as MEMS, much lower operational parameters are required for the modern actuating material [8].

Polymer-based actuation materials have been developed that offer extraordinary capacity for induced deformation, but have the drawback of being weak and compliant [8]. Extensive work by Gleiter, Kramer Weissmuller and Detsi [26] has demonstrated the potential of nanostructured metals to act as actuators, creating so-called “metallic muscles,” with the ability to demonstrate the properties required of the modern actuator: low throughput voltage requirements, high extension yield, strength and stiffness [9-11].

1.3 Metal foams and nanofoams

The principle of metallic composites has existed since the discovery that alloying metals yields a material with the properties of both of its parts. Indeed, a well-known alloy of copper and tin was the centrepoint of human civilization during the aptly-named Bronze Age, where tools, coin and weapons were all forged from the highly versatile metal [12]. Modern metallurgy is almost entirely focused on the development of multi-component alloys with properties tailored to fulfill specific functions [13, 14]. Taken from a wider point of view, a metal alloy is a type of composite material, where a composite material is, in general, described as a material composed of two or more different components.

When one of the components in a composite system is air, the system is described as being porous. Porous systems come in two types –

interconnected and non-interconnected (alternatively, open-cell and closed-cell, respectively), describing the relationship of the material's pores: in the former, there exists a continuous pathway between every single pore in the material and in the latter the pores exist independently as separated islands. A porous system is typically characterized by a high surface area-to-volume ratio due to the high amount of air-to-solid interface area as well as by a lower density and, by connection, by a lower weight compared to its solid bulk counterpart.

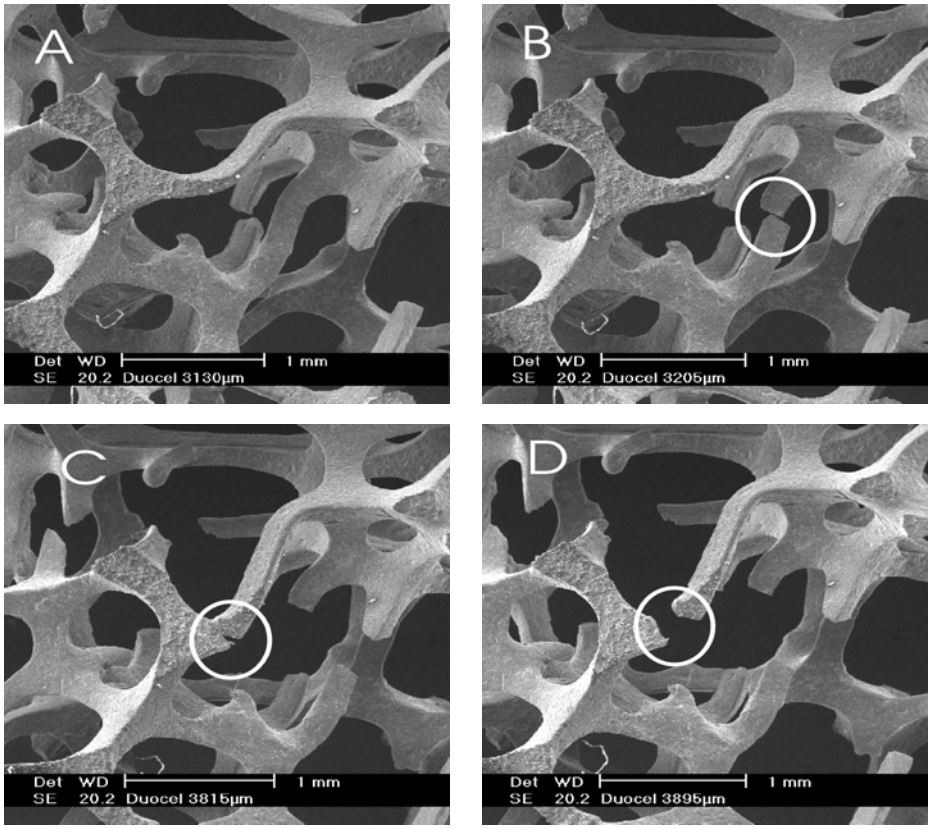

Figure 1.1: In-situ deformation in a Philips XL30-FEG-ESEM of Duocel 40 PPI macro foam with a relative density of approximately 7%. [52].

To briefly mention terminology, a porous material is made up of pores, struts and nodes. Pores are the encompassing term for the volume of air within a foam and struts are solid material that merge at nodes and connect nodes together.

The popularity of macrofoams i.e. porous materials where pore size is above the scale of tens of microns, stems from the intersection of a variety of desirable properties in industry. For example, aluminium macrofoam boasts a high stiffness-to-density ratio, high capacity for energy absorption during compression, high temperature resistance, electrical and thermal conductivity, good machinability and cheap production costs [15]. Such properties make macrofoams attractive in the construction and automotive industries, for example.

While macrofoams are common materials with known applications in industry, the class of materials known as nanofoams is more exotic. Operating under the same concepts as macrofoams in principle, nanofoams are characterized by pore and strut sizes being at the nanoscale, in other words the greatest diameter of a pore or strut must be considered a nanoscale dimension. For a more precise definition, the International Union of Pure and Applied Chemistry has categorized nanoporous metals into three groups, depending on the pore size: microporous metals have pore size under 2nm, mesoporous metals have pore sizes between 2 and 50nm and macroporous metals have pore size above 50nm.

Nanofoams share many properties with their macrofoam counterparts, such as the high surface-area-to-volume ratio, but also including the capacity for cheap production and easy machinability. In addition, however, nanoporous foams have seen usage in many applications beyond those of macrofoams, including nanofiltration systems, drug delivery platforms, catalysis, sensing and actuation [16-21]. A major advantage that nanoporous metals have is the ability to hold a lattice of nanoscale features whilst being able to be easily handled and

transported, something metallic nanoparticles, for example, cannot provide.

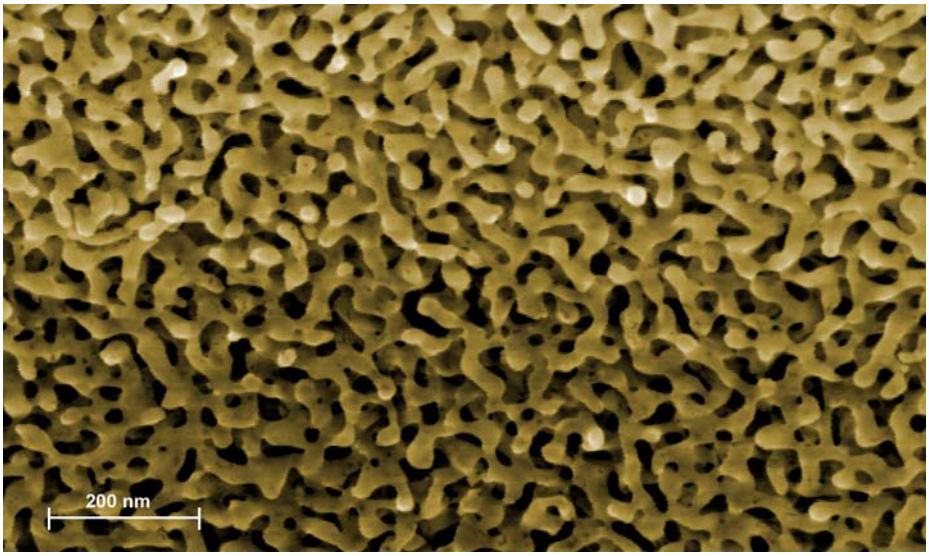

Figure 1.2: Typical nanoporous Au [26].

Production of disordered metal nanofoams.

In the majority of cases, metal nanofoams are produced through dealloying. For this process to work, an alloy must be produced between the required metal and another that can be etched away in some manner. It is also required that the two metals be able to form a solid solution, as any other morphology will not allow for the eventual formation of an isotropic structure of pores and ligaments. This is often the limiting factor for the dealloying process of nanofoam manufacture, as many metals do not easily form solid solutions, and if they do, it may not be possible to selectively etch one of the components of the alloy system whilst leaving the other intact.

Silver is alloyed with gold to form so-called “white gold,” an alloy commonly used in jewelry. The versatility of the alloy stems from its ability to form a solid solution at any ratio of gold to silver allowing for fine control of porosity of a resultant pure gold system.

While copper does not have alloy systems as simple as gold's with silver, copper-manganese forms a reliable solid solution across a wide range of compositions. Unfortunately, except for at very low percentages, Mn tends to segregate out of the solid solution and form a phase of pure Mn at low temperatures. This issue is solved through rapid quenching from solid solution temperature. This process prevents the formation of the pure Mn phase and, provided that the quenching had occurred successfully, yields an ingot with a microstructure comparable to that of Ag-Au alloy.

Mechanical properties of nanostructured materials at the nanoscale

While the production of nanoporous metallic structures is well-documented, up until recently very little was known about their mechanical properties - at submicron scales, sample size has the possibility to produce a large effect on mechanical properties, where in macroporous foams cell size specifically does not have an influence on material strength [22]. Indeed, it is highly uncertain that the behaviors of macroscopic and microscopic foams will be at all similar in principle and nature. Li and Sieradzki report that porous Au undergoes a ductile-brittle transition that seemed to be influenced by the microstructural length scale of the material [23]. Biener *et al.* have continued this investigation into the mechanical properties of nanoporous Au through nanoindentation [24]. They report the main deformation mechanism during nanoindentation as a ductile, plastic densification. Strong long-range stress fields, brittle fracture and crack emission were not observed. They note that the scaling laws that are typically applied to macroporous foams apply poorly to nanoporous metals, as they observe an experimental yield strength of 145MPa instead of the expected 16MPa.

Volkert *et al.* performed microcompression experiments on FIB-milled micron-sized pillars of nanoporous Au with 15nm diameter ligaments [25]. They find that, while Young's modulus values as determined experimentally and as predicted by scaling laws do not show significant

difference, there is a major increase in yield strength as sample size decreases below 50um length scales. A yield strength of 1.5GPa is predicted, which is several orders of magnitude above that of typical bulk Au. They interpret this effect as influenced by the increased required stress to activate dislocation sources as ligament size decreases, until theoretical shear strength is reached.

Further work by Biener *et al.* investigated this elevated yield strength and whether its origin was the microstructure of disordered nanoporous Au ligaments or the specific size-dependent mechanical properties of Au [22]. This was performed by preparing multiple samples with varying ligament sizes. It is established that in the production of a nanoporous material it is possible to tune ligament and pore size through varying dealloying conditions [26]. They observed a clear influence of ligament size such that the strength of nanoporous Au increases with decreasing ligament diameter, and thus propose that the Gibson and Ashby scaling model of foam plasticity [53] needs to be adjusted to take into account ligament size for nanoporous systems.

1.4 Ordered metal foams and nanofoams

As is often the case for many novel materials, interest in producing a nanoporous structure with an ordered, anisotropic pore structure came from observing nature. Specifically, the opalescence effect – variation in color based on direction of observation – seen in butterfly wings and mother-of-pearl stems from the ordered chitinous scales for the former or calcium plates for the latter serving as photonic diffraction gratings.

The brilliant colour variation seen in figure 1.3 is a light effect described as opalescence and is a result of an ordered nanoporous lattice acting as a series of waveguides, only permitting through light of a particular frequency depending on viewing direction. The use of waveguide materials such as this has been proposed for use in optical circuitry [27].

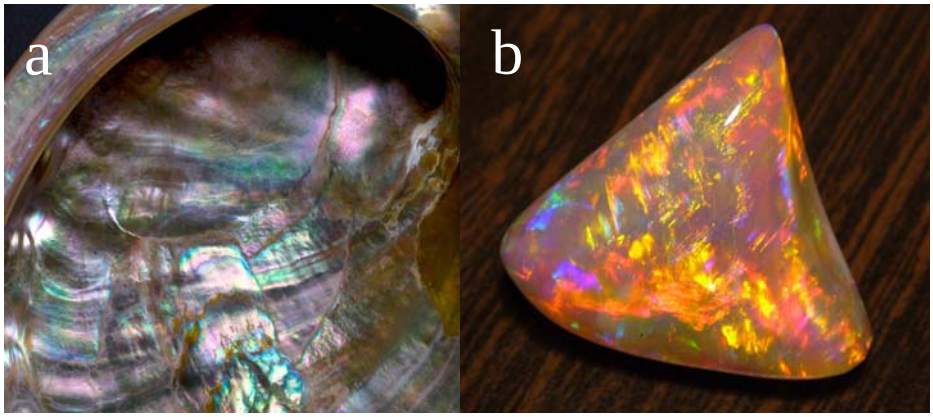

Figure 1.3: Mother-of-pearl, photo by Roy Kaltschmidt, Berkeley Lab (a) and natural opal, Department for Manufacturing, Innovation, Trade, Resources and Energy, Government of South Australia (b).

With clear applications across many industries, [28-30], three-dimensionally-ordered materials have garnered much attention. As with all nanostructured materials, two methods of approach are viable for their production: top-down and bottom-up. Top-down production focuses on reducing a bulk source sample down to the correct size, shape and morphology through a variety of destructive production methods. Whilst the top-down method boasts a very logical application with easy potential for iterative improvement, its greatest limitation is the scale down to which its production methods can reach – detail at the nanometer scale is beyond the capabilities of the typical top-down method [31-33]. The alternative is the bottom-up approach, where nanoscale features are assembled piece by piece into a full structure. This method allows for far finer detail control and overall quality of the assembled structure, but is typically challenging to implement due to it often being a multi-stage process.

Pre-templating production methods

The top-down process of production of nanostructured materials typically involves a starting bulk macroscale solid and then the use of

one of several techniques to achieve a nanostructure through size reduction. In medical applications, a top-down method for the production of nanoparticle suspensions is high-pressure homogenization, consisting of the repeated forcing of a suspension through a very thin gap at high velocity or media milling, which is the mechanical attrition of suspended particles using glass or zirconium oxide [34]. Mechanical attrition in general is a common procedure for the production of nanostructured materials, and one example of such a procedure is the method of ball milling, where powders are sealed in a strengthened container with a set of hard metal spheres and treated in a vibratory mill to elicit potential phase changes and the formation of nanostructured grains in the processed particles [35]. More non-standard procedures are also known: Yan *et al*. have proposed that, considering its simplicity and capacity for high-resolution spatial imaging, an atomic force microscopy (AFM) apparatus can be used to machine nanoscale features, and have demonstrated this capability in aluminium [36].

Nanosphere templating

As a whole, lithography is considered a top-down method, and is common in the electronics industry for the production of microchips. However, it can be converted into a bottom-up method by reducing the size of the initial template. This idea can be applied for 3D nanostructures: a porous 3D template is constructed that allows for the introduction of a particular material into the pore spaces within the template. After the template is removed the result is a 3D “image” of the template’s pore network. This is called inverse templating, and is the principal bottom-up method that allows for repeatable batch production in moderately large quantities, provided that the template is easily constructed. For this purpose, self-assembling templates are highly valued – templates whose component parts can, over time, arrange themselves into a desired 3D pattern with no further intervention aside from the initial process setup.

Nanosphere templating uses the natural ability of silica or polymer (PMMA, polystyrene, latex) nanospheres to reliably self-assemble into a template on a large scale. The nanospheres are suspended in a solution and are allowed to naturally settle over time, although centrifugation can be used to accelerate the process at the expense of quality of ordering. An alternative method is to allow the spheres to settle across a meniscus to improve ordering with the downside of the resultant template film being very thin. The spheres will preferentially settle into their most low-energy configuration, which is a crystalline face-centred cubic (FCC) arrangement. As the nanospheres settle, the solution evaporates and eventually a dry nanosphere template remains.

A settled nanosphere template is typically a weak, brittle solid, as the spheres are held together only through van der Waals forces. Thermal processing can be applied to strengthen a finished template by furnace-treating the template to allow necks to form between adjacent spheres. The appropriate temperature and time vary significantly by material, where several minutes at 120°C is enough for polymers like polystyrene, and several hours' processing at over 900°C is required for silica. The result is a much more robust template that can withstand mechanical rigor, but may be more challenging to remove.

Diblock copolymer templating

In principle, any sort of material with submicron-scale features that exhibits ordering can be used as a template, provided that interconnected voids exist between the features. One such material is the so-called "block copolymer." In such a material, two covalently-linked polymers, or blocks, undergo a process called microphase separation, i.e. attempt to separate as oil and water would, but are limited in their capacity to do so due to cross-linking. An enthalpy-entropy balance governs the specific manner in which this separation occurs. By controlling the compositions of the component block, it is possible to influence the phase behaviour of the copolymer and thus form a variety of phases: lamellar, cylindrical and spherical phases are

common, classical phases, with the perforated lamellar, gyroidal and ordered bicontinuous double diamond phases seen more rarely. In all cases, depending on the composition, one block forms the specific feature that the morphology is named after and the other forms a matrix around the feature.

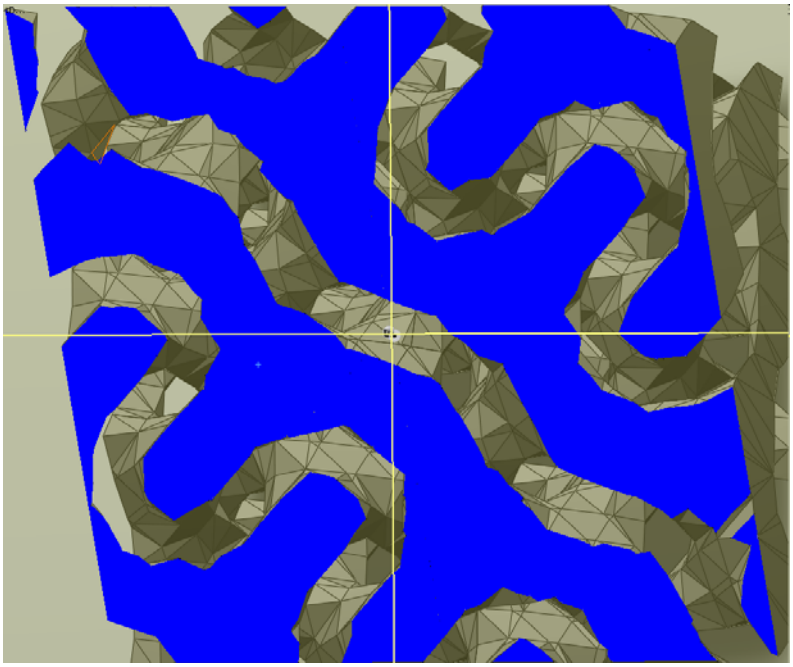

Figure 1.4: Cross-section of a diblock copolymer modeled using SolidWorks 2010. Characteristic double-wave pattern of the gyroid morphology is clearly visible.

Remarkably, all resultant structures show a high degree of ordering of their characteristic unit cell. As such, if, once a particular phase has been formed, one of the blocks of the copolymer could be removed whilst leaving the other preserved, the resultant polymer matrix could be used as an organic template. Of the possible phases formed by diblock copolymers, the gyroid phase is most interesting due to its repeating, long-ranged ordering of a three-dimensional feature. In other words, the gyroid morphology offers the strongest potential for use as a template to produce a three-dimensionally-ordered nanofoam.

Introducing material into a template.

The chief function of a template, obvious as it may seem, is to force material to grow around the template. In other words, material production methods compatible with templating are those that allow for the potentially complex morphology of the template whilst still forming a coherent solid. In this matter, most line-of-sight material deposition or coating methods like sputtering, PVD, plasma-assisted deposition etc. are incompatible with template-based production due to the natural obstruction that the template itself provides. This leaves liquid- and vapor-based deposition techniques as the best options.

Chemical vapor deposition (CVD) offers a commercially- and industrially-popular technique with the capacity for high-precision coating of surfaces with complex topography. A wide variety of metallic coatings can be applied using CVD: W, Al, Cu, Ag, Au and many others. Simply described, the CVD process involves the delivery of a precursor gas into a reactor, where it adsorbs onto a selected substrate and reacts to release supporting ligands from their metallic atoms. These atoms agglomerate to form particles and, eventually, a metallic coating layer. While CVD offers high purity and consistency in its coating process, its "low-temperature" conditions are described as being under 500°C, which can be a severely limiting experimental condition when the use of polymer templates is involved, which begin to denature at temperatures around 100°C [37].

Wet deposition techniques rely on the use of a solution to deliver the required material inside a template. Of these, the most common are electro- and electroless plating. Both suspend metal ions in a specific solution and employ a particular driving force to enable the ions to nucleate onto a surface.

Electrochemical plating, or electroplating, has been used since the 19th century to apply metallic coatings to materials. In electroplating a

substrate is submerged in an ionic solution and, in a typical system, is part of a three-electrode cell where the substrate acts as the working electrode, a noble metal acts as a counter electrode and a reference electrode, typically Ag-AgCl or Calomel, is used for stable control of the system. When the system is active, the ions in solution deposit on the working electrode and, typically, the non-metal component deposits or evolves at the counter electrode [38]. When used with a template, several additional factors come into play to complicate the process. The primary concern is the stability of the template in solution and its ability to adhere to the conducting substrate that acts as the working electrode. Provided this can be accounted for, another issue rises of the ability for metal ions to fully saturate the template. If the template is particularly complex, it is entirely possible for ions near the working electrode to deposit around the template, depleting the solution volume immediately around the electrode, with the rest of the rich solution requiring an extremely long time to fully diffuse into the template to continue the plating process. Finally, the metal is fixed to the substrate that it deposits onto, limiting the experimental capability of the material.

However, whilst the limitations of the process are very clear and non-negligible, the chief advantage of electroplating is the high degree of control that is possible over the deposition rate through electrochemical conditions applied, as well as the amount of experimental feedback received during deposition, as modern electrochemical experiments are carried out using highly sensitive sensing and processing apparatus.

Electroless plating, as its name implies, does not require an electric current for its deposition process and, therefore, is capable of plating non-conductive surfaces, allowing for a more homogeneous deposition into a template [39-42]. As a rule, the process requires a sensitization step and an activation step prior to the deposition of metal. The former adsorbs Sn ions onto the surface and the latter, through a redox reaction, forms Pd sites that subsequently act as a catalyst for the deposition process of the desired metal. Additional agents will be present in the

working solutions for buffering purposes and to stabilize the plating solution.

Removing templates.

Each template type commonly used in industry and academia also has a method to remove the template associated with it. It is a matter of course that the material used in the deposition step must be able to withstand the template etching process, and this requirement provides the most issues when coupled with the high complexity of typical 3D templates.

Silica templates are highly resistant to both etching and non-chemical treatments, and are mainly only susceptible to HF treatment. This greatly limits the amount of metals that can be grown in a silica template that can also be acquired as an ionic solution to, for the most part, only gold. In the case of organic templates more options are available for the removal of the template: pyrolysis, UV degradation, chemical etching etc.

Pyrolysis involves forcing the decomposition of an organic template at elevated temperatures, and has been observed to be very effective due to the method's high penetration capability into a template regardless of template complexity. The chief concern during pyrolysis is the effect of the treatment on the metal lattice that has been formed. Gold has been observed to coarsen heavily and quickly even at low temperature furnace treatments such that any ordering might be lost as ligaments deform. Less noble metals may oxidize if the pyrolysis is not carried out inside a controlled atmosphere, and others may undergo microstructural changes [43-44]

UV degradation is a common technique used during lithography-based manufacture of electronic circuitry that is inapplicable for use for 3D templates due to its being a line-of-sight technique that would only be able to degrade the upper layers of a polymer template before the rest of the template would be masked by the remaining metallic lattice.

Chemical etching is a wet process that does not face the issues of line-of-sight techniques and allows for selective chemical use that would not harm the metal within the template. However, this technique suffers the same problem as HF treatment for silica lattices: at a certain point the solvent's surface tension would prevent any deeper penetration and, thus, leave a large portion of the template intact.

1.5 Focused Ion Beam

The effects of high-energy particles striking a material are a major concern in the nuclear materials industry, where reactor housings and the components used within have to be designed with consideration of the influence of alpha, beta, gamma and neutron radiation. Such effects can be extremely detrimental to the operation of a reactor. Amongst them are, for example, the formation of voids within reactor walls, the embrittlement of affected surfaces, the formation of secondary phases or the formation of entirely new materials due to nuclear effects which can lead to the reduction of functionality of critical components like control rods [45].

High-energy particles have a beneficial use, however. The modern focused ion beam (FIB) instrument has a wide variety of applications in many fields [46], and is a versatile tool for sample preparation for scanning and transmission electron microscopy. The FIB operates through either deposition or sputtering of material to perform topological alterations to a sample. In both cases, ions of a particular species, usually Ga+, He+, Ne+ or Ar+ are excited to a high energy, typically 30keV, and accelerated towards their target. An incident ion imparts a large amount of energy to the target surface and this results in a series of effects: sputtering of material i.e. the release of the sample's surface atoms, ion implantation and formation of defects along the ion's trajectory within the material until it reaches a stopping point.

The sputtering effect is the most common and traditional use for the FIB, where material can be precisely and quickly removed. However, a high-energy particle emitted from a FIB entering a material will also transfer its energy to adjacent particles through inelastic collisions. These particles will do the same to their own neighbors in a process of so-called “knock-on” effects. Whilst some particles displaced in this manner will recover to their initial locations in the atomic lattice, others will remain displaced as interstitial atoms, leaving behind a vacancy in a defect type called a vacancy-interstitial or Frenkel pair. In this manner, a single high-energy particle traveling through a material will create a large amount of defects, and continuous exposure to a beam of high-energy particles will create a defect-rich layer in a material that is approximately as deep as the maximum penetration depth of the accelerated ions.

1.6 Ion-Beam-Induced Bending

In addition to the FIB’s already impressive list of qualities, another potentially useful behaviour has been observed in recent research. *In-situ* deformation of materials has been observed in FIB experiments: thermal-spike-induced deformation of colloidal solids in the work by van Dillen *et al.* [47] and deflection of free-standing amorphous silicon nitride thin films induced by a proposed biaxial compressive stress caused by the injection of an ion layer into the surface of the film [48].

While we have described the ions emitted by the FIB as high-energy, their energy profile compared to the particles used in high-energy nuclear experiments is extremely low, with acceleration energies rarely exceeding 50kV. The observations regarding deformation induced through focused ion beam exposure opened the possibility for micro-manipulation of extremely fine – easily at the submicron scale – features using nothing more than what is a moderately common laboratory apparatus.

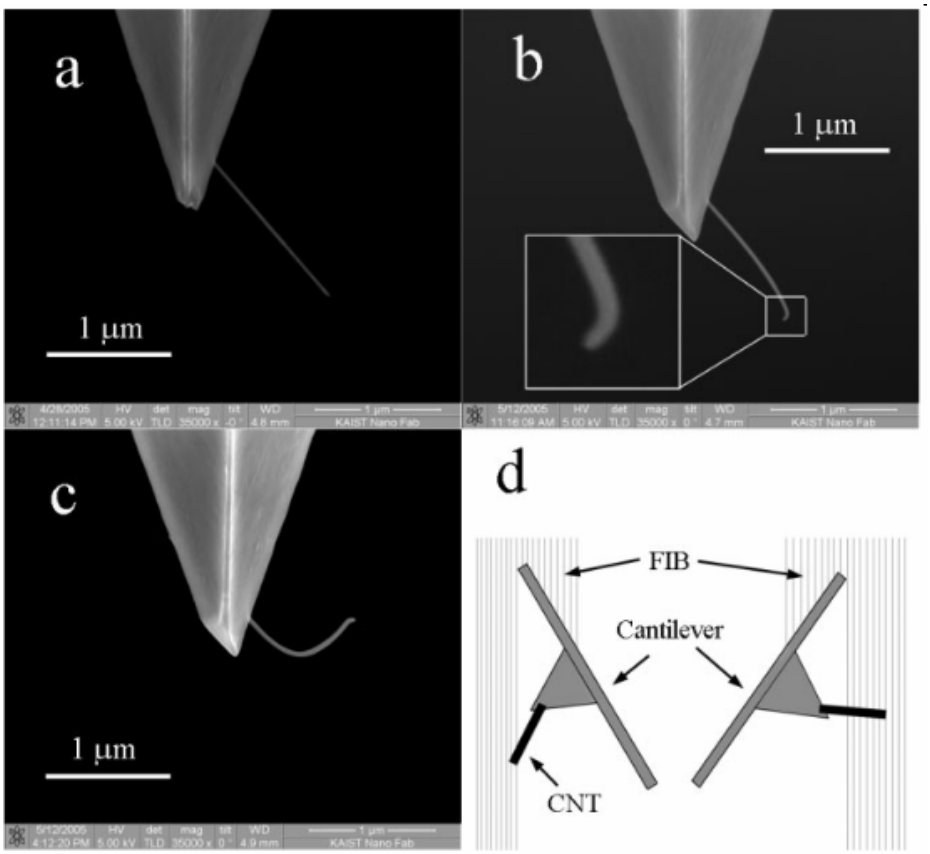

Figure 1.5: Demonstration of CNT bending by the FIB. a) The end of the as-attached CNT was illuminated by the FIB using a mask. b) The straight CNT was sharply bent at the end as a result, which can be seen magnified in the inset. The lower half of the CNT was in turn illuminated. c) The CNT was bent once more at a different point more in the middle. d) Schematics of how the cantilever acted as a mask for the process. The left configuration was used for the transformation from (a) to (b), and the right was used for (b) to (c). Reproduced from Bending of a Carbon Nanotube in Vacuum Using a Focused Ion Beam by Park *et al [49]*.

This deformation effect observed in a FIB has been coined Ion-Beam-Induced Bending (IIB) and has seen attention in recent years. As shown in Figure 1.5, Park *et al*. have used IIB to selectively deform and shape a scanning force microscopy (SFM) carbon nanotube tip to allow them

to perform experiments at unusual contact angles [49], and Tripathi *et al.* have further expanded on IIB in carbon nanotubes/cantilevers by presenting an explanation for the deformation effect based on thermal profiles induced in the nanotube/cantilever. In addition, they have shown the degree of control possible with this technique by bending a cantilever into a spiral shape through piecewise deformation. Rajput *et al.* performed similar experiments on crystalline metals, specifically silver [51], achieving similar results: controlled, reversible deformation with a high degree of finesse.

1.7 Use of IIB as a mechanical characterization tool.

If IIB can be demonstrated to be predictable through an accurate model then a path opens to the possibility of using IIB as a destructive method of characterization of the mechanical properties of extremely fine features that are beyond the capacity of typical physical contact-based techniques to measure.

In the scope of this thesis, we came up against an obstacle very much like this – when using picoindentation to examine the properties under compression of nanoporous metallic pillars, we observed that, as inaccuracies from various sources started to compound, it became progressively harder and harder to acquire results from which confident conclusions could be produced. We turned to investigating IIB as a characterization method that would give us the degree of precision and control we wanted.

For IIB to be used as a characterization technique several things are required: a consistent methodology with full control of the parameters involved, a comparative baseline between different materials such that consistency can be tested and confirmed, the knowledge of the underlying principles and an accompanying deformation model. The work in this thesis has touched on all of the above, with Chapters 4-7 offering the main focus on the principles of IIB.

1.8 Thesis overview.

The scientific content of this thesis is, as a whole, split into two parts. To elaborate, while the scope of the thesis initially covered the comparison of actuation properties of ordered and disordered nanoporous metals, it was learned that it would not be possible to develop a comparative baseline between the two materials, as it was not feasible to produce ordered nanoporous foam samples with the same dimensions and quality as their disordered counterparts.

In an attempt to sidestep this issue by applying a different method of characterization to the two types of materials – mechanical indentation – an interesting phenomenon was observed whose origins were not immediately obvious: the bending of a sample of particular dimensions under the influence of a focused ion beam, IIB. Further investigation into IIB, its principles and its mechanics followed, and, finally, IIB was applied in a callback to the original project scope to investigate the mechanical deformation properties of ordered and disordered metallic foams.

Thus, Chapter 3 contains the investigation and discussion of the initial proposal, and contains work on the production of ordered nanoporous templates, the use thereof for the production of ordered nanoporous metal foams and the characterization thereof through actuation and picoindentation. Chapters 4 onwards focus on investigations on the origins of ion-beam-induced bending, and perform an experimental series to establish IIB as a possible experimental tool.

Production of ordered nanoporous metal foams through inverse templating.

This part of the thesis contained in Chapter 3 concerns the work on the specific preparation of ordered nanoporous metal foams. Discussion starts from the preparation of templates themselves, with discussion of the merits and flaws of the two template types used: diblock

copolymers and nanospheres. The latter is additionally divided into the use of polystyrene, poly(methylmethacrylate) and silica nanospheres, each offering different characteristics and requirements of use for the nanosphere templating section. Discussion follows into the insertion of metallic species into a template by means of electro- and electroless plating. Results are presented of multiple combinations of use of nanosphere and diblock copolymer templates and the two plating techniques and we present conclusions on the efficacy of each different method based on the outcome of the experiments. Finally, we discuss the finished ordered metal foam that comes as a result of each of the combinations of template+plating method used with the appropriate accompanying template removal method.

Characterization of metallic foams.

The ordered nanoporous metal foams produced through the inverse templating method are subjected to investigation through actuation and picoindentation. The former is performed for the purpose of comparison between the actuation capabilities of ordered and disordered nanoporous metals. The latter is performed to supplement the currently-limited library of literature on the mechanical properties of nanofoams. In this section, also contained in Chapter 3, we discuss the performance of nanoporous nickel in a cyclic voltammetry setup, including the electrochemical characteristics of the metal as compared to gold, the best conditions for actuation given these electrochemical characteristics as well as the history of such experiments on gold, and actuation itself.

In addition, we discuss the implementation of picoindentation experiments to test the mechanical properties of pillars made of ordered and disordered nanoporous metals. Here, we talk about the issues inherent in the sample and setup arrangement, as well as some common behaviour observed during these experiments. The final sections of Chapter 3 talk about the transition of the investigation into focus on ion-beam-induced bending.

Chapter 1

Origin of IIB

A series of experiments are performed to investigate the limits of the effects of IIB in Chapter 4. Our initial experiments were on the easily-produced disordered nanoporous gold, and, through bending of these pillars *in-situ*, we test the reproducibility, accuracy and precision of IIB. We discuss bending behaviors of the nanoporous gold pillars, issues encountered and tendencies observed. Unsatisfied with the currently-presented in literature explanations of the mechanism behind the IIB effect, we develop a model to back up our own experimental findings. We produce this model through the consideration of the lattice stress produced due to vacancies produced by knock-on effects as ions travel through the material.

As a vacancy-rich layer builds up through continuous ion exposure, the lattice stress of each vacancy contributes linearly to an aggregate compressive stress across the vacancy-rich region. A bilayer effect is the result, where the vacancy-rich region experiences compressive stress and the vacancy-free region – where the ions have not penetrated – remains stress-neutral, with the overall effect being a bending deformation in the direction of the ion beam's source.

IIB: a comparative baseline

With the model in place, we perform IIB on a variety of solid crystalline materials: Al, Cu, Au. As the properties of these materials are well-known in literature, it should be possible to deduce quantitatively the effects of IIB on submicron features made from these metals and then apply this knowledge to their more complex nanoporous analogues. In Chapter 5 we present our findings during IIB of solid Au, Cu and Al pillars.

Here we first coin the terms homogeneous bending and point-bending as pillar responses to IIB, the former describing a continuous bend along the full length of the pillar, and the latter describing a localized

rapid bend with other sections of the pillar remaining straight. As point-bending is considered detrimental to IIB investigation due to its unpredictable, plastic effect, we search for its origin and attribute its occurrence to inhomogeneities within the pillar microstructure. Using samples undergoing homogeneous bending, we acquire a set of bending strains and Young's moduli. We use the Kinchin-Pease model to find the number of defects formed by the impact of a single ion and estimate the total number of defects present in a pillar at a given bending deformation.

By applying beam bending mechanics, we find the contribution of a single vacancy towards total bending stress in aluminium. We compare this value to that presented by atomistic simulation and find a large discrepancy, which we attribute to multiple factors, such as degree of amorphisation of the experimental sample and the main assumption that every single vacancy contributes to lattice stress without some of them compensating for each other. These considerations are combined into a black-box adjustment that allows compatibility between empirical and computational data that we use in future investigations.

IIB for the mechanical characterization of nanoporous metals

Using the experience from experiments in Chapters 4 and 5, we attempt to demonstrate the use of IIB as an experimental characterization tool in Chapter 6. We use disordered nanoporous Cu and Au for our experiments. We find that nanoporous pillars never exhibit point-bending, despite their solid counterparts doing so, and explain this behaviour as stemming from a homogenization effect that is caused by the porosity, where the pore-ligament microstructure becomes dominant over crystalline grain-based microstructure.

In addition, we observe the occasional tendency for a pillar's bending rate to accelerate during IIB. We find that the rate of acceleration increases linearly with decreasing pillar diameter and establish this as a rate-based mechanism: in pillars that bend quickly due to low stiffness,

diameter reduction does not occur quickly enough for bending acceleration to take place. In stiffer pillars, there is more time for this to occur.

Finally, we use the Kinchin-Pease model along with measured bending strains and the black-box adjustment calculated in Chapters 4 and 5 to calculate the Young's Modulus for nanoporous Au and Cu. We find that the value we find for nanoporous Au matches literature closely. With nanoporous Cu we find a discrepancy, which we attribute to the effects emerging from the prolonged exposure to the ion beam that is required for bending to occur in the stiffer material.

Order vs. disorder

In our continuing interest to establish IIB as an experimental characterization tool, we are interested in investigating the effects specific microstructural changes or features might have on a given material to give us an increasingly comprehensive view on the full capabilities of IIB. In addition, we are still interested in the difference in properties between ordered and disordered nanofoams.

To answer both interests, we use IIB to investigate the properties of ordered nanoporous nickel produced by inverse templating of gyroidal diblock copolymers. In Chapter 7 we use the same procedure as presented in chapters 4, 5 and 6 to investigate the IIB response of gyroidal nanoporous nickel and compare its properties to solid nickel. We find that the reduction in stiffness when going between solid and gyroidal nanoporous is much more severe than when observed between solid and disordered. This effect is attributed to the ordering: while induction of porosity creates a homogenization effect, the induction of ordering into the porosity reintroduces the possibility of localization effects and of preferential deformation planes akin to those of a crystalline solid.

1.9 References

[1] R R Schaller, *Spectrum, IEEE* , vol.34, no.6, pp.52,59, Jun 1997

[2] K Kudoh, T Gotoh, K Satoj, Y Yamagata, K Furutani, T Higuchi, Journal of Mammalian Ova Research 7, 7-12 (1990)

[3] M S Wilson, S Gottesfeld, *Journal of Applied Electrochemistry*, 22 (1990) 1-7

[4] T L Metroke, O Kachurina, E T Knobbe, *Progress in Organic Coatings,* Volume 44, Issue 3, June 2002, Pages 185-199

[5] B Lee, K H Leong, I Herszberg, *Journal of Reinforced Plastics and Composites* May 2001 20: 652-670

[6] S Link, M A El-Sayed, *The Journal of Physical Chemistry B* 1999 *103* (40), 8410-8426

[7] E Momosaki, S Kogure, *Ferroelectrics,*Vol. 40, Iss. 1, 1982

[8] H J Jin, X L Wang, S Parida, K Wang, M Seo, J Weissmuller, *Nano Letters* 10, 187-194 (2010)

[9] H Gleiter, J Weissmuller, O Wollersheim, R Wurshum, Acta mater. 49 (2001) 737-745

[10] J Weissmuller, R N Viswanath, D Kramer, P Zimmer, R Wurschum, H Gleiter, Science 300, 312 (2003)

[11] D Kramer, R N Viswanath, J Weissmuller, Nano Lett., Vol. 4, No. 5, 2004

[12] J D Muhly, American Journal of Archaeology, Vol. 89, No. 2 (Apr., 1985), pp. 275-291

[13] M Hever, *Modern Steel – High Performance Material For High Performance Bridges*, Conference Proceedings of 5th International Symposium On Steel Bridges, Barcelona 2003.

[14] W S Miller, L Zhuang, J Bottema, A J Wittebrood, P De Smet, A Haszler, A Vieregge, Materials Science and Engineering A280 (2000) 37 – 49

[15] E Amsterdam, *Structural Performance and Failure Analysis of Aluminium Foams*, (Groningen University Press, Groningen, 2008).

[16] A Wittstock, V Zielasek, J Biener, C M Friend, M Bäumer, *Science* 15 January 2010: 327 (5963), 319-322.

[17] L C Nagle, J F Rohan, International Journal of Hydrogen Energy, Volume 36, Issue 16, August 2011, Pages 10319-10326 .

[18] X Y Lang, H T Yuan, Y Iwasa, M W Chen, *Scripta Materialia*, Volume 64, Issue 9, May 2011, Pages 923-926,

[19] S D Gittard, B E Pierson, C M Ha, C-A M Wu, R J Narayan, D B Robinson, *Biotechnology Journal*, Volume 5, Issue 2, pages 192–200, February 2010

[20] M S Yavuz, Y Cheng, J Chen, C M Cobley, Q Zhang, M Rycenga, J Xie, C Kim, K H Song, A G Schwartz, L V Wang, Y Xia, *Nature Materials* 8, 935-939 (2009)

[21] L Au, D Zheng, F Zhou, Z-Y Li, X Li, Y Xia, *ACS Nano* 2008 *2* (8), 1645-1652

[22] J. Biener, A. M. Hodge, J. R. Hayes, C. A. Volkert, L. A. Zepeda-Ruiz, A. V. Hamza, F. F. Abraham, *Nano Letters* 2006 Vol. 6, No. 10 2379-2382

[23] R Li, K Sieradzki, Au. Phys. Rev. Lett. 68, 1168-1171 (1992)

[24] J Biener, A M Hodge, A V Hamza, L M Hsiung, J H Satcher, J. Appl. Phys. 97, 024301 (2005)

[25] C A Volkert, E T Lilleodden, D Kramer, J Weissmuller, Appl. Phys. Lett. 89 061920 (2006)

[26] E Detsi, Metallic Muscles: Enhanced Strain and Electrolyte-Free Actuation, Groningen University Press, Groningen, 2012

[27] J S Foresi, P R Villeneuve, J Ferrera, E R Thoen, G Steinmeyer, S Fan, J D Joannopoulos, L C Kimerling, H I Smith, E P Ippen, *Nature* 390, 143-145 (13 November 1997)

[28] X Li, F Tao, Y Jiang, Z Xu, *Journal of Colloid and Interface Science*, Volume 308, Issue 2, 15 April 2007, Pages 460-465

[29] K Soni, B S Rana, A K Sinha, A Bhaumik, M Nandi, M Kumar, G M Dhar, *Applied* Catalysis B: Environmental, Volume 90, Issues 1–2, 25 July 2009, Pages 55-63,

[30] Y Meng, D Gu, F Zhang, Y Shi, H Yang, Z Li, C Yu, B Tu, D Zhao, *Angewandte Chemie* Volume 117, Issue 43, pages 7215–7221, November 4, 2005

[31] H Yu, D Wang, M-Y Han, J. Am. Chem. Soc. 2007, *129*, 2333-2337

[32] P Garrigue, M-H Delville, C Labrugere, E Cloutet, P J Kulesza, J P Morand, A Kuhn, *Chem. Mater*. 2004, *16*, 2984-2986

[33] H-J Jeon, K H Kim, Y-K Baek, D W Kim, H-T Jung, *Nano Lett.* 2010, *10*, 3604-3610

[34] B Van Eerdenbrugh, G Van den Mooter, P Augustijns, *International Journal of Pharmaceutics* 364 (2008) 64-75

[35] C C Koch, *Rev. Adv. Mater. Sci.* 5 (2003) 91-99

[36] Y Yan, Z Hu, X Zhao, T Sun, S Dong, X Li, Small 2010, *6*, No. 6, 724-728

[37] M J Hampden-Smith, T T Kodas, *Chem. Vap. Deposition* 1995, *1*, No. 1

[38] M Schlesinger, M Paunovic, *Modern Electroplating, Fifth Edition*, Wiley 2011.

[39] W Riedel, *Electroless Nickel Plating*. Finishing Publications: Metals Park, 1991.

[40] G O Mallory, J B Hajdu, *Electroless Plating: Fundamentals and Applications*, American Electroplaters and Surface Finishers Society, 1992

[41] S S Djokic, *Electroless Deposition of Metals and Alloys*, vol. 35: Springer US, 2002, pp. 51-133

[42] S S Djokic, P L Cavallotti, *Electroless Deposition: Theory and Applications*, vol. 48: Springer New York, 2010, pp. 251-289

[43] H-Y Hsueh, R-M Ho, Langmuir 2012;28(22):8518-8529

[44] M Hakamada, M Mabuchi, *J. Mater. Res*, Vol. 24, No. 2, Feb 2009

[45] G H Vineyard, *Radiation Damage in Reactors*, AIP Conf. Proc. 19, pp. 182-201

[46] S Reyntjens, R Puers, *J. Micromech. Microeng.* 11 287 2001

[47] T van Dillen, A Polman, C M van Kats, A van Blaaderen, *Appl. Phys. Lett.* 83 4315 (2003)

[48] Y-R Kim, P Chen, M J Aziz, D Branton, J J Vlassak, *J. Appl. Phys.* 100, 104322 (2006)

[49] B C Park, K Y Jung, W Y Song, B-H O, S J Ahn, *Adv. Mater.* 2006, *18*, 96-98

[50] S K Tripathi, N Shukla, S Dhamodaran, V N Kulkarni, Nanotechnology, 2008 May 21;19(20):205302

[51] N S Rajput, A Banerjee, H C Verma, *Nanotechnology* 22 (2011) 485302

[52] K F L Michielsen, H De Raedt, J Th M De Hosson, 'Aspects of mathematical morphology', *Advances in Imaging and Electron Physics 125* 119-195 (2002).

[53] L J Gibson, M F Ashby, *Cellular Solids: Structure and Properties*, 2nd ed. (Cambridge University Press, Cambridge, 1997)

Chapter 2

CHARACTERIZATION TECHNIQUES

2.1 Microscopy

Scanning Electron Microscopy

Several scanning electron microscopes that are available in the Applied Physics-Materials Science group were used, including FEI-FEG XL-30, FEI-FEG XL-30s, FEI-FEG ESEM XL-30, for visual characterization of the microstructure of materials produced during research. All these scanning electron microscopes are equipped with an Electron Dispersive Spectroscopy (EDS) module. In the following we present a concise review for the non-experts, without going into all the details. The summary is based on the summaries that were also presented by former PhDs in our group, in particular by Bas Groen, Patricia Carvalho, Wouter Soer, and Zhenguo Chen. [1,2,3,4].

The Scanning Electron Microscope (SEM) is a type of electron microscope that study microstructural and morphological features of the sample surface by scanning it with a high-energy electron beam in a raster scanning pattern. The electrons interact with the sample matter producing a variety of signals that contain information about the sample surface topography, composition and other properties.

The first SEM image was obtained by Max Knoll, who in 1935 obtained an image of silicon steel showing electron channeling contrast [5]. The SEM was further developed by Professor Sir Charles Oatley and his postgraduate student Gary Stewart and was first marketed in 1965 by the Cambridge Instrument Company as the "Stereoscan".

The signals produced by an SEM include secondary and back-scattered electrons (SE & BSE), characteristic X-rays, cathodoluminescence (light), specimen current and transmitted electrons. The SE detector is the most common one in SEM. As shown by the schematic Figure 2.1, in an FEI/Philips XL-30 FEG-SEM (Field Emission Gun), electrons are generated by the field emission gun using a high electrostatic field.

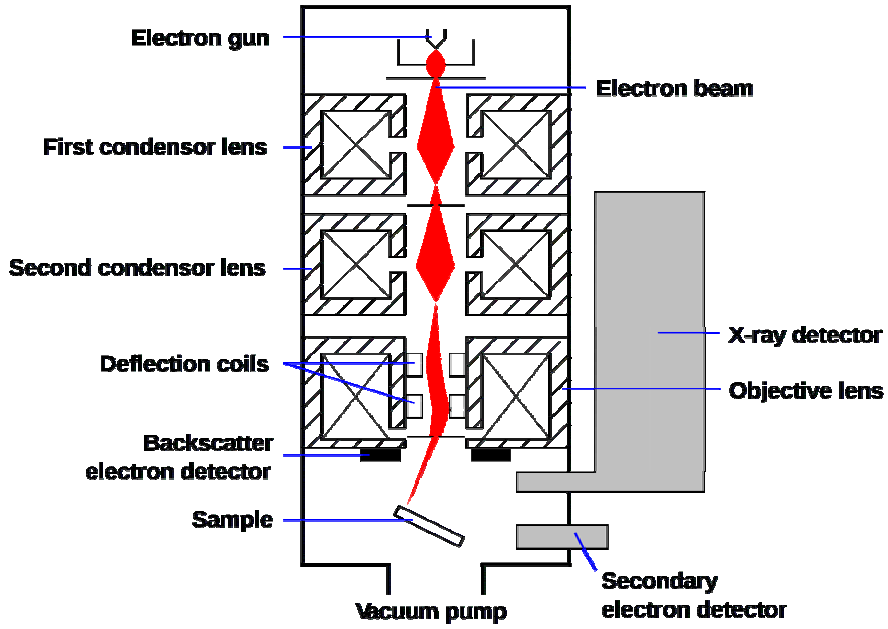

Figure 2.1: Schematic figure of the Scanning Electron Microscope.

The electrons are accelerated with energies between 1keV and 30keV down through the column towards the specimen. While the magnetic lenses (condenser and objective lenses) focus the electron beam to a spot with a diameter of approximately 10nm, the scanning coils sweep

the focused electron beam over the specimen surface. If the microscope is operated in the backscattered mode, the result is a lateral resolution on the order of micrometers. The number of back-scattered electrons produced is proportional to the atomic number of the element bombarded. The result is that material with a high(er) atomic number produces a brighter image. To capture this information a detector is required which can either be metal, which is the least effective, but is versatile and used in environmental scanning electron microscopy (ESEM); semi-conductor, which is most common, or a scintillator/light pipe/photomultiplier, which are the most efficient.

The primary electron current is approximately 10^{-8} to 10^{-7}A. The large penetration depth of the high energy electrons will cause the electrons to be trapped in the material. When studying conducting materials, the electrons will be transported away from the point of incidence. If the specimen is a non-conducting material, the excess electrons will cause charging of the surface. The electrostatic charge on the surface deflects the incoming electrons, giving rise to distortion of the image. To reduce surface charging effects, a conducting layer of metal, with typical thicknesses 5-10nm, can be sputtered onto the surface. This layer will transport the excess electrons, reducing the negative charging effects. An adverse effect of the sputtered layer is that it may diminish the resolving power of the microscope, since topographical information is no longer gained from the surface of the material, but from the sputtered layer. Charging of the surface is not the only factor determining the resolution of a scanning electron microscope. The width of the electron beam is also an important factor for the lateral resolution. A narrow electron beam results in a high resolution. The spot size however, is a function of the accelerating voltage

$$d_p^2 = \frac{1}{\alpha^2}\left[\frac{i}{B} + \lambda^2\right] + \left[\frac{\Delta E}{E_0} C_c\right]^2 \alpha^2 + \left[\frac{1}{2} C_s\right]^2 \alpha^6 \qquad (2.1)$$

The broadening of the spot size is the sum of broadening effects due to several processes. The first contributor is the beam itself, B is the brightness of the source, i is the beam current and α its divergence angle. The second part is the contribution due to diffraction of the electrons of wavelength λ by the size of the final aperture. The last two parts are the broadening caused by chromatic and spherical aberrations, where E_0 is the electron energy, ΔE is the energy spread, C_s is spherical aberration and C_c is the chromatic aberration coefficient. To achieve the smallest spot size, all contributions should be as small as possible. Decreasing the accelerating voltage will not only cause the wavelength of the electrons to increase, but also the chromatic aberration increases as well, resulting in increasing of the spot size and, as a consequence, a decrease in resolving power of the microscope.

A field emission gun has a very high brightness B, reducing the contribution in broadening due to the beam itself. The energy spread ΔE in the electron energies is also small. Together with the fact that the coefficients C_S and C_C can be reduced by optimising the lenses for low-energy electrons, provides the FEG low voltage scanning electron microscope with very high resolving power. In this thesis scanning electron microscopy is carried out with a FEI Philips XL30-FEG or XL30s-FEG SEM equipped with a field emission gun (FEG).

Transmission Electron Microscopy

In our work a high-resolution transmission electron microscope (Jeol4000EX./II) and an analytical transmission electron microscope Jeol2010FEG, operating at 400kV and 200kV respectively, were used for characterization at scales inaccessible for classical scanning electron microscopy.

The first TEM was built by Max Knoll and Ernst Ruska in 1931. The first TEM with a resolving power greater than that of light was successfully designed in 1933 and the first commercial TEM became

available in 1939. Transmission Electron Microscopy (TEM) has revolutionized our understanding of materials by completing the *processing-structure-properties* links down to atomistic levels [5].

In the TEM, as shown in Figure 2.2, the electron beam is transmitted through an ultra-thin specimen, interacting with the specimen as it passes through. An image is formed from the interaction of the electrons transmitted through the specimen; the image is magnified and focused onto an imaging device, such as a fluorescent screen or photographic film, or is detected by a sensor such as a CCD camera.

Conventional transmission electron microscopy is the most widely used technique to image defects in crystals. [6] The image contrast caused by dislocations is based on electron diffraction following Bragg's law. A useful description of electron diffraction in crystals is given by the concept of the Ewald sphere. The Ewald sphere is constructed in the reciprocal lattice by letting the incident wave vector $\mathbf{k}_i$ end on one of the reciprocal lattice points and drawing a sphere around its origin with a radius of $|\mathbf{k}_i| = 1 / \lambda_e$, where λ_e is the (relativistic) de Broglie wavelength of the electrons. The diffracted wave vector $\mathbf{k}_d$ has the same length as $\mathbf{k}_i$ and the magnitude of their difference $\mathbf{K} = \mathbf{k}_d - \mathbf{k}_i$ is related to the diffraction angle θ by

$$|\mathbf{K}| = \frac{2\sin\theta}{\lambda_e} \tag{2.2}$$

For those reciprocal lattice points that are intersected by the Ewald sphere, the diffraction vector has a length equal to the inverse interplanar spacing $1 / d_{hkl}$ and therefore the Bragg condition is satisfied, i.e.

$$\lambda_e = 2d_{hkl}\sin\theta \tag{2.3}$$

In electron diffraction of volumes that are constrained to a small length scale in one or more dimensions (a TEM foil is constrained in at least

one dimension: the thickness), diffraction also occurs for wave vectors that do not exactly fulfill the Bragg condition. The excitation error can accordingly be defined as $\mathbf{s_g} = \mathbf{K} - \mathbf{g}$.

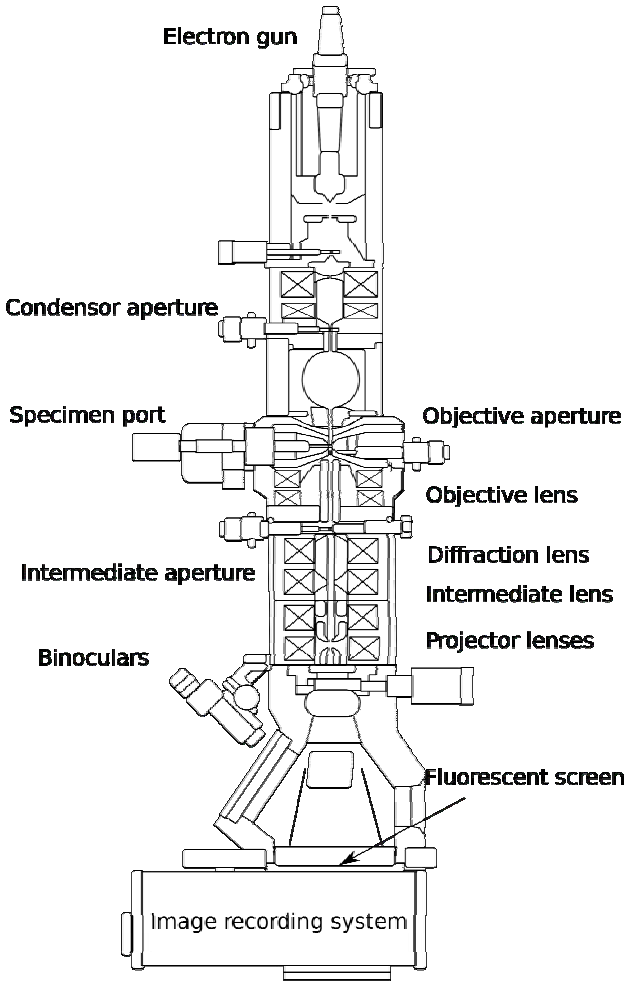

Figure 2.2: Schematic figure of the Transmission Electron Microscope.

To interpret electron micrographs it is essential to understand the factors that determine the intensities of Bragg-diffracted beams. Various approaches can be followed, i.e. ranging from the kinematical theory to the dynamical theory of electron diffraction. The former is based on the assumptions that only elastic scattering takes place (hence

no absorption) and that an electron can be scattered only once, whereas the latter also allows for interaction between the diffracted beams. This interaction is particularly well-defined when the crystal is tilted in such a way that, besides the direct beam, only one beam is strongly diffracted (i.e. $|\mathbf{s_g}| >> 0$ for the other reflections). As the transmitted wave with amplitude $\phi_0(z)$ propagates through the crystal, its amplitude is depleted by diffraction and the amplitude $\phi_\mathbf{g}(z)$ of the diffracted beam increases, i.e. a dynamical interaction between $\phi_0(z)$ and $\phi_\mathbf{g}(z)$ exists. If we assume that $\mathbf{s_g}$ is parallel to the electron beam, the interaction can be described by the following pair of coupled differential equations, known as the Howie-Whelan equations:

$$\frac{d\phi_\mathbf{g}}{dz} = \frac{\pi i}{\xi_0}\phi_\mathbf{g} + \frac{\pi i}{\xi_\mathbf{g}}\phi_0 e^{-2\pi i s_\mathbf{g} z} \tag{2.4}$$

and

$$\frac{d\phi_0}{dz} = \frac{\pi i}{\xi_0}\phi_0 + \frac{\pi i}{\xi_\mathbf{g}}\phi_g e^{2\pi i s_\mathbf{g} z} \tag{2.5}$$

where $s_\mathbf{g} = |\mathbf{s_g}|$ and ξ_0 and $\xi_\mathbf{g}$ are the extinction distances for the direct and diffracted waves, respectively. The extinction distance is a characteristic length scale determined by the atomic number of the material, the lattice parameters and the wavelength of the electrons, it typically lies between 10 and 100nm. The above equation shows that the change in $\phi_0(z)$ as a function of depth z is the sum of forward scattering and scattering from the diffracted beam, taking into account a phase change of $\pi/2$ caused by the scattering. Solving the previous 2 equations for $\phi_\mathbf{g}(z)$ gives:

$$\phi_g = \frac{i}{\sqrt{1+s_g^2\xi_g^2}}\sin\left(\frac{\pi t}{\xi_g}\sqrt{1+s_g^2\xi_g^2}\right) \tag{2.6}$$

where t is the thickness of the crystal. Accordingly, the intensity of the diffracted beam becomes:

$$I_{\mathbf{g}} = \left|\phi_{\mathbf{g}}\right|^2 = \frac{\sin^2 \pi t s_{\text{eff}}}{\xi_{\mathbf{g}}^{\ 2} s_{\text{eff}}^{\ 2}} \tag{2.7}$$

where s_{eff} is an effective value of $s_{\mathbf{g}}$ defined by $s_{\text{eff}} = (s_{\mathbf{g}}^{\ 2} + \xi_{\mathbf{g}}^{\ -2})^{1/2}$. In fact, by replacing s_{eff} by $s_{\mathbf{g}}$, the intensity according to the kinematical approximation is found. Absorption can be included in the dynamical theory by adding appropriate terms to both ξ_0 and $\xi_{\mathbf{g}}$. Mathematically speaking, absorption is included simply by allowing the arguments of the sines and cosines to become complex.

Dislocations or stacking faults give rise to contrast because they locally distort the lattice and thereby change the diffraction conditions. If the distortion is given by a displacement field **R**,i.e.

$$\frac{d\phi_{\mathbf{g}}}{dz} = \frac{\pi i}{\xi_0}\phi_{\mathbf{g}} + \frac{\pi i}{\xi_{\mathbf{g}}}\phi_0 \exp\left[-2\pi i\left(s_g z + \mathbf{g}\cdot\mathbf{R}\right)\right] \tag{2.8}$$

In order for a dislocation to contribute to contrast formation, the dot product $\mathbf{g}\cdot\mathbf{R}$ must be nonzero. A screw dislocation in an isotropic elastic medium has a displacement field parallel to its Burgers vector, and therefore produces no contrast when $\mathbf{g}\cdot\mathbf{b} = 0$. General dislocations have a displacement field with more components; their image contrast also depends on $\mathbf{g}\cdot\mathbf{b}_e$ and $\mathbf{g}\cdot(\mathbf{b}\times\mathbf{u})$, where $\mathbf{b}_e$ is the edge component of the Burgers vector and $\mathbf{u}$ is a unit vector along the dislocation line. In practice however, only very faint contrast occurs when $\mathbf{g}\cdot\mathbf{b} = 0$ but $\mathbf{g}\cdot\mathbf{b}_e \neq 0$ and $\mathbf{g}\cdot(\mathbf{b}\times\mathbf{u}) \neq 0$. Therefore, the "invisibility criterion" $\mathbf{g}\cdot\mathbf{b} = 0$ is used commonly to determine Burgers vectors of dislocations in elastically isotropic solids. The determination of a Burgers vector involves finding two reflections $\mathbf{g}_1$ and $\mathbf{g}_2$ for which the dislocation is invisible, so that $\mathbf{b}$ is parallel to $\mathbf{g}_1\times\mathbf{g}_2$.

The situation where only one beam $\phi_{\mathbf{g}}(z)$ is strongly diffracted is referred to as a two-beam condition. This type of diffraction is widely used in conventional TEM of crystalline materials because the contrast is well defined and the Burgers vectors of the dislocations can be determined as described above. By using the objective aperture in the microscope, either of the two beams can be selected to form an image and accordingly, two imaging modes may be distinguished: bright field (BF) when the direct beam $\phi_0(z)$ is used, and dark field (DF) when the diffracted beam $\phi_{\mathbf{g}}(z)$ is used. Generally, the diffracted beams do not coincide with the optical axis of the microscope and consequently the DF image will not be of maximum quality due to spherical aberration. To overcome this problem, the incident beam is normally tilted in such a way that the desired diffracted beam passes along the optical axis.

While two-beam conditions produce high contrast of dislocations, the resolution at which these defects are resolved is not optimal since the lattice planes around the dislocations are distorted over a relatively large area. To obtain the maximum resolution, the crystal should be tilted slightly further by such an amount that the exact Bragg condition is only fulfilled within a small region near the dislocation. In this way, a high-resolution image is obtained in which the dislocation shows up as a bright line. This technique is referred to as weak-beam imaging. The deviation from the exact Bragg condition for perfect crystal is given by $s_{\mathbf{g}}$ as mentioned above and can be determined accurately by the relative position of the so-called Kikuchi pattern with respect to the diffraction pattern. The origin of the Kikuchi pattern lies in the elastic re-scattering of inelastic scattered electrons as further explained in the following section.

The width of a dislocation image is approximately $0.3\xi_{\mathbf{g}}$, i.e. several tens of nanometers in conventional bright- and dark-field imaging. This width can be detrimental to the observations of dislocations that are very closely spaced. Since the effective extinction distance decreases for increasing deviation away from the Bragg condition, the width of a

dislocation image can be reduced to values in the order of 1 to 5nm in weak-beam imaging.

At lower magnifications, the average crystal orientation may vary considerably within the observed area, so that only a small area of the specimen can be set up in two-beam condition. This is especially relevant in specimens that have been deformed prior to preparation. In these cases, it is often convenient to orient the specimen close to a zone axis, so that many reflections are weakly excited, independently of small changes in orientation. By using the direct beam for imaging, the dislocation structure can be imaged with good contrast over a relatively large area. However, the contrast from individual dislocations is generally smaller than in two-beam condition and not well defined since it results from many different reflections.

Another TEM technique refers to high-resolution and is called HRTEM. The essence of HRTEM imaging lies in the transformation of the phase differences in the exit wave into amplitude modulation, and therefore contrast. In the Fraunhofer approximation to image formation, the intensity in the back focal plane of the objective lens is simply the Fourier transform of the wave function exiting the specimen. Inverse transformation in the back focal plane leads to the image in the image plane. However, if the phase-object approximation holds, the image of the specimen by a perfect lens shows no amplitude modulation. In practice, however, a combination with the extra phase shifts induced by defocus and lens aberrations generates suitable contrast. The influence of the extra phase shifts can be taken into account by multiplying the wave function at the back focal plane with functions describing each specific effect. As such effects can be conceived cylindrical symmetric, they can be represented as a function of the distance of the reciprocal lattice point from the optic axis, $U = (u^2 + v^2)^{1/2}$, where u and v are the angular variables used for the distribution of amplitude or intensity in reciprocal space.

The phase factor used to describe the shifts introduced by defocus and spherical aberration is [7,8]:

$$\chi(U) = \pi\lambda\Delta f U^2 + \tfrac{1}{2}\pi C_s \lambda^3 U^4 \tag{2.9}$$

with Δf the defocus value of the objective lens and C_s the spherical aberration. The function that multiplies the exit wave is then:

$$\mathrm{B}(U) = \exp(i\chi(U)) \tag{2.10}$$

If the specimen behaves as a weak-phase object, only the imaginary part of B(U) contributes to the contrast in the image, T(U):

$$\mathrm{T}(U) = \sin(\chi(U)) = \sin(\pi\lambda\Delta f U^2 + \tfrac{1}{2}\pi C_s \lambda^3 U^4) \tag{2.11}$$

which is known as the contrast transfer function (CTF) of the objective lens, so called because it determines the weight of each scattered beam transferred to the image intensity spectrum. In this way, the phase information from the specimen is converted into intensity information by the phase shift of the objective lens. The aperture inserted at the back focal plane of the objective lens only allows transmitted beams up to a certain angle. Its effect can then be represented by multiplication with an aperture function A(U) which is unity for $U < U_0$ and zero outside this radius. In practice, combinations of fluctuations in high voltage and lens current, objective lens chromatic aberration, mechanical vibrations along z and usage of a partly converged beam cause loss of spatial and temporal beam coherency, which have been assumed so far. Such effects result in a smearing of the image, and compromise the ultimate resolution, since for high frequencies, the transfer function is now damped and approaching zero. Partial temporal coherence can be represented as a spread of focus, E_Δ, and partial spatial coherence as incident beam convergence, E_α. These effects are taken into account by multiplying sin(χ) with specific damping envelopes. A definition of resolution is not easily given for an electron microscope. In the case of completely incoherent imaging, as in optical microscopy, it is possible to define point resolution as the ability to resolve individual point objects.

This resolution can be expressed (using the criterion of Rayleigh) as a quantity independent of the nature of the object. In electron microscopy, however, the illumination is more coherent and the resolving ability depends on the diffracting behaviour of the object. For example, for thick specimens, there is not necessarily a one-to-one correspondence between the projected structure of the object and its image.

Therefore, the concept of microscope resolution is only meaningful for thin objects, and furthermore, one has to distinguish between:

- *Point resolution*, which is related to the finest detail that can be directly interpreted in terms of the specimen structure. Since the CTF depends very sensitively on defocus, and in general shows an oscillatory behaviour as a function of U, the contribution of the different scattered beams to the amplitude modulation varies. However, for particular underfocus settings the microscope approaches a perfect phase contrast microscope for a range of U before the first crossover, where the CTF remains at values close to –1. It can then be considered that, to a first approximation, all the beams before the first crossover contribute to the contrast with the same weight, and cause image details that are directly interpretable in terms of the projected potential. Optimisation of this behaviour through the balance of the effects of spherical aberration vs defocus leads to the generally accepted *optimum defocus* $-1.2(C_s\lambda)^{1/2}$. Designating an optimum resolution involves a certain degree of arbitrariness. However, the point where the CTF at optimum defocus reaches the value –0.7 for $U = 1.49C_s^{-1/4}\lambda^{-3/4}$ is usually taken to give the *optimum (point) resolution* ($0.66C_s^{-1/4}\lambda^{-3/4}$). This means that the considered passband extends over the spatial frequency region within which transfer is greater than 70%. Beams with U larger than the first crossover are still linearly imaged, but with reverse contrast. Images formed by beams transferred with opposite phases cannot be intuitively interpreted.

- *Information limit resolution*, corresponding to the highest spatial frequency still appreciably transmitted to the intensity spectrum. This resolution, which is higher than the point resolution, is related to the finest detail that can actually be seen in the image, which however is only interpretable using image simulation. For a thin specimen, such limit is determined by the cut-off of the transfer function due to spread of focus and beam convergence (usually at $1/e^2$). The use of FEG sources minimizes the loss of spatial coherence. This helps to increase the information limit resolution in the case of lower voltage (≤ 200 kV) instruments, because in these cases the temporal coherency does not usually play a critical role. On the other hand, with higher voltage instruments, due to the increased brightness of the source, the damping effects are always dominated by the spread of focus and FEG sources do not contribute to an increased information limit resolution.

The resolution performance can generally be improved by increasing the accelerating voltage of the microscope to reduce λ and/or decreasing the coefficient of spherical aberration of the objective lens. Unfortunately, the use of very high accelerating voltages is ultimately limited by the damage caused to the specimen and the reduction of C_s usually involves specific pole piece designs that pose restrictions to specimen tilt capabilities.

Due to the finite resolution, a correct interpretation of the structure requires a careful alignment of the specimen along a low-index zone axis. In practice however, a residual crystal tilt, of a fraction of 1mrad, usually remains. Beam tilt has a more detrimental influence on the image because the beam enters the objective lens at an angle, causing phase changes in the electron wave front. This effect can be corrected by the voltage-centre alignment, whereby the acceleration voltage is varied to find the centre of magnification that is then placed on-axis. However, this procedure does not account for misalignments in the imaging system after the objective lens. For an accurate correction, the coma-free alignment is necessary. The process involves alternatively applying equal

and opposite beam tilts to the incident beam, and subsequent comparison of the two resulting images (for two orthogonal directions). If there is residual beam tilt, one image is more distorted than the other and the beam-tilt controls should be adjusted until both tilted images display similar distortions. Nevertheless, in practice such procedure is only feasible with a computer-controlled microscope, equipped with a CCD camera, and has not yet been used in the current work; the voltage-centre alignment was used instead, inevitably resulting in some residual beam tilt. On the other hand, two-fold astigmatism can normally be easily removed by the operator, because of its clear effect on the image of amorphous edges. The microscope parameters can be kept constant from experiment to experiment by a careful mode of operation.

2.2 Focused Ion Beam

The typical function of an ion beam apparatus is either the removal or the addition of material - depending on the nature of ions and their acceleration energy - through bombarding a target with accelerated ions. Incoming ions typically have much more energy than the bond energy of the atoms of their target and, upon impact, break a large amount of atomic bonds as they move into the material. The release of atoms as they break free from the source material due to this imparted energy is called sputtering, and the use of this process to selectively change the shape of an object using the ion beam is called milling.

A dual beam FIB/scanning electron microscope (SEM) microscope (Lyra, Tescan, CZ) apparatus was used in all ion-beam related experiments. The apparatus produces a Ga ion beam with an acceleration voltage of 30keV. The ion beam's spot size and ion current can be varied. During all experiments, the spot size remained unchanged. The ion current operates on factory presets, with settings for 1, 10, 40, 150, 200, 1000 and 10000pA. True ion current is measured internally using a Faraday cup, and it is consistently observed that the true ion current varies from that of the setting at which that

current is produced. The variation can be up to a factor of two above or below the preset value. While this variation is small on the absolute scale at low ion current values, it quickly becomes significant as ion current increases.

The FIB apparatus is equipped with a computer-controlled moving stage that allows for 360 degree rotation as well as tilt that ranges from -20 to +70 degrees. Through a combination of rotation and tilt a sample can be observed from any angle. (for schematics see Figure 2.3)

There is a 55 degree angle between the electron and ion emitters, such that a sample being observed from a perpendicular inclination with the SEM will be 55 degrees tilted away from the normal when observed with the ion beam.

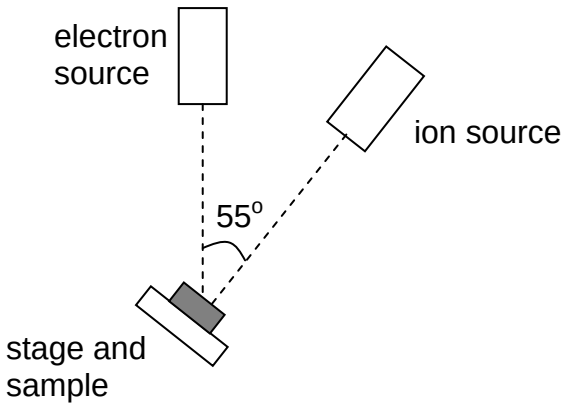

Figure 2.3: Schematic illustration of FIB/SEM dual beam arrangement.

As such, it is customary for a sample to be tilted 55 degrees once the working area has been found.

The FIB apparatus is capable of masking its ion beam during emission to allow for a variety of milling types – random and polish. During

random milling a selected area is continuously bombarded with ions with each ion striking a random point within the area. During polish milling the ion beam removes material a row of ion "pixels" at a time, which often ensures a far cleaner edge than random milling.

Pillar production

The formation of nanoscale pillars is performed entirely using the FIB apparatus. The single prior requirement of a source sample from which pillars will be milled is that an edge of no more than 10μm thickness is accessible. This requirement can be achieved by applying large-scale mechanical milling or through careful cutting.

A sample is mounted on a classical SEM aluminium stub such that it lies parallel to the stub's surface and the working edge protrudes approximately a millimeter away from the stub. This protrusion is necessary, as it provides a sufficiently large working space for the ion beam. The mounting can be done through any method provided that an electrical contact remains between the sample and the aluminium stub, although the most common is the use of silver paste as a conductive adhesive.

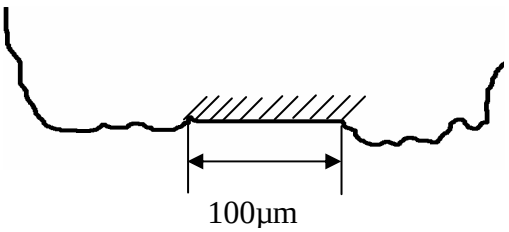

Figure 2.4: Illustration of working area preparation. Ion beam is incident into the page.

What follows is a multi-step procedure that uses progressively lower ion currents to achieve an increasingly fine quality of mill:

A working area is milled out of the source's sample's leading edge of approximately 100µm (Figure 2.4). The working area should be as flat as possible.

Rectangular "teeth" are cut out of the working area at the highest current setting. This is done with the ion beam perpendicularly aligned to the source sample. The spacing and dimensions of the teeth are approximately equal to the initial source sample's thickness.

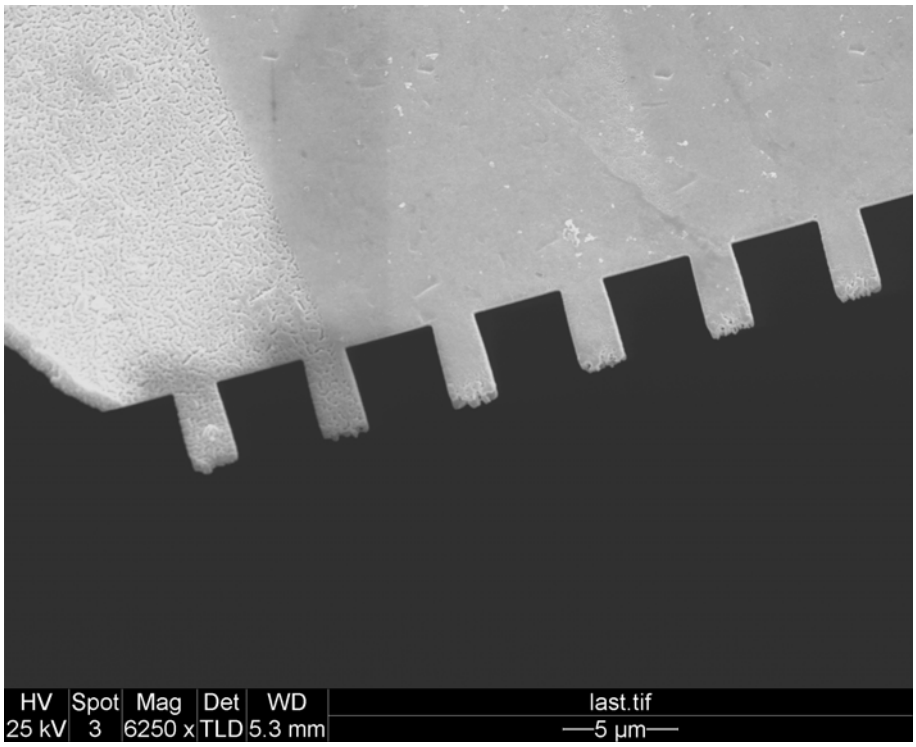

Figure 2.5: "Teeth" cut into a working area. Ion beam is incident into the page.

Once the "teeth" are cut the sample has to be reoriented (Figure 2.5). Whilst it is possible to produce pillars without reorientation by initially aligning the working edge to point towards the ion beam source and use the FIB masking features to mill top-down, the downsides would be

both poor control over the quality of the pillar's sides and the natural tapering present in the ion beam's shape – in other words, the pillar's sides would not be parallel to each other using the top-down method.

The reorientation changes the angle of tilt between the ion beam emitter and the sample working edge by 45 degrees. From this point, polish milling is carried out by shaping the pillar sides from two different orientations. Once a particular pillar thickness has been achieved the sample is rotated 180 degrees such that an axis perpendicular to the one of the previous milling direction is accessed. Once again, the required thickness is achieved with polish milling. As FIB has a tendency to smear the sides of the pillar at high currents, successively smaller currents are used to polish the sides of the pillar until the influence of the FIB is minimal (see Figure 2.6).

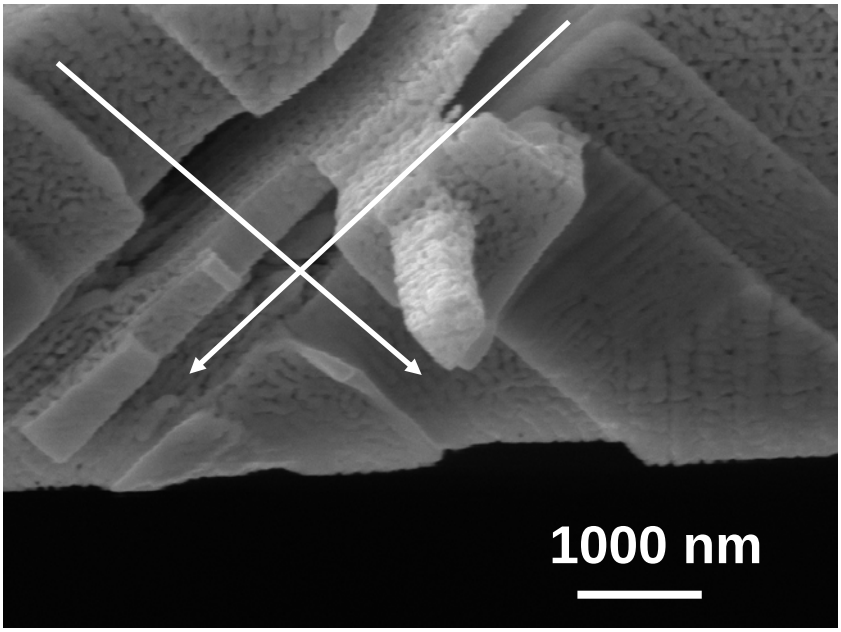

Figure 2.6: A pillar after successive polishing passes. Note the crossing directions of FIB emission orientations.

2.3 Production of disordered nanoporous metals

All production of disordered nanoporous metals was carried out through chemical or electrochemical dealloying of a binary alloy whose composition enables the formation of a solid solution phase. With this, the resultant sample is fully homogeneous and has a nanoscale microstructure, as large precipitates do not form.

Gold

AuAg ingots of composition $Au_{0.35}Ag_{0.65}$ at.% (see Figure 2.7) were prepared by arc-melting high-purity (99.99+%) Au and Ag purchased from Alfa-Aesar. Ingots were sealed in quartz tubes in an airless atmosphere and homogenized at 1223K over several days.

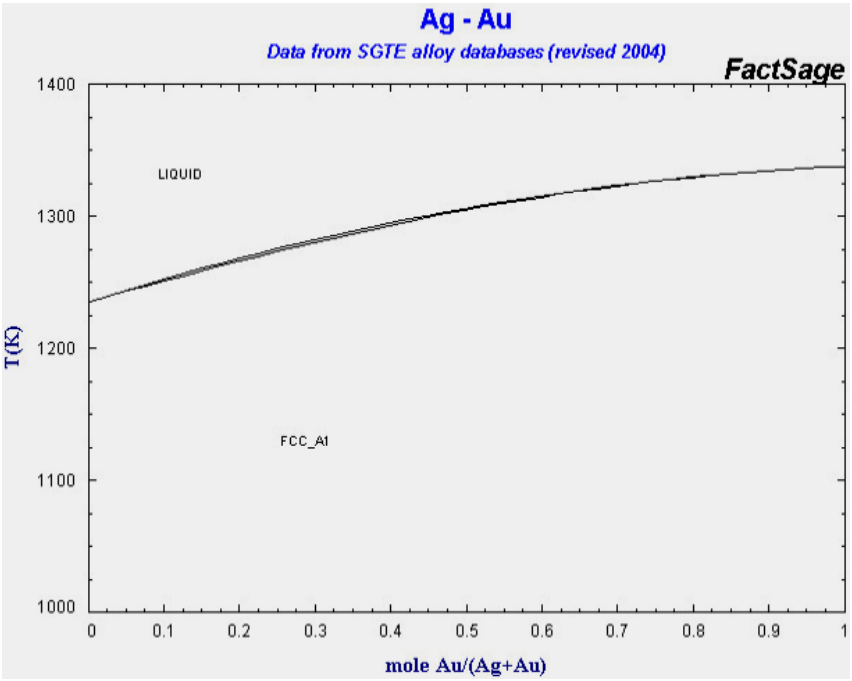

Figure 2.7: Phase diagram for the AgAu binary alloy, Centre for Research in Computational Thermochemistry [9]. A solid solution forms at all compositions.

This step is self-explanatory: the initially-prepared ingot may not have a fully homogeneous microstructure due to uneven cooling inside the arc furnace or during handling, and the homogenization step mitigates such inconsistencies. Dealloying was carried out using a standard three-electrode Potentiostat electrochemical cell (*µAutolab type III/ Fra2-Eco Chimie)*, with the AuAg sample at the working electrode, platinum mesh at the counter electrode and Ag-AgCl as a reference electrode. Dealloying was performed in 1M HNO_3 at ~ 600mV over several days until dealloying current was negligible. As the electrolyte environment is moderately hostile, the working electrode itself is typically chosen to be a platinum wire that can be wound around the AuAg ingot to ensure contact.

Copper

CuMn ingots of composition $Cu_{0.30}Mn_{0.70}$ at.% were prepared using an arc furnace. High-purity (99.99+%) Cu and Mn shot was purchased from Alfa-Aesar.

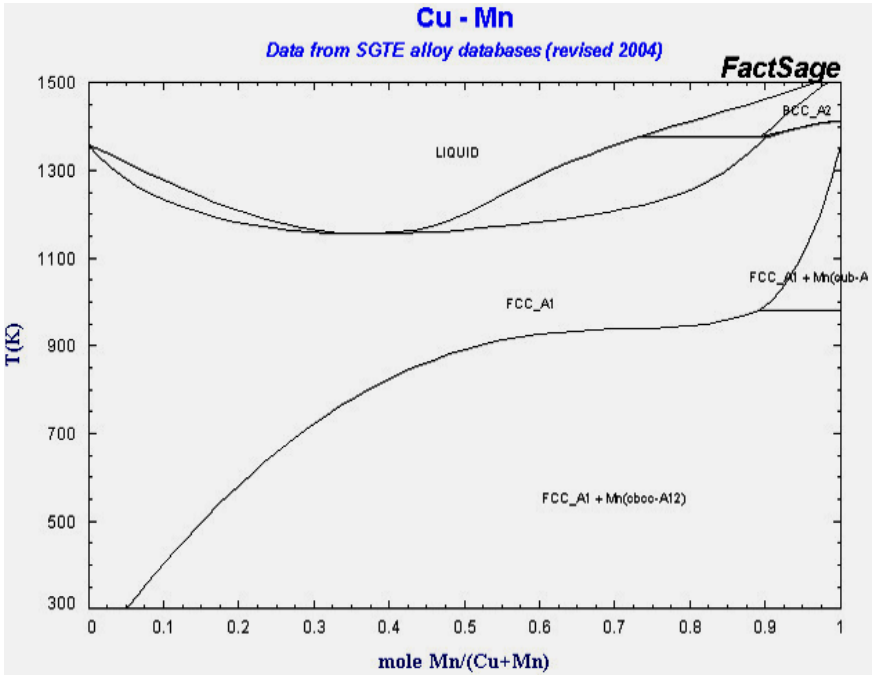

Figure 2.8: Phase diagram for the CuMn binary alloy, Centre for Research in Computational Thermochemistry [9].

Characterization techniques

Afterwards the ingots were vacuum-sealed inside quartz tubes and homogenized over several days at 900K. Ingots were then rapidly quenched to prevent formation of secondary phase in an otherwise CuMn solid solution. The composition and quenching process were selected due to the behaviour of the CuMn alloy.

As can be seen from the phase diagram in Figure 2.8, in a slowly cooling $Cu_{0.30}Mn_{0.70}$ alloy a secondary Mn phase will nucleate below approximately 700K. Rapid quenching prevents this by forcing the alloy to cool so quickly that the secondary phase does not have time to form. Dealloying was carried out in an experimental setup similar to those of the dealloying of AgAu. Dealloying was performed in 0.05M HCl at -550mV over 4 hours until dealloying current was negligible.

CuNi Alloy

Ingots of $Ni_{0.25}Cu_{0.25}Mn_{0.5}$ were prepared by arc-melting high-purity Ni, Cu and Mn. The ingots were homogenized at 1173K for 24 hours and then rapidly quenched in water. Dealloying was carried out using the same apparatus as above in 0.1M $(NH_4)SO_4$ at -0.65V vs. SCE for 1 hour[11].

2.4 Production of ordered nanoporous metals

Ordered nanoporous metals were always produced using bottom-up inverse templating techniques.

Nanosphere templating

Polystyrene nanospheres suspended in aqueous solution with diameters of 50, 100, 200, 500 and 1000μm were purchased from Alfa Aesar and Bangs Laboratories. Solutions were diluted down to a range of 0.1-1%.

As nanospheres will gradually sediment due to gravity and ultrasonic treatment can lead to warping of nanospheres due to heating, solutions were vigorously stirred prior to experimentation.

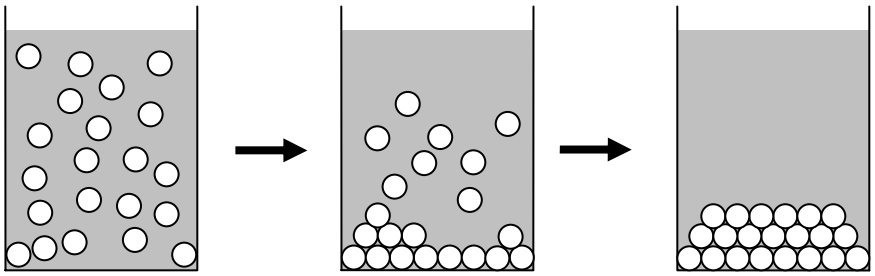

Figure 2.9: Schematic diagram of the sedimentation self-assembly of nanospheres.

Teflon molds were fabricated through machining. The molds had square cavities extending through the entire thickness of the mold spaced at even intervals across the length of the mold.

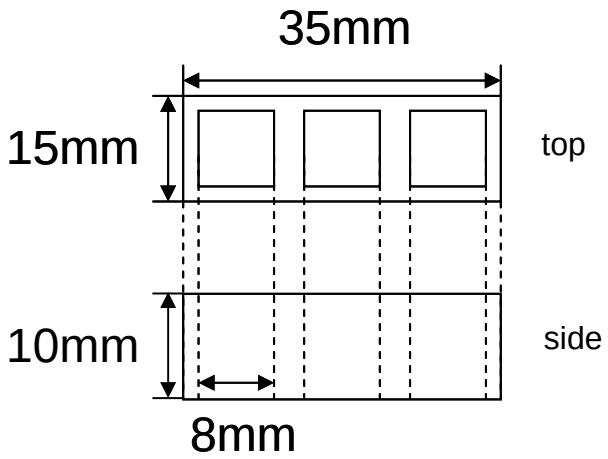

Figure 2.10: Teflon mold from top and side projections.

The Teflon molds were attached to standard microscope slides using vacuum grease such that the microscope slide would cover the cavities from one side entirely. Once properly affixed, nanosphere solution was

poured inside the cavities. The assembly was then placed under a glass cover large enough to fit it and several containers of water such that a saturated atmosphere would be formed under the glass cover to prevent evaporation. The setup was then left for 3-4 days to allow nanospheres to sediment under gravity. Afterwards the glass cover was removed to allow the water to evaporate from the nanosphere solution over 2-3 days (see Figure 2.9 and Figure 2.10).

Once the nanospheres were fully dry, the Teflon mold was removed to leave the nanosphere deposits on the glass slide. The nanosphere deposits on the glass slide could be removed using tweezers, as they were sufficiently robust for manual handling. If any nanosphere deposits adhered to the Teflon mold, they could be removed in the same way.

To increase the toughness of the template furnace treatment was performed. Depending on sphere size, templates were left in a furnace at 43°C for 8-10 minutes to allow necks to form between adjacent spheres.

Diblock copolymer templating

Gyroidal polymer templates were produced by Ivana Vukovic, and the full discussion of the process can be found in her thesis [10]. The process has the possibility to produce a wide variety of diblock morphologies depending on the composition of the various components present; however, the gyroid morphology is the one we desire and the only one used. For the sake of completion, we quote the section most relevant to this chapter and this investigation in general:

“Films of the supramolecular complexes were cast by dissolving the PtBOS-b-PS-b-P4VP [poly(*tert*-butoxystyrene)-*block*-polystyrene-*block*-poly(4-vinylpyridine)] triblock copolymer and PDP [3-Pentadecylphenol] in chloroform. The concentration of polymer was

maintained below 2wt% to ensure homogeneous complex formation, and the solution was stirred for a couple of hours at room temperature. Afterward, the solution was poured into a glass Petri dish, which was subsequently placed into a saturated chloroform atmosphere. Chloroform was allowed to evaporate slowly during several days at room temperature. Subsequently, the samples were heated at 130°C for half an hour. The low molecular weight amphiphile was removed by stirring a piece of the film in ethanol for three days at room temperature resulting in the formation of the nanoporous template for metal deposition.**"**

A traditional electroplating procedure was used to coat templates with metallic films. For this process, a three-electrode cell is required with a working, reference and counter electrodes and an electrolyte that is, in the case of this procedure, also the source of gold ions.

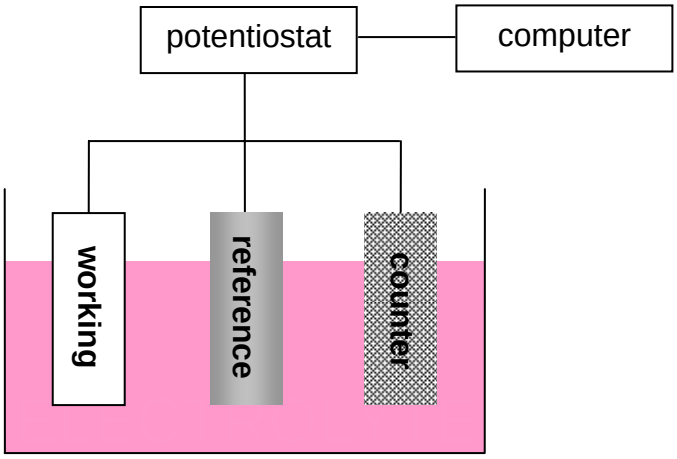

Figure 2.11: Schematic diagram of three-electrode setup with an Autolab potentiostat.

During electroplating, the template is attached to the working electrode, the reference electrode is either Calomel or Ag-AgCl, and the counter electrode is typically platinum mesh. Plating is carried out at

potentiostatic conditions that are controlled by the combination of potentiostat and proprietary control software setup in an attached computer. The same apparatus measures the resulting plating current and provides visual output in the form of a scatter graph. The potential for plating varies by plating metal. (see Figure 2.11) The precise conditions for electroplating will be discussed later in the thesis.

Electroless plating is a general term that refers to the group of plating methods that deposit metal onto a substrate surface through means of chemical reaction. The advantage of this technique is that it does not require the presence of an electrochemical setup and, by extension, a conducting substrate. As the reaction occurs based on the presence of certain catalyst sites, electroless plating offers a much more thorough plating coverage of a non-conducting template. A typical electroless plating process consists of three steps: sensitization, activation and plating. The first step that involves the adsorption of metal ions onto the surface enables the second step, where these metal ions are substituted with a catalyst. The catalyst then enables the third step, where the plating metal ions are reduced by a reducing agent present in the solution and deposit onto the template. The specifics of electroless plating used in this investigation are detailed in a later chapter.

The method of template removal varied by the material of the template and of the plated metal. In the case of organic templates, if the plated material was nickel then samples were left overnight in a furnace at 450°C. If the plated material was gold then samples were left overnight in chloroform solution in a fume hood and afterwards vigorously washed with deionized water. For silica templates HF treatment was performed: samples were left overnight in HF and rinsed in water afterwards.

2.5 Picoindentation

Ex situ nanoindentation followed by post mortem transmission electron microscopy does not allow for direct observation of the microstructure

during indentation and thus lacks the possibility to monitor deformation events and the evolution of structures as the indentation proceeds. Also, the microstructure observed after indentation is generally different from that of the material under load, due to recovery during and after unloading. The recently developed technique of in-situ nanoindentation in a transmission electron microscope [11,12,13,14,15,16] does not suffer from these limitations and allows for direct observation of indentation phenomena. Furthermore, as the indenter can be positioned on the specimen accurately by guidance of the TEM, regions of interest such as particular orientations can be specifically selected for indentation. For a review see [17,18,19,20,21,22].

The first indentation holder was developed in the late 1990s by Wall and Dahmen [11,12] for a high-voltage microscope at the National Center for Electron Microscopy (NCEM) in Berkeley, California. In the following years, several other stages were constructed at NCEM with improvements made to the control of the indenter movement and the ability to measure load and displacement. In the work described in this thesis a device dedicated to load and displacement rate controlled measurements was used as developed by Hysitron (Hysitron Inc., Minneapolis, MN, USA) [23].

The indenter tip is mounted on a piezoceramic tube as illustrated in [13]. This type of actuator allows high-precision movement of the tip in three dimensions, the indentation direction being perpendicular to the electron beam. Coarse positioning is provided by manual screw drives that move the indenter assembly against the vacuum bellows. The indenter itself is a flat punch or a Berkovich-type diamond tip, which is boron-doped in order to be electrically conductive in the TEM. The goniometer of the TEM provides a single tilt axis, so that suitable diffraction conditions can be set up prior to indentation.

In the holder for the JEOL2010F, a capacitive sensor monitors the load and displacement during indentation. The displacement signal is used as input for a feedback system that controls the voltage on the

piezoceramic tube based on a proportional-integral-derivative (PID) algorithm [24]. The indentation is therefore displacement controlled and can be programmed to follow a predefined displacement profile as a function of time.

The need for a separate load and displacement sensor as implemented in the holder is mainly due to the complex response of the piezo tube. If the response was fully known, the load could be calculated at any time during indentation from the displacement (which can be determined directly from the TEM image) and the characteristics of the load frame [25]. Ideally, the correlation between the applied voltage and the displacement of the piezo element is linear. However, hysteresis and saturation effects lead to significant nonlinearities. Moreover, as lateral motion is achieved by bending the tube, the state of deflection strongly affects the response in the indentation direction as well.

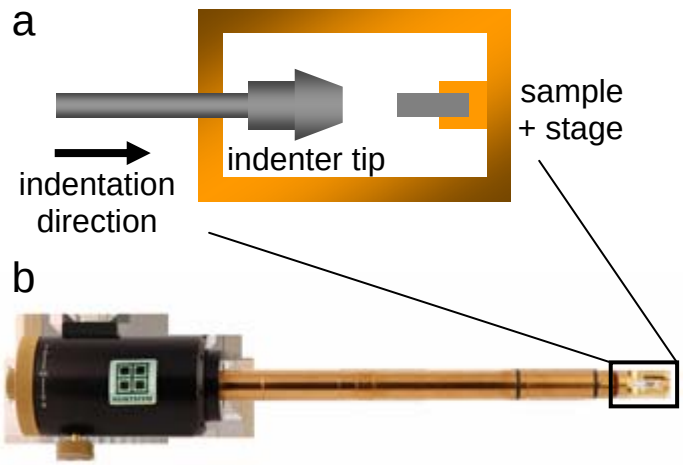

Figure 2.12: Schematic diagram of Hysitron picoindentation tip and stage (a) and Hysitron picoindenter apparatus (b) [26].

Calibration measurements of the piezo response in vacuo at 12 points across the lateral range showed an average proportionality constant of 0.12µm/V with a standard deviation as large as 0.04µm/V. Although during indentation, the deflection of the tube is approximately constant

and the response becomes more reproducible, the abovementioned hysteresis and saturation effects still complicate the measurement of the load. The implementation of a dedicated load sensor, as in the new holder, is therefore essential for obtaining reliable quantitative indentation data.

Nanopillars of porous metal that were prepared through FIB milling were installed on the Hysitron picoindenter stage. Pillar deformation was induced using the dual beam FIB/scanning electron microscope (SEM) microscope (Lyra, Tescan, CZ) apparatus. Each pillar was aligned perpendicular to the beam to fully expose one of its faces. This leaves the opposing face in the ion beam's shadow. Variation was possible in probe current and size of exposed area. Ion beam energy was maintained constant at 30kV, and beam currents of 1, 10, 40 and 150pA were selected for the experiment. We note that the presented values are software-controlled current presets, and may vary from the actual beam current emitted by the ion beam source. In every case, true ion beam current values are used. Exposure times varied between 1 and 300s, depending on ion beam current used.

2.6 Actuation and cyclic voltammetry

Actuation and cyclic voltammetry (CV) in general was performed using the same three-electrode setup as described in the electroplating section (see also PhD thesis of Eric Detsi [27]). The reference electrode used was either Calomel or Ag-AgCl, most commonly the latter. While platinum mesh was commonly used as a counter electrode, often nanoporous gold blocks were used as a counter electrode to increase the amount of surface area for reaction. Actuation was mostly performed on extremely fragile ordered nanoporous nickel samples which could not be directly connected to an electrode. Instead, a gold wire was attached to a gold foil "stage" onto which the nickel sample could be placed. No affixing was performed to ensure contact. The details of the cyclic voltammetry parameters are discussed in the next chapter.

Actuation required additions to the CV setup for the purpose of measure the displacement induced through injection of charge. Actuation was performed in a large flat Petri dish that was placed on the stage of an optical microscope. The microscope was arranged to be able to observe the sample on the gold foil stage and to be able to zoom in on an edge of the sample to clearly resolve any possible deformation. The microscope had to it attached a video camera which was able to output in real-time to a computer with recording software.

Cyclic voltammetry sweeps with a triangular wave pattern were performed in the range where nickel would see a characteristic redox pattern but where the gold stage would only provide a weak space charge contribution such that the results from the gold would not interfere with those from nickel. This range was from 0-0.5V. Deformation was continuously recorded over several sweeps.

2.7 References

[1] B Groen, *Misfit dislocation patterns studied with high resolution TEM*, Thesis University of Groningen, pp.108, 17 September 1999.

[2] P A Carvalho, *Planar defects in ordered systems*, Thesis University of Groningen pp.162, 26 January 2001.

[3] W Soer, *Interactions between dislocations and grain boundaries*, pp.132, 6 January 2006.

[4] Z Chen, *Superplasticity of coarse grained aluminum alloys*, Thesis University of Groningen, pp.122, 10 September 2010

[5] M Knoll, Aufladepotentiel und Sekundäremission elektronenbestrahlter Körper. Zeitschrift für technische Physik 1935, 16, 467-475.

[6] J Th M De Hosson, 'Transmission electron microscopy of metals and alloys', in: S. Amelinckx, D. Van Dyck, J. Van Landuyt, and G. Van Tendeloo (eds.), *Handbook of Microscopy*, volume III, Weinheim: Wiley-VCH, 1997, pp.5-111.

[7] D B Williams, C B Carter, Transmission Electron Microscopy: A Textbook for Materials Science. Springer 2009.

[8] J M Cowley, in High-Resolution Transmission Electron Microscopy (eds. P. Buseck, J. Cowley, L. Eyring), Oxford University Press, New York (1988) p. 3.

[9] http://www.crct.polymtl.ca/FACT/documentation/SGTE/SGTE_Figs.htm

[10] I Vukovic, *Block Copolymer Template-Directed Synthesis of Well-Ordered Metallic Nanostructures*, Groningen University Press, Groningen, 2013

[11] M A Wall, U Dahmen (1997) Microsc Microanal 3: 593

[12] M A Wall, U Dahmen (1998) Microsc Res Tech 42:248

[13] E A Stach, T Freeman, A M Minor, D K Owen, J Cumings, M A Wall, T Chraska, R Hull, J W Morris Jr, A Zettl, U Dahmen (2001) Microsc Microanal 7:507

[14] A M Minor, J W Morris Jr, E A Stach (2001) Appl Phys Lett 79:1625

[15] A M Minor, E T Lilleodden, E A Stach, J W Morris Jr (2002) J Electron Mater 31: 958

[16] A M Minor, E T Lilleodden, E A Stach, J W Morris Jr (2004)J Mater Res 19:176

[17] W A Soer, J T M De Hosson, A M Minor, E A Stach, J W Morris Jr (2004) Mater Res Soc 795:U9 3 1

[18] W A Soer, J T M De Hosson, A M Minor, J W Morris Jr, E A Stach (2004) Acta Mater 52: 5783

[19] J T M De Hosson, W A Soer, A M Minor, Z Shan, E A Stach, S A Syed Asif, O L Warren (2006) J Mat Sci 41:7704

[20] J T M De Hosson, W A Soer, A M Minor, Z Shan, S A Syed Asif, O L Warren (2006) Microscopy and Microanalysis, 12: Issue S02, 890

[21] W A Soer, J T M De Hosson, A M Minor, Z Shan, S A Syed Asif, O L Warren (2007) Applied Phys Lett,

[22] W A Soer, J T M De Hosson, Electron Microscopy at High Resolution, Ed. Florian Banhart, World Scientific, 2008, 1

[23] J Th M De Hosson, *Handbook of Nanoscopy*, Weinheim: Wiley-VCH, 2012, pp.1097-1151.

[24] O L Warren, S A Downs, T J Wyrobek (2004) Z Metallk 95: 287

[25] A M Minor (2002) Ph D thesis ,University of California, Berkeley

[26] PI 95 TEM PicoIndenter® with the performech™ control unit, *www.hysitron.com*

[27] E Detsi, *Metallic muscles: enhanced strain and electrolyte-free actuation*, Thesis University of Groningen, pp.120, 23 November 2012

Chapter 3

PROCESSING AND MANUFACTURING OF NANOPOROUS METALS

3.1 Introduction

There is no doubt in the utility of actuating materials in a wide variety of applications. Piezoelectric ceramics have been used in microelectronics, home entertainment, sensing and the medical industry to great effect. With polymers, ceramics and carbon nanotubes proposed as likely actuating materials, there has been little to no discussion on the use of metals as actuators.

Gleiter *et al.* proposed in 2001 the use of an external electric field to modify properties such as charge carrier density and the like in a nanostructured solid. The proposal presented that such property modification would enact changes in the surface regions of the solid, which would, when considering the nanostructuring, attain a large fraction of the total sample volume [1]. The principle is akin to that of the field effect seen in semiconductor electronics. While sound in theory when applied to metals, the chief obstacle in applying this principle to metals is the efficient electronic screening caused by a high conduction electron density that restricts space-charge layers to the first few atomic depths of the metal's surface. This obstacle, however, can be overcome by returning to Gleiter's proposal and applying this field

effect to a nanostructured metal where, indeed, the surface-to-volume ratio is typically extremely high. Weissmuller *et al.* first tested this proposal with nanostructured Pt, produced from the consolidation of commercial Pt black, immersed in a variety of electrolytes – H_2SO_4, $HClO_4$ and KOH. By measuring *in situ* with diffractometry and dilatometry, they observed a reversible deformation that occurred in phase with variation in the electric field (Figure 3.1).

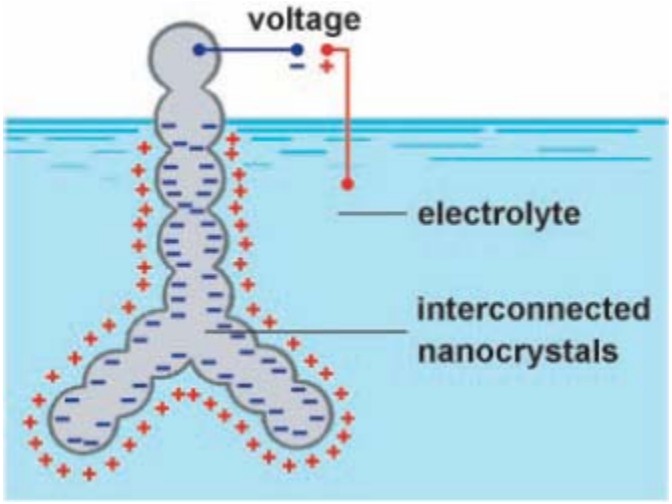

Figure 3.1: Schematic illustration of the distribution of charge across an interconnected array of nanoparticles in an electrolyte [2].

In this experiment, the proposed principle behind the charge-induced deformation lies in the mechanics of charge injection into the surface of the metal. Specifically, surplus electrons in the band structure of the surface atoms change the band structure's shape, which in turn influences the surface stress state. This proof-of-concept experiment demonstrated that, unlike in other types of actuator materials, the charge-induced deformation ability of metals is strongly influenced by their microstructure and, specifically, the nature of their porosity and, by extension, the surface-to-volume ratio that is present within the material. By varying the degree of porosity, the interconnectivity of the

pores and pore size the actuation properties of nanostructured metals can be varied.

Proceeding from Weissmuller *et al.*'s work on nanostructured platinum, Kramer *et al*. presented that an actuating device must be precisely and reproducibly shaped, with the capacity to be bonded to a component that transmits displacement and load. Their solution was to use nanoporous metals produced from a solid solution alloy through dealloying and attaching the resulting nanoporous metal to a solid foil to produce a cantilever beam that would experience a biaxial stress during the metallic actuation event and thus undergo a bending displacement [3].

3.2 Motivation for microstructure, order vs. disorder

The deformation observed in disordered nanoporous metals during actuation raises several questions on the behaviour of similar materials but with different quality or degree of porosity. Amongst these is the consideration of the effects that ordering might have on the actuation response. After all, crystalline materials have preferential deformation planes based on the packing fraction of atomic planes. Would a similar effect be observed in an ordered nanoporous metallic foam, where a unit cell shape is the equivalent of a crystallite, and a three-dimensional arrangement of such unit cells is the equivalent of a grain?

Which metals are to be used in conjunction with an inverse templating process is dependent on two separate considerations. The first consideration is that, of course, the metal itself must be compatible with the process in the first place, which quickly becomes an issue of the metal's history of utility in industry and academia. For example, the history of the use of gold and silver for plating, i.e. applying a thin layer of gold, silver or bronze onto an otherwise mundane object for the purposes of protection or aesthetics – gilding – has been used in ancient Egypt and China, although most such gilding was accomplished using

the hammering of gold leaf or through the use of gold paint (Figure 3.2). However, even the more sophisticated method of electroplating of gold and silver were discovered over two hundred years ago.

Figure 3.2: Gold-plated statue of Avalokiteshvara, 18th century, Rome Natural Museum of Oriental Art.

As such, a large amount of literature and research exists on the use of gold and silver for electroplating and not, for example, for aluminium or nickel. Recent developments in chemical so-called electroless plating have created opportunities for the use of copper and nickel for template-based production, but the pool of materials available still remains small.

The second consideration is that, while the metal may be compatible with whatever means of plating is selected, the means of plating may

not be compatible with the template and post-plating procedures. Finally, for the sake of consistency and comparison, it would be ideal if the metals selected could be deposited on all templates selected and with all deposition methods used. This leaves a very limited selection of materials available, with Au at the top of the list as the most commonly-used material with the largest amount of background literature for its use.

3.3 Nanosphere inverse templating.

A nanosphere template is a prime example of a three-dimensionally ordered, stable, self-assembling template that is extremely easy to produce. As the only requirements for the production of the template are spheres that are insoluble in and heavier than water, the material selection for the spheres themselves is quite varied. In our experiments, we have used silica, polystyrene and poly(methylmethacrylate) (PMMA) nanospheres. Typically, nanosphere templates are assembled by allowing layers to deposit across a meniscus that develops on an angled glass slide as the liquid holding the nanosphere suspension evaporates. This technique is known to produce thin layers of a few dozen nanospheres at most and, while entirely valid, is insufficient for our experiment, where the requirement is a free-standing template. Additionally, we want a porous metallic sample that can be evaluated in a similar way to that of a disordered nanoporous metal, samples of which can be up to 1mm in the smallest dimension. Another concern is the use of the template for electroplating – a valid contact for a working electrode has to be present.

Silica nanospheres

Silica (SiO_2) nanospheres when used in the context of a self-assembling template offer the properties of being highly chemically and physically stable, allowing them to be used in potentially hostile environments. This advantage can also act as a hindrance, as a key principle during

inverse templating is the easy removal of the template without adverse effects on the metal inverse image deposited into the template. A highly stable template would thus be difficult to remove and might require unusual processing in the final stages of preparation.

Silica nanospheres are typically produced in the industry using reverse microemulsion, flame synthesis or the sol-gel process. The sol-gel process is a long-time favorite for the production of ceramic materials due to its ability to form pure and homogeneous products at mild conditions. Sol-gel involves the hydrolysis and condensation of metal alkoxides or inorganic salts, provided they have a silicon component, in the presence of a catalyst. As a result of this step silanol groups are formed in solution and condensation forms bridges between the silanol groups that form the silica structure as a colloid in solution. Individual silica particles form through spontaneous nucleation and grow in size due to aggregation and agglomeration [4].

Flame synthesis is a broad term describing the production of nanoparticles from a gas by means of a so-called gas-to-particle conversion that encompasses the use of flame, hot-wall, furnace, plasma furnace or laser and sputtering reactors, or vapor-phase evaporation-condensation processes. Alternatively, during Flame Spray Pyrolysis a liquid solution that contains the particle precursor is combusted with a gaseous or liquid fuel. During this process, solution droplets disintegrate upon entering the flame resulting in separated individual nanoparticles. In all cases, the disadvantage of flame-based synthesis is the difficulty in controlling the final morphology and composition of produced particles due to the fast processes involved [5].

Microemulsion is a wet process involving the dispersion of an insoluble liquid in a continuous medium to form nanosized droplets. When a surfactant is introduced, the polar molecules within the surfactant arrange themselves around the droplet, forming a nanosized object known as a micelle. This arrangement can be used to construct nanospheres with extremely high shape fidelity. In addition, the particle

size can be controlled by varying the parameters of the microemulsion. The drawbacks of this process are the typically high costs involved, as well as the difficulty of the removal of surfactants [6].

Polystyrene nanospheres

Colloidal silica nanospheres of varying diameters in solution were purchased from Polysciences, Inc. Colloidal polystyrene nanospheres of varying diameters in solution were purchased from Alfa Aesar GmbH & Co KG. Colloidal poly(methylmethacrylate) nanospheres of varying diameters in solution were purchased from Bangs Laboratories Inc. Nanosphere solutions were diluted to a variety of concentrations, ranging from 0.1-1%.

If used in conjunction with a Teflon mold, the Teflon mold was attached to a silicon wafer or glass slide substrate with vacuum grease. Then, the diluted nanosphere solution was poured into the mold and allowed to settle in a saturated atmosphere over 3-4 days. The saturated atmosphere was achieved by surrounding the mold with containers with distilled water and a glass cap was placed over the arrangement. After the settling period, the cap was removed and the water was allowed to evaporate out of solution.

Electroplating (gold) and Electroless plating (nickel)

Gold electroplating solution was purchased from Caswell. Au electrodeposition was carried out using a standard three-electrode cell in conjunction with an Autolab potentiostat with associated proprietary software. Au was deposited at the working electrode. Calomel was used as a reference electrode and Pt mesh was the counter electrode. Electrodeposition was carried out at -0.9V at potentiostatic conditions for 30 minutes.

A three-step process was used for electroless plating of nickel. In step 1, the template is immersed in $SnCl_2$/HCl to allow the adsorption of Sn^{2+}

ions onto the template surface. In step 2, the sample is washed and immersed in $PdCl_2$/HCl to allow the formation of Pd sites through the redox reaction $Sn^{2+} + Pd^{2+} \rightarrow Sn^{4+} + Pd^0$. The Pd sites catalyze the metal deposition process in step 3. Step 3 is performed in a bath composed of nickel sulfate as the nickel source, sodium citrate as the complexant, lactic acid as the buffer and dimethyl amine borane (DMAB) as the reductant. The pH of the nickel bath is adjusted to 7.0 using ammonium hydroxide. A more detailed explanation of the process and chemicals used is available for reading in the thesis by Dr. Ivana Vukovic, who performed the electroless plating process [7]. The same procedure was used for the plating of diblock copolymer templates.

Poly(methylmethacrylate) and polystyrene nanosphere templates were removed by soaking overnight in toluene. Silica nanosphere templates were removed by soaking in buffered hydrofluoric acid (BHF) over 3 hours.

Template assembly

Prior to use, colloidal nanosphere solutions often required extensive agitation as, by design, the nanospheres will deposit on the bottom of the solution's container if left over several days. While stirring was often enough to satisfactorily break up significant deposits, ultrasonic bath treatment was performed to attempt to accelerate the process. It was observed that, while ultrasonic treatment had no adverse effects on silica nanospheres, polymer nanospheres underwent severe deformation and physical agglomeration, as shown in Figure 3.3.

Throughout all gravity-assisted deposition of colloidal nanospheres procedures a tendency was observed where larger nanospheres tended to order more correctly and at a longer range than smaller ones. The diameters of nanospheres deposited were 50, 100, 200, 500 and 1000 nanometres. 50nm nanospheres were exclusively silica, as we were unable to find polymer nanospheres of this size, and 100nm onwards

were available in polystyrene (PS) and poly(methylmethacrylate) (PMMA). A batch of ~400nm silica nanospheres was later used. (Figure 3.5)

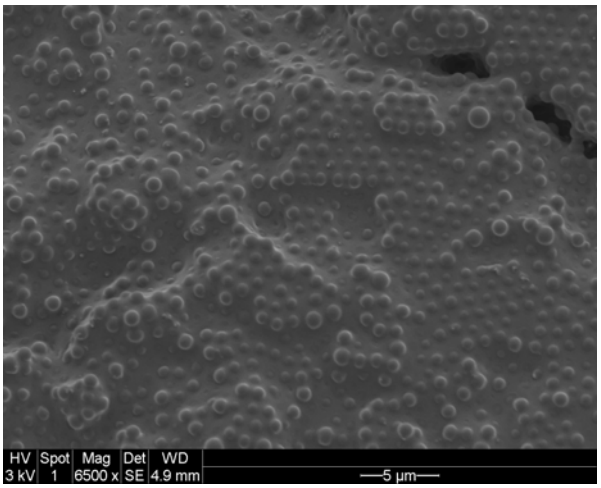

Figure 3.3: SEM micrograph of severe agglomeration of PMMA nanospheres after ultrasonic treatment.

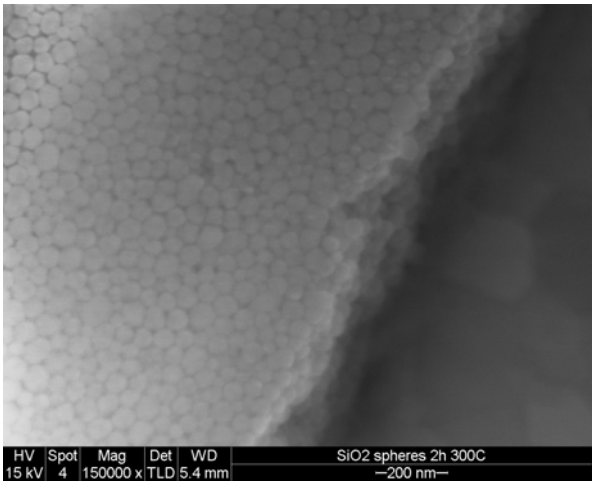

Figure 3.4: SEM micrograph of surface layer and depth fracture of gravity-deposited 50nm silica nanosphere template.

A typical issue endemic to the use of the particular batch and brand of silica nanospheres that we ordered was the lack of monodispersity in

nanosphere sizes. Worse yet, there are clear cases where particle shape is grossly non-spherical, seen in Figure 3.4. The end result is that templates constructed from 50nm silica nanospheres had poor to no ordering and a lack of homogeneity and reproducibility.

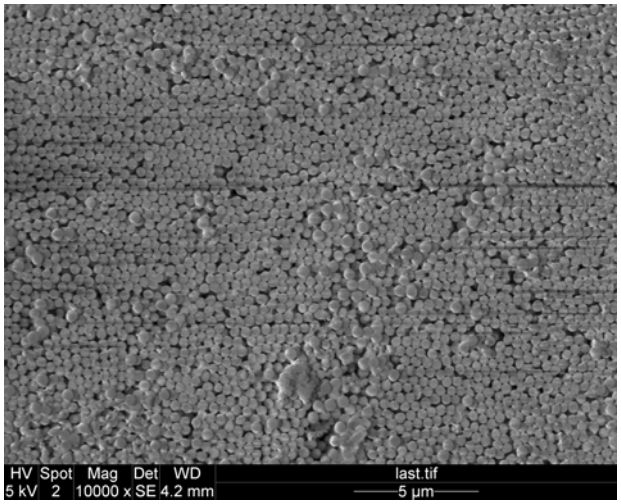

Figure 3.5: SEM micrograph of surface layer of gravity-deposited 400nm silica nanosphere template.

As a comparison, a template later constructed from 400nm silica nanospheres showed both improved quality of nanospheres as well as a stronger ordering (Figure 3.5). As can be seen in Figure 3.9, surface inhomogeneities are present in the large nanospheres.

The majority of templates used in our experiments were produced from polymer nanospheres – polystyrene (PS) and poly(methylmethacrylate) (PMMA).

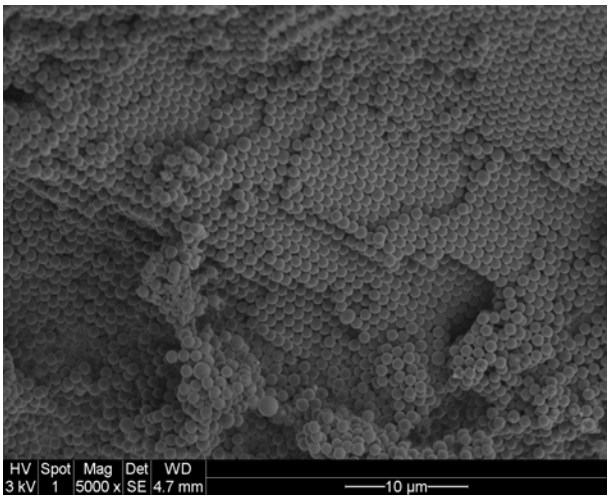

Figure 3.6: SEM micrograph of 1um poly(methylmethacrylate) nanospheres across a fracture surface.

In the case of the larger PMMA nanospheres, both ordering and shape fidelity have been observed to be high (Figure 3.6). Monodispersity was still low, however, preventing the development of sections with significant long-range order.

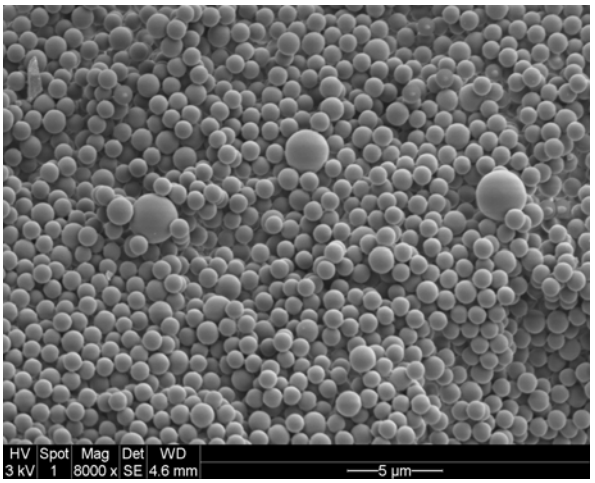

Figure 3.7: SEM micrograph of surface of nanosphere template produced by gravity-assisted deposition. Nanospheres of varying sizes can be clearly seen.

Poor quality of nanospheres was observed to be limited to particular sources. In our case, we had found that the majority of silica and PMMA nanospheres ended up as unusable due to the lack of monodispersity, seen in Figure 3.7. PS nanospheres, however, purchased from Alfa Aesar, were found to have good monodispersity across a variety of batches. It was observed that, given good monodispersity, that self-assembled templates had strong long-range ordering and good reproducibility. Nanospheres assembled in orientated grains. The size of such grains is a good measure of the quality of long-range order of the template. Large cracks were observed to develop along grain boundaries, as shown in Figure 3.8.

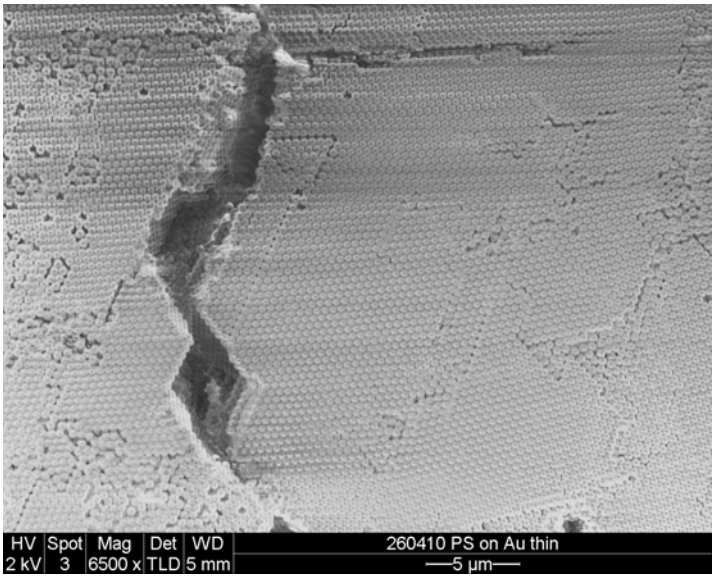

Figure 3.8: SEM of surface and fracture of polystyrene nanosphere template. Ordering is observed at the surface and inside the crack.

It was observed that the typical nanosphere template is brittle and weak. Using the Teflon mold method, thick templates could be assembled (up to 1mm thick). In such a state, templates could be handled carefully, but introduction into an aqueous medium for electro- or electroless plating frequently caused the templates to break apart spontaneously or with minor agitation of the solution. To strengthen templates, heat

treatment was investigated to induce minor sintering of the templates to improve bond strength between individual spheres and thus of the entire template. To facilitate this, nanosphere templates were heat-treated at varying temperatures for varying periods of time in a furnace.

Silica nanospheres, as shown in Figure 3.9, were treated for 24 hours at 900°C, which is a common procedure for the heat-treatment of silica nanosphere templates for use in the optical electronics industry [8].

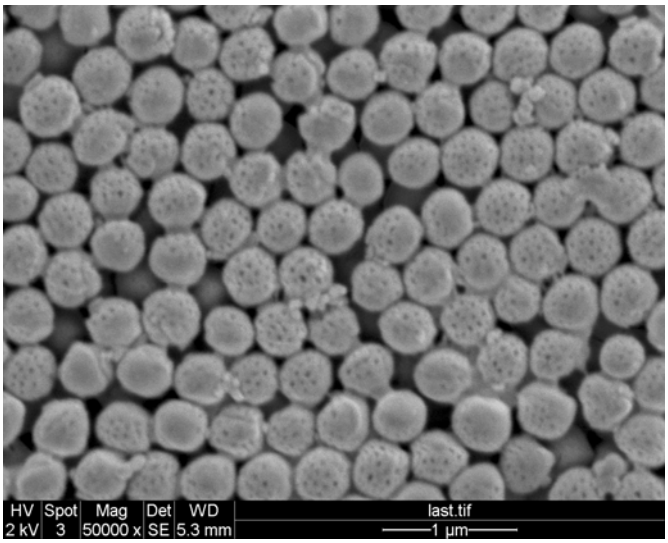

Figure 3.9: SEM micrograph of silica nanosphere template after heat treatment. Necks are clearly visible between spheres.

The much lower T(g) of PMMA and polystyrene nanospheres warranted a quicker heat treatment at lower temperature. While the T(g) of PMMA is approximately 125°C [9], differential scanning calorimetry (DSC) shown in Figure 3.10 results showed two reaction peaks, one at ~25°C and the other at ~68°C. The first peak shows the first effects of sphere fusion through neck formation, and the second comes from the full merging of spheres and the subsequent diffusion of air out of the resulting bulk.

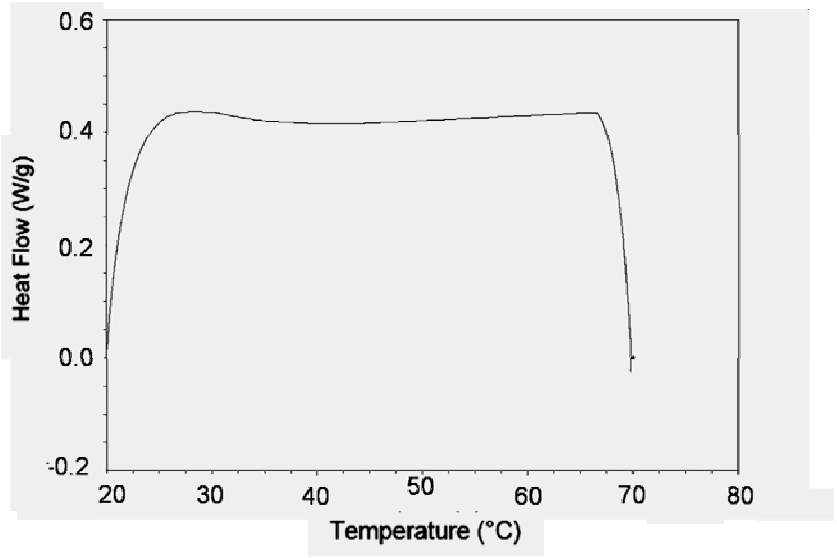

Figure 3.10: DSC of PMMA nanosphere template. Two temperature effect peaks are clearly visible.

Indeed, heat treatment close to the T(g) of PMMA demonstrated rapid fusion of nanospheres, such that the process could not be controlled, shown in Figure 3.11.

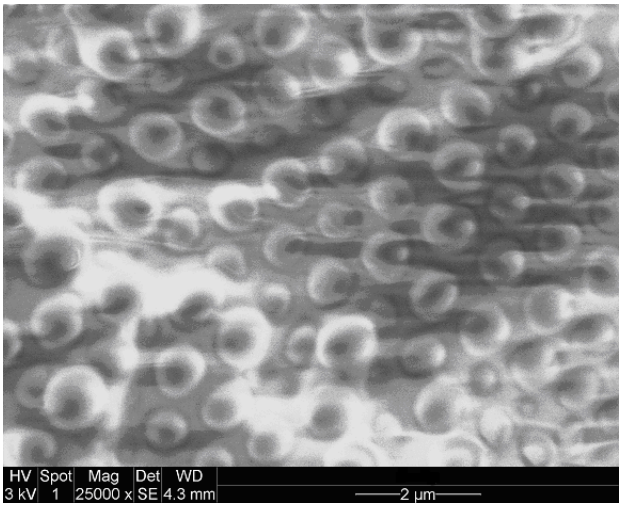

Figure 3.11: Nanospheres treated at 100°C for 5 minutes. Spheres are visible, but voids in between have been fully filled.

It was observed that treatment for up to 10 minutes at ~43°C yielded the best results where neck formation between spheres was visible and the resultant template was robust in handling and did not disintegrate rapidly when placed in aqueous solution. Simultaneously, voids retained their integrity during this treatment.

To develop an alternate option to the long deposition rate of gravity-assisted template self-assembly, assembly by centrifugation was attempted. Due to the significant heat induced in the process, only silica nanospheres could be used. Parameters of the process were 2000 rotations per minute (RPM) over 35 minutes. The result was a dense white solid, typical to that of a self-assembled nanosphere template, shown in Figure 3.12.

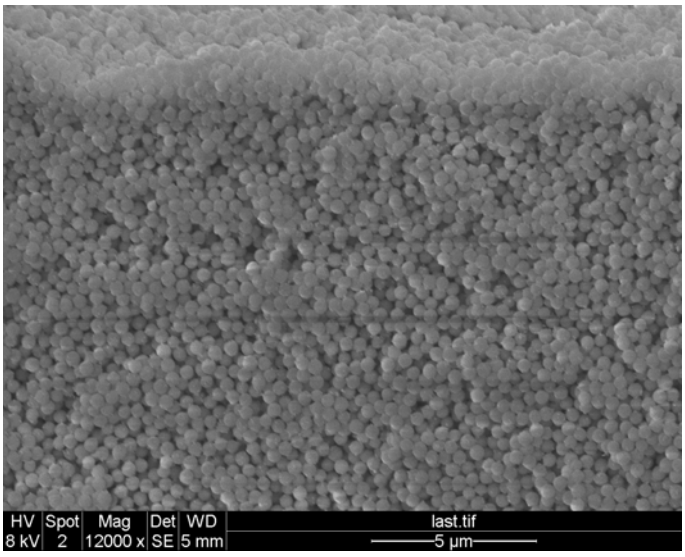

Figure 3.12: SEM micrograph of a centrifuge-assisted self-assembled silica nanosphere template.

The primary issue observed with centrifuge-assisted assembly was the extremely limited degree of ordering observed in the nanospheres. Small ordered areas were present, but no long-range order was ever observed.

During electro- and electroless plating (discussed in a later section) it was observed that plating on PS and PMMA nanospheres often resulted in poor deposition coverage quality leading to structural weakness and breakdown once the template was removed. This was attributed to the poor wetting qualities of the polymer nanospheres. To combat this, a sensitization process using poly(vinylpyridine) (PVP) was attempted on the nanospheres to improve wetting. However, it was determined that it was not possible to control the solution such that only a thin layer of PVP would be deposited on each individual sphere. Instead, every result showed that voids between nanospheres would be completely filled by PVP even at extremely low concentrations, shown in Figure 3.13.

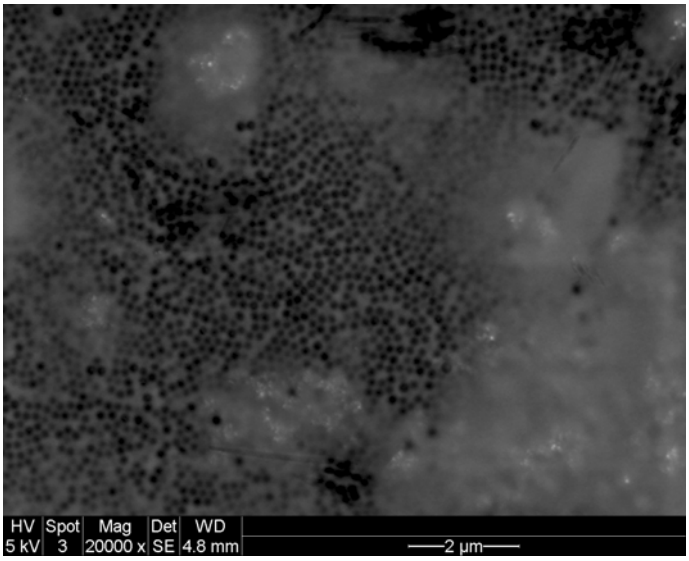

Figure 3.13 SEM micrograph of PVP-treated PS nanosphere template (black). Voids are completely filled by PVP (white).

As an electrical contact is required for electroplating, nanosphere templates assembled by means of gravity-assisted deposition were deposited on substrates with metallic surfaces. As electroplating would be carried out using gold ions, a gold surface was preferred to prevent mixed signals during the electroplating process. To facilitate this, we

used two types of surfaces. In the first case, a 10-nm gold layer was sputtered onto silicon wafers purchased from Kurt J Lesker, UK. Sputtering was carried out using equipment purchased from Kurt J Lesker, UK and sponsored by NanolabNL. In the second, 24-carat gold leaf purchased from Noris Blattgold GmbH was manually spread into as smooth a layer as possible onto standard laboratory glass slides.

In the case of silica wafers, nanospheres deposited smoothly to produce a well-ordered template in all cases. When using glass slides, however, adherence issues were observed between the gold surface and the nanosphere template such that, once assembled, the template would frequently detach from the substrate during handling, shown in Figure 3.14.

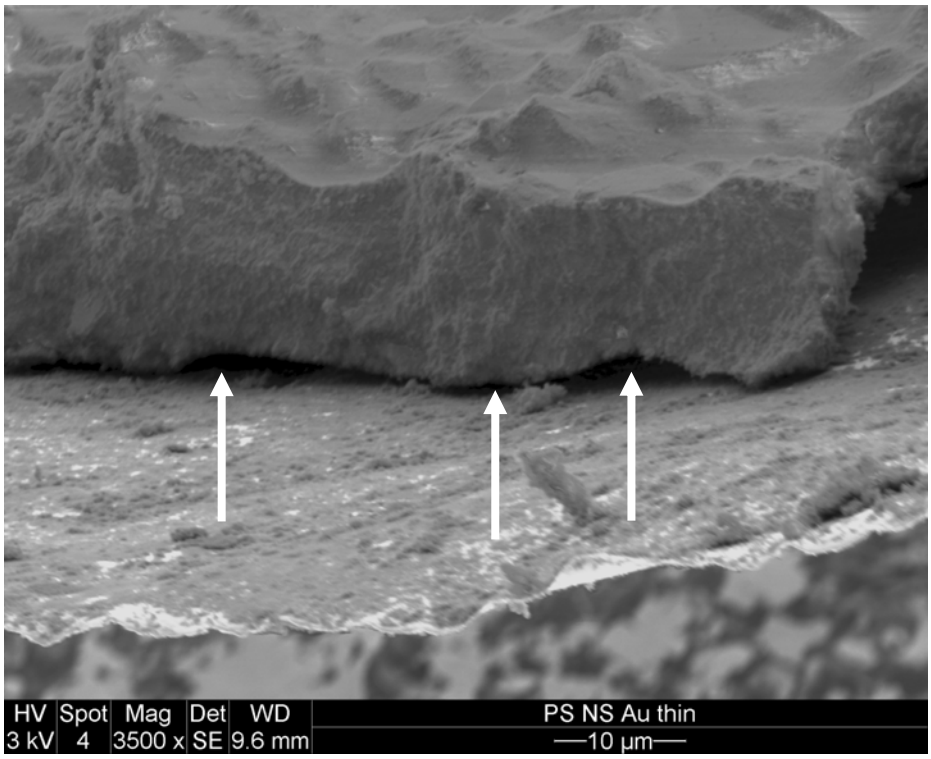

Figure 3.14: SEM micrograph of nanosphere template on gold foil. Delamination is indicated and clearly visible.

Template electroplating

Electroplating using a standard 3-electrode setup using an ionic Au solution produced a consistent deposition current for the duration of the experiment. After template removal, SEM observation was carried out of the resultant inverse nanosphere foam.

While a high-fidelity inverse reproduction of the nanosphere template was observed after electrodeposition experiments, shown in Figure 3.15. As nanospheres were observed to deposit in grains, with grain size determining the degree of long-range order, so were the grain sizes preserved during deposition. Issues, however, were observed with both template integrity and the resulting foam thickness.

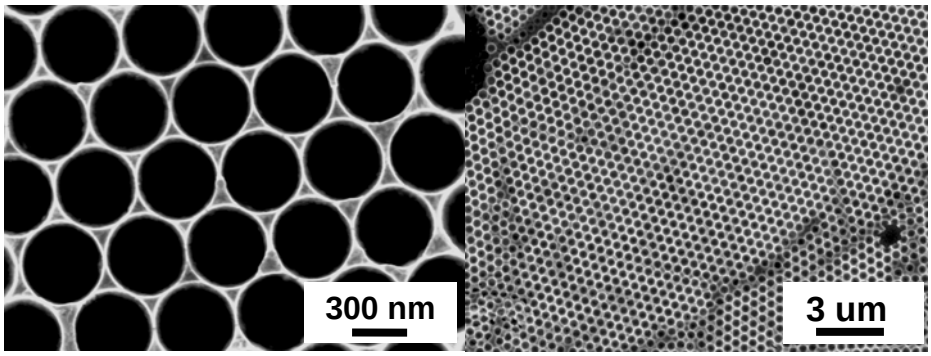

Figure 3.15: SEM micrograph of inverse nanosphere Au foam.

Specifically, templates assembled on silica-and-gold substrates were not heat-treated for strengthening to prevent possible damage to the submicron-thickness gold layer. Due to this, the nanosphere template often suffered loss of thickness, seen in Figure 3.16, as surface layers were washed away. This was a likely cause for the often monolayer thickness of the resulting metal foam.

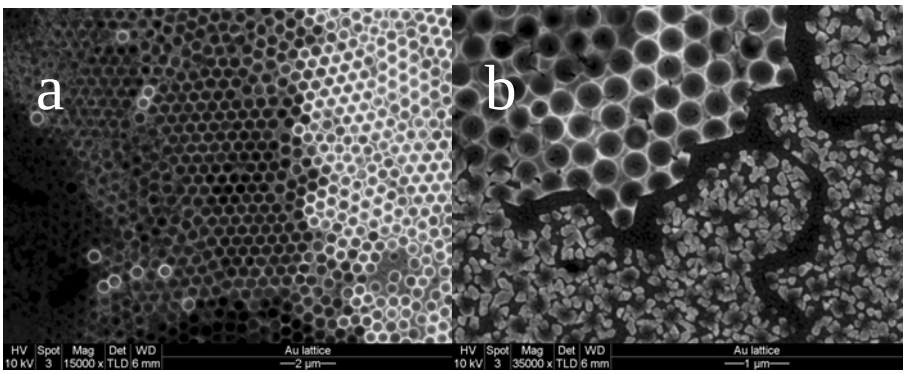

Figure 3.16: SEM micrograph of three layers of metal foam (a) and lowest layer of metal foam with substrate clearly visible (b).

Template electroless plating

A three-step electroless plating process was implemented as an alternative to electroplating, chiefly to mitigate issues involving the requirement that the nanosphere template has to be attached to a conducting substrate. For this process, three steps were carried out: sensitization, activation and plating. During sensitization, the template is immersed in $SnCl_2$/HCl for the adsorption of Sn^{2+} ions onto the template surface. The template is then washed and in the activation step, the template is immersed in $PdCl_2$/HCl to facilitate the redox reaction $Sn^{2+} + Pd^{2+} \rightarrow Sn^{4+} + Pd^0$. Palladium acts as a catalyst for the final step of the reaction where electroless deposition actually occurs.

The general form for metal ion electroless deposition is $M^{z+} + R^{n-} \rightarrow M^0 + R^{z-n}$. In our case, we have used only Ni for electroless plating. In addition to an ion source and a reducing agent, the electroless plating typically contains a complexing agent that acts as a buffer by reducing the concentration of free metal ions and a stabilizer that prevents the decomposition of the plating solution[7].

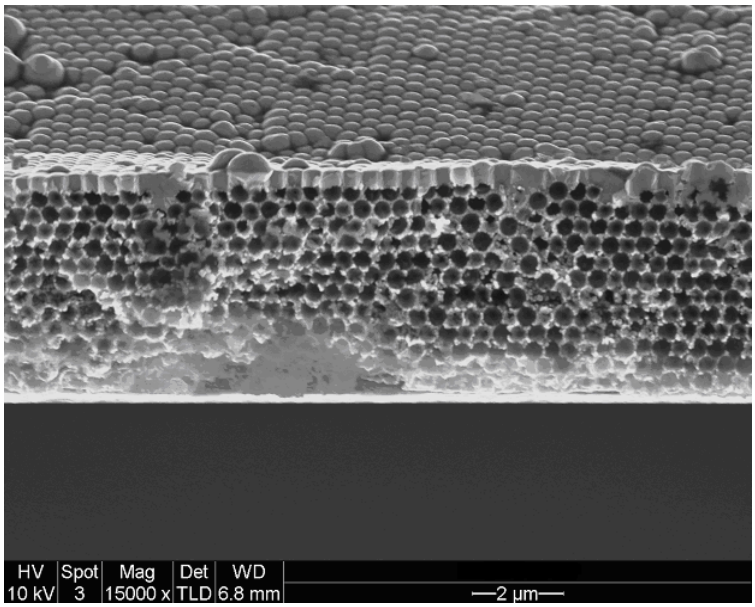

Figure 3.17: SEM micrograph of electroless plated nanosphere template on gold-plated silicon wafer after template removal.

While electroless plating of nanosphere templates did yield a high-quality inverse nanosphere foam, as can be seen in Figure 3.17, it was observed that there were significant limitations to the process. The issue of template thickness observed still remained: if the nanosphere template was deposited on a gold-plated silicon wafer, then, as shown in Figure 3.17, there was often an implied maximum thickness associated with such a template. Whilst the nanosphere template deposited on silicon was considered the ideal environment for such self-assembly, imperfections in the plating process were observed.

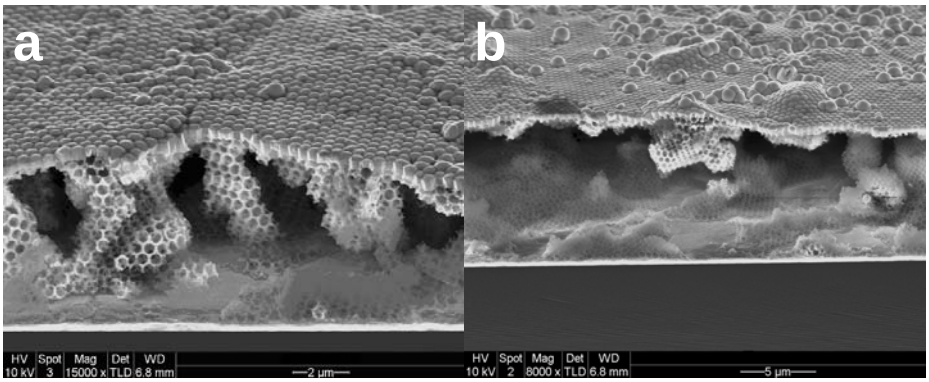

Figure 3.18: SEM micrograph of electroless plated nanosphere template on gold-plated silicon wafer after template removal with voids present.

It is evident that there were regions within the template where plating did not occur such that when the template was removed, total voids were present instead of a foam, shown in Figure 3.18. It is impossible to predict prior to experiment completion whether a particular region in a given sample would have successful plating or a void.

An alternative to the use of a nanosphere template assembled on and adherent to a gold-plated silicon wafer was to use a free-standing template. As mentioned above, it was possible to make free-standing templates by assembling them on a glass slide (optionally with a gold foil stretched over it). Templates assembled in such a way tended to delaminate. Such a free-standing template could additionally be heat-treated for strengthening. In other words, there was a larger variety of template thicknesses available for electroless plating when using free-standing templates.

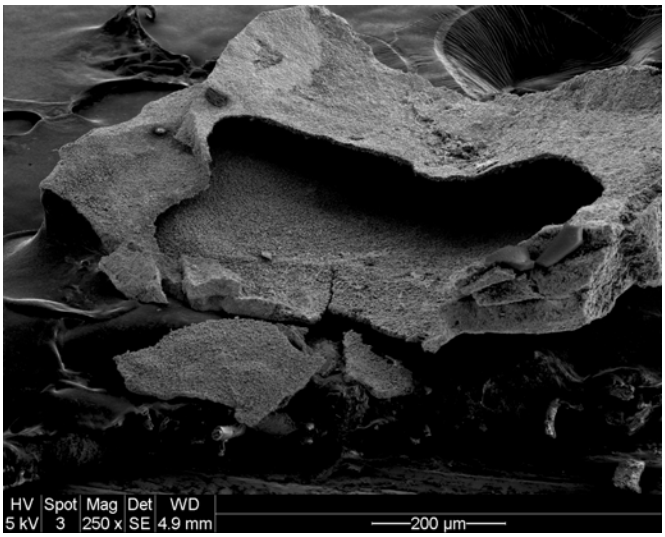

Figure 3.19: SEM micrograph of cross-section of electroless nickel-plated PMMA template after template removal.

Issues involving plating failure were only exacerbated in the case of thicker templates. In many cases, plating only occurred at the surface of the template where a continuous nickel film formed, and a few layers of nanospheres beneath the surface underwent plating, as can be seen in Figures 3.19 and 3.20. No plating occurred deeper towards the centre of the template, such that after template removal a hollow nickel shell remains with a continuous outer film and a thin foamy layer.

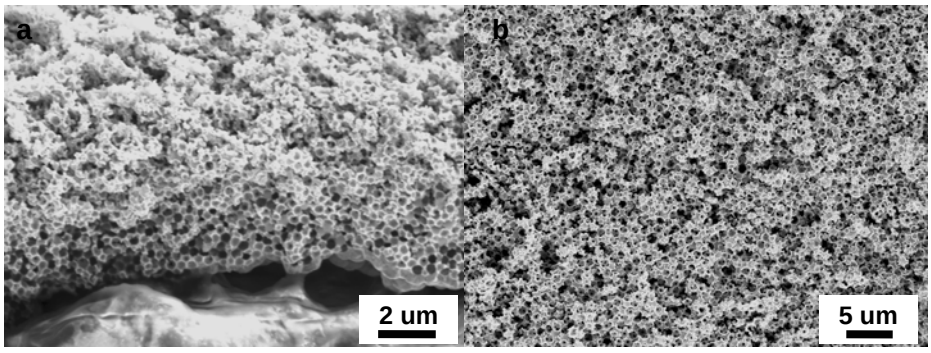

Figure 3.20: SEM micrograph of thin foamed layer underneath the continuous nickel surface film.

Processing and manufacturing

Extensive void formation was observed even in thinner free-standing templates that underwent electroless nickel plating. This tendency was attributed to the wetting properties of polystyrene and PMMA – the plating solution would not fully penetrate all pores, which would lead to incomplete plating. As mentioned earlier, surface treatment of polymer nanospheres proved to be too challenging with the equipment available. As an alternative, silica nanospheres – with superior wetting properties to those of PS and PMMA - were employed.

While plating of silica nanosphere templates could be performed using the same solutions as used for polymer nanospheres, silica nanosphere templates could only be removed through the use of hydrofluoric acid (HF) or buffered HF (BHF). Silica nanospheres did indeed demonstrate superior plating solution penetration and resultant plating, but the HF treatment required would be a severe hindrance to their use, as discussed in the next section.

Template removal

Chloroform or toluene treatments have been successfully used to remove a PS or PMMA nanosphere template completely. Typically, a full overnight immersion without agitation has proved to be sufficient. As can be seen from the Figures shown above, no evidence of polymer template remains after such a treatment.

The use of a silica template and the accompanying BHF treatment, however, has demonstrated a number of issues.

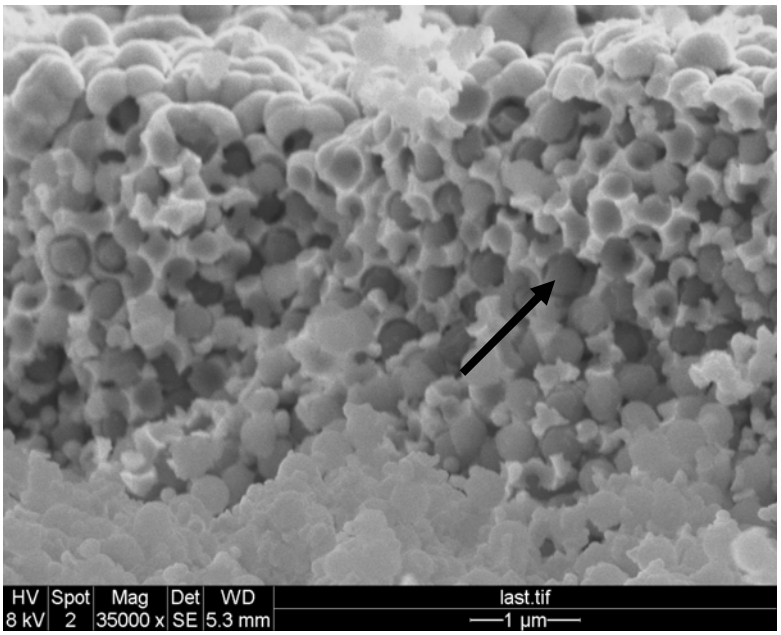

Figure 3.21: SEM micrograph of cross-section of electroless nickel plated silica nanosphere template after 45 minutes' immersion in BHF. Template still remains and is clearly visible.

The first observation was that silica nanospheres are far less susceptible to dissolution in BHF than polymer ones are in toluene or chloroform. As a result, while a quick 1-2 hour immersion could remove the majority of a polymer template, this was not an option for a silica template, as demonstrated by Figure 3.21. Instead, an overnight immersion was mandatory. This requirement raised another issue caused by material selection itself.

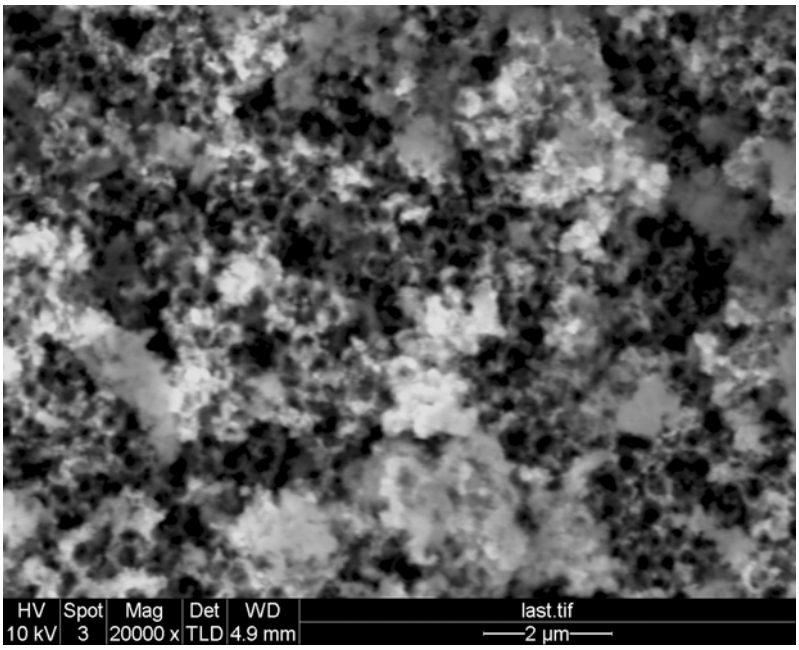

Figure 3.22: SEM micrograph of cross-section of electroless nickel plated silica nanosphere template after overnight immersion in BHF.

Over the time period it would require to remove the silica template to a satisfactory degree, the BHF would attack the deposited nickel as well, damaging the template's ordering and inducing coarsening, seen in Figure 3.22. It was not possible to mitigate the issues raised by the use of a silica template in the framework of the project.

Discussion

Three-dimensionally ordered template production by means of nanosphere self-assembly is a proven and reliable method, but quickly faces issues when the requirements of the subsequent actuation experiments are imposed. Specifically, by necessity, the end result metallic foam needs to be able to undergo a degree of deformation as part of the investigation into the actuation properties of ordered metallic foams.

As such, while a silicon wafer plated with gold served as an excellent substrate for the self-assembly of a nanosphere template and the subsequent electroplating procedure, it was unsuitable for use in actuation experiments due to the thickness of the silicon wafer being far greater compared to the thickness of the metal foam. In such an arrangement, any deformation in an actuation experiment would be stopped by the silicon substrate's contribution. The merits of self-assembly on a metal-plated silicon wafer still warrant discussion for the sake of analysis, however. A typical commercial silicon wafer has an extremely low surface roughness, with the best offering surface deviations no greater than 1nm. In our experiments we have used physical vapor deposition (PVD) to apply a ~10nm-thick layer of gold on the silicon wafer. We can assume a homogeneous deposition of material across the silicon wafer and thus no significant alteration to the initial surface roughness of the substrate.

As such, the prepared substrate offers surface features whose scale is negligible compared to the size of a single nanosphere. In other words, a silicon wafer with a PVD-deposited layer of gold can be considered as a perfectly smooth surface for the assembly of a nanosphere template. In this sense, such a substrate offers the most optimal conditions for template assembly, with inhomogeneities limited to the nanosphere solution and the nanospheres themselves. Indeed, it has been observed that, amongst all substrates used, only laboratory glass slides offered a similar quality of the end result template such that opalescence was observed with the naked eye across the entire deposited nanosphere layer.

Template adherence to the substrate was also highest for the silicon wafer, which corresponds to the high surface quality. For the purpose of the assembly of a free-standing template, however, this was a hindrance, as it is impossible to remove the template from the wafer without damaging the template. Use of gold-plated silica wafers as substrates for nanosphere template assembly was eventually discontinued due to the challenges presented.

While still interested in the electroplating of a nanosphere template, we proposed an alternative procedure that would, in theory, yield an effect similar to Kramer's bistrip experiment [3]. We would assemble nanospheres on a gold foil that had been stretched over a glass microscope slide. The intent was to be able to remove the foil from the glass slide with the template still attached. After electroplating and template removal the result would be a metallic bistrip, with one side a continuous solid Au foil and the other an ordered porous metallic foam.

Unfortunately, it was found that the adherence between the gold foil and the microscope slide is stronger than that between the nanosphere template and the gold foil. The reason for this effect is the simple difference between contact areas – the area between glass and Au is far greater than that between spheres and Au, leading to a far higher compound adhesive force, in this case Van Der Waals. A side effect of Au's easy adherence to glass is the formation of roughness as pockets of air lead to an uneven spread of the gold foil onto the glass.

This roughness further inhibits the deposition and adherence of nanospheres, as the size of the roughness features observed, for example in Figure 3.14, begins to approach that of the nanospheres. The final result is that in all cases a fully-assembled template would completely delaminate from the glass-Au substrate, disallowing further electroplating experiments.

This delamination could be exploited, however, with the use of electroless plating methods. As a delaminated nanosphere template was a fully free-standing template, it was open to heat treatment for strengthening and further use in the somewhat aggressive environment of the electroless plating bath. Here, however, plating was found to only form a continuous solid shell and a few nanosphere layers' worth of foam deep. This can be caused by two mechanisms.

The first involves the formation of the continuous solid outer nickel shell. Specifically, due to ease of transport, nickel deposits most easily

on the immediate surface of the nanosphere template first. As electroless plating is an autocatalytic reaction, i.e. the deposition of metal further catalyses the process, any further deposition would occur most rapidly at the surface, leading to the formation of the solid shell.

Further deposition would occur inside the shell, but would be limited due to depletion of nickel ions in the plating solution inside the shell. Ionic replenishment of the solution would be impossible due to the shell acting as a barrier. Once all ions inside the shell have been deposited, no further plating can occur. Of course, when the template is removed, the unplated region results in a large void inside the solid nickel shell. The second mechanism involves the poor wetting properties of the polymers used.

The result of this could be that the solution is simply not capable of penetrating to a particular depth within the template. As there is no driving force for the plating solution to enter the pores beyond capillary force, a balance rises where the surface tension prevents any further progress of the solution into the template. The result is, once again, that after the template is removed the large unplated core of the sample becomes a void.

When using PMMA, PS and silica nanosphere it is a common experience that the easier the sphere is to use pre-plating, the harder it will be to work with after plating and, very notably, vice versa. This comes from the mechanical and chemical stability of the nanospheres and the requirement by necessity that the template constructed from the nanospheres will need to be destroyed selectively. Of course, the more robust the nanosphere, the harder it will be to destroy the template at the end.

While theoretically offering a high-quality three-dimensionally-ordered template that is assembled with no additional input other than the initial experimental setup, it seems paradoxical that nanospheres are also the most prone to errors during assembly. A template will self-assemble

perfectly only with the consideration that every single sphere in the colloidal solution matches every other one. A small degree of polydispersity may be accommodated by the lattice such that any disorder it induces will only extend a few unit cells, but any size variance significant enough to be observed under the SEM induces severe nanosphere lattice faults.

The presence of a single sphere larger than the ones around it is a cause of lattice distortion, and therefore the concentration of such larger spheres is directly related to the degree of ordering observed within the template. In this context, we consider a template strongly ordered when a single nanosphere grain extends many hundreds of nanosphere diameters in every direction. A weakly ordered template, then, only has grains the size of several dozen nanosphere diameters.

The strengthening of templates by heat treatment operates on the same principle as the commonly-observed neck formation between ceramic or metallic particles during sintering as shown in Figure 3.23. Instead of full sintering, the heat treatment would be stopped at the earliest point of neck formation such that the weak Van Der Waals adhesion bonds between particles would be replaced by the far stronger covalent bonds or chain entanglement depending on the material of the particles. While silica offered the most forgiving treatment conditions (overnight at 900°C) where the only requirement was that diffusion was enabled between adjacent particles, details became increasingly important in work with polymer nanospheres.

It was observed that treatment should be held at temperatures that just allow the sliding of polymer chains without approaching the glass transition temperature. At this stage, chain drift is still extremely quick, and full coarsening of adjacent spheres can occur within minutes.

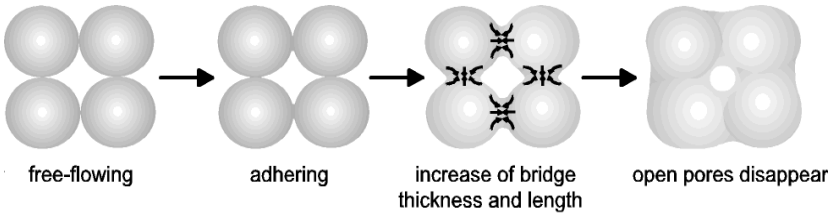

Figure 3.23: Stages of sintering of spherical particles [10].

Centrifuge-assisted template assembly did allow for extremely quick assembly of nanosphere templates, but was only limited to silica nanospheres due to the high heat induced during centrifugation that would easily lead to polymer nanosphere damage and coarsening. In this process, nanospheres are forced by centrifugal force to the bottom of their container, vastly accelerating template assembly time. Self-assembly is very substrate-dependant, and the quality of the first layer of nanospheres formed will significantly affect every other layer above it – it is for this reason that the extremely flat silicon wafer offered the best possible surface for template assembly.

For this same reason centrifuge-assisted assembly is an extremely poor environment for the formation of long-ranged order within a template due to the nature of the apparatus available. Specifically, only round- or cone-shaped-bottomed containers could be used in the centrifuge, and therefore, due to the inhomogeneous surface available for self-assembly, there is a significant limit on the ordering possible. The speed of the process still makes it viable for experimentation where long-range ordering is not of the utmost importance – the ability to assemble a template within 30 minutes as opposed to 5 days is not to be ignored.

3.4 Gyroid inverse templating.

Methods associated with the use of diblock copolymers.

The production of diblock copolymer templates was carried out by Dr. Ivana Vukovic, and a full discussion on their fabrication and the nature of their microstructure at varying compositions is available in her thesis [7].

Experimental procedures

Diblock copolymer templates were removed by overnight immersion in toluene or chloroform. Alternatively, templates were removed by overnight heating in a furnace at 450°C overnight. Chemical removal was only used in conjunction with copper or gold plating, and heat-based removal was used in conjunction with nickel plating.

Actuation was carried out in a glass Petri dish under an optical microscope at 10x magnification. The optical microscope was attached to a camera with proprietary acquisition and recording software. A standard three-electrode setup was used where samples were placed on a gold working electrode, with Ag-AgCl as the reference and a block of nanoporous Au as the counter electrode. Actuation was carried out through repeated cyclic voltammetry sweeps in a triangular wave pattern in the range 0-0.5V.

A dual beam FIB/scanning electron microscope (SEM) microscope (Lyra, Tescan, CZ) setup was used for selective milling of nanoporous foam sample surfaces. Sample orientation was controlled through both FIB stage manipulation and through physical sample reorientation by means of a modular custom stage. Milling was carried out at a variety of preset ion currents: 1, 10, 40, 150, 200, 1000 and 10000nA.

A Hysitron picoindenter was used in conjunction with a JEOL 2010 Transmission Electron Microscope. The picoindenter employs a custom

stage that allows samples that have been processed in the FIB using our own modular stage to be transferred without the sample itself having to be detached from its stage at any point. Pillars were deformed using the 1µm-diameter indentation tip. Indentation was carried out until fracture or, if no fracture was observed over one cycle, repeated loading was performed until fracture occurred.

Results

Unlike their counterparts in nanoporous gold, ligaments in nanoporous nickel were not observed to easily coarsen during exposure to heat. This allowed for the use of pyrolysis for the removal of the gyroid template. As pyrolysis does not rely on the ability of a solvent to penetrate the pore structure of the template but merely on the capacity of the sample to fully conduct heat, it is a much more reliable technique for template extraction than wet methods.

Figure 3.24: SEM micrograph of nickel cross-section after 400^{o}C furnace treatment for 1 hour.

The earliest implementations of this treatment have demonstrated excellent retention of ligament structure, seen in Figure 3.24 as well as the reliable removal of the template – energy-dispersive spectroscopy (EDS) consistently showed only trace carbon after pyrolysis, with carbon being the characteristic signature peak present in the polymer templates used.

A main concern with every template removal method is whether it is successful in penetrating to the deepest points at the centre of a sample. Chloroform treatments have shown a tendency where only surface layers of the template would be removed, with the template remaining intact deeper inside. As consistently seen in Figure 3.24 and in all other furnace-treated samples, cross-sections through any part of the material where gyroids have formed always show clear porosity and thus complete template removal.

It has also been generally observed that furnace-treated sample undergo significant cracking – a typical sample will often break apart into smaller sections during handling and SEM micrograph frequently show large discontinuities between porous sections, seen in Figure 3.25.

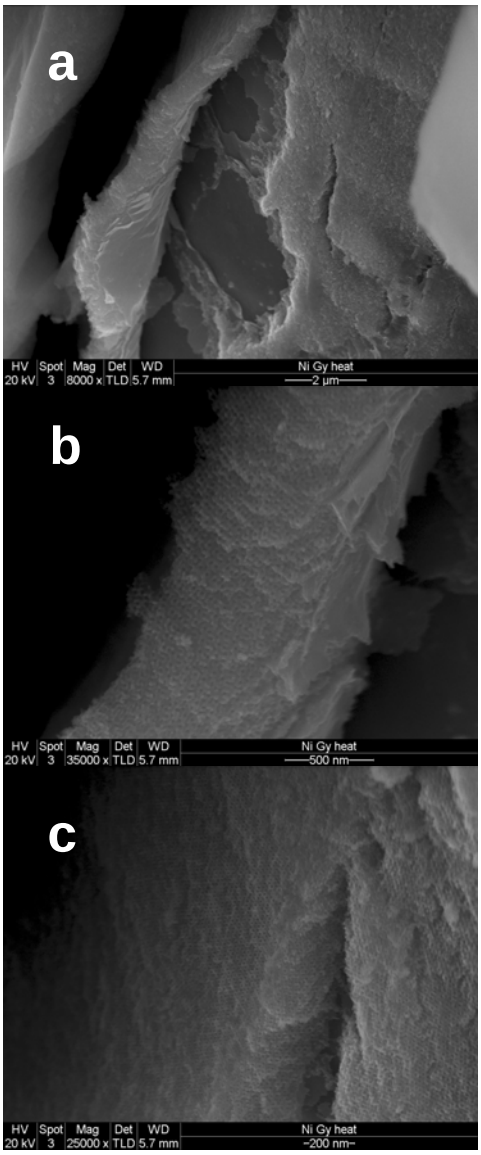

Figure 3.25: SEM micrograph of various cross-sections of a furnace-treated nickel sample. (a) and (b) show the same region at different magnifications where a fully porous layer has detached from a solid substrate. (c) shows clear porosity within a crack.

The extent of the nanoporous nickel foam's capacity to resist adverse effects brought on by heat treatment was implemented. Samples were furnace-treated at temperatures standard to pyrolysis treatment,

approximately 350-450°C, but for extensive periods of time: between 1 and 4 days' continuous treatment.

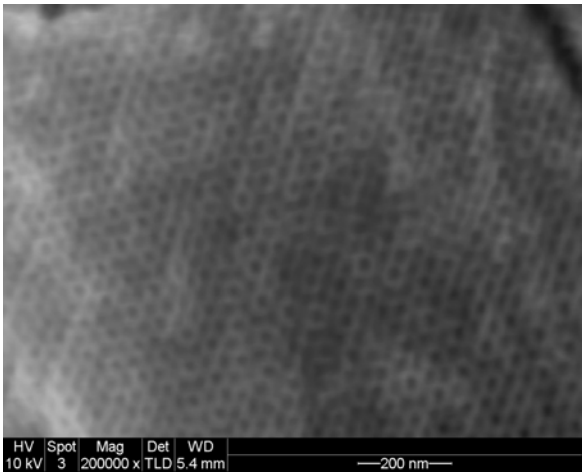

Figure 3.26: SEM micrograph of nanoporous nickel foam treated for 1 hour. Used as a reference for ligament size.

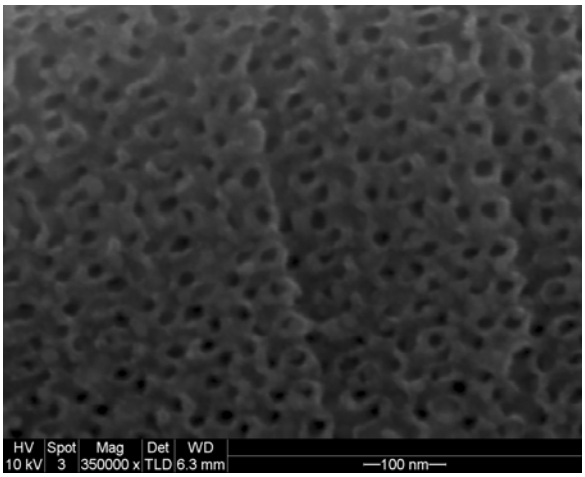

Figure 3.27: SEM micrograph of the same nickel foam as in Figure 3.26, treated for 1 day.

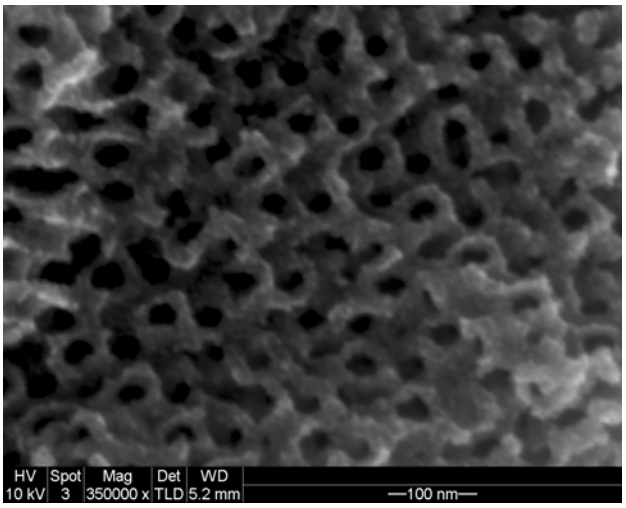

Figure 3.28: SEM micrograph of the same nickel foam as in Figure 3.26, treated for 4 days.

As can be seen across Figures 3.26-3.28, even by the 4th day of continuous heating, only extremely minor distortion can observed in the foam – ligaments have coarsened slightly and pores have increased in diameter accordingly. It is clear, however, that pores still remain open and ordering is still preserved.

3.5 Actuation

The actuation setup that was used in this investigation aimed to replicate the experiments initially carried out by Kramer *et al*. and others in the field. For this purpose, a common three-electrode cell setup with an electronic potentiostat was used to ensure that electron injection was as controlled a process as possible. Cyclic voltammetry of solid nickel provided a characteristic peak pattern that we were able to use to determine the optimal operating conditions for actuation. This typical peak pattern can be seen in Figure 3.29, assembled by performing repeated sweeps. During our experiments we have used Au connecting wires for working and counter electrodes. Previous

experiments with Au have shown a stable region between 0 and 0.5V where no redox reactions occur but, rather, weak space charge effects take place. Therefore, we have used this range of values to prevent the Au connectors from influencing the results from Ni.

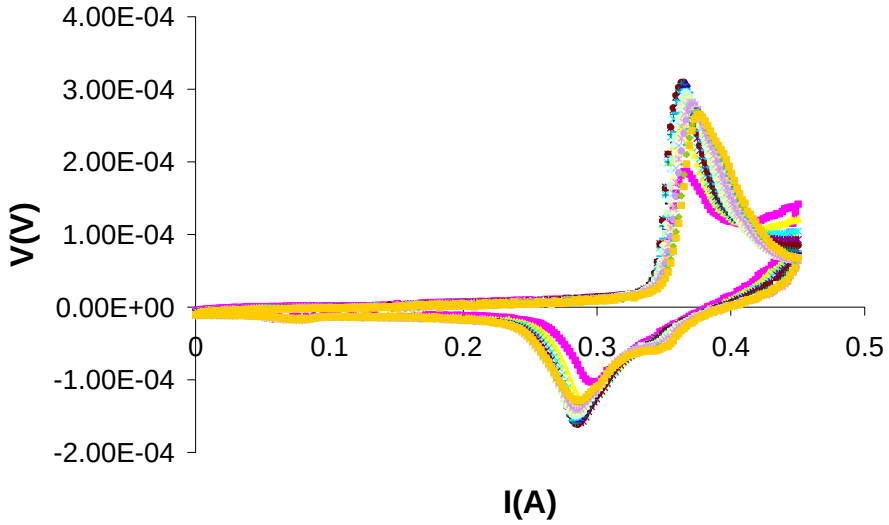

Figure 3.29: Cyclic voltammetry of solid bulk nickel sheet over 20 sweeps. Each color represents a separate sweep.

The 0-0.5V region showed characteristic peak behaviour for solid nickel. While it has been observed in Au that the most stable actuation results came from the space charge effect range with redox regions introducing uncertainties, the space charge range in Au is much greater than that in Ni, allowing for greater charge injection into the sample. Therefore, the entire 0-0.5V range was used in all electrochemical experiments involving nickel.

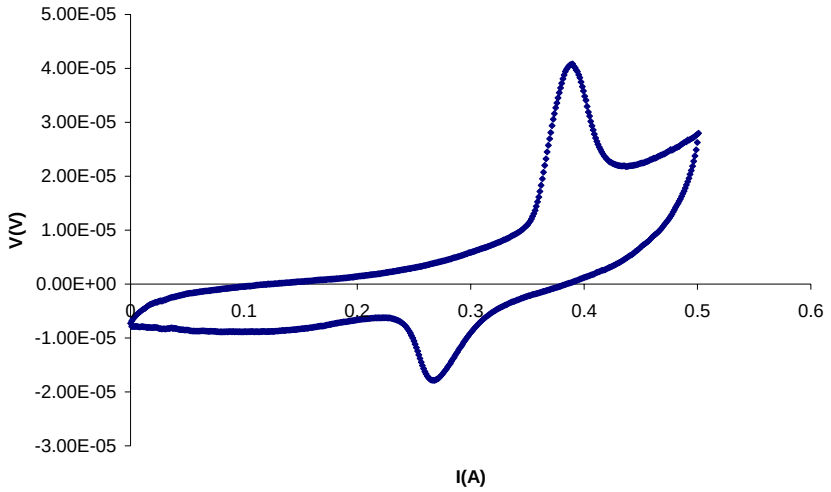

Figure 3.30: Cyclic voltammetry sweep of nanoporous nickel foam.

As a rule, the response observed from nanoporous nickel foam, shown in Figure 3.30, was much weaker than that of the solid variant, although the shape of the sweep remained the same. As charging and discharging in a controllable manner could be observed across most nanoporous nickel samples, actuation testing proper was carried out. This was performed by means of observing a selected sample in a cyclic voltammetry setup using an optical microscope.

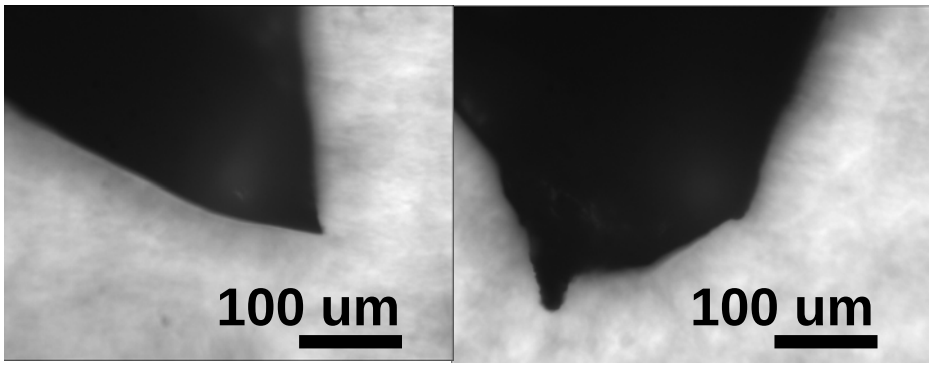

Figure 3.31: Optical micrograph of section of gyroidal nanoporous nickel sample.

In all cases, observation was carried out across the up- and down-sweeps separately. An up-sweep is defined as the full potential progression from 0 to 0.5V and a down sweep progresses from 0.5 back down to 0V. By studying individual sweeps, we hoped to identify deformation tendencies characteristic to an increase or reduction of charge at the sample. However, if any deformation occurred, it was not visible using the apparatus we had available. No deformation was observed in actuation experiments using gyroidal nanoporous nickel.

3.6 Focused Ion Beam

With large-scale nanoporous nickel samples presenting mediocre at best results in actuation and utility, we attempted to reduce the working scale so as to improve sample reliability and, potentially, strength of results. Our primary tool for this was the Focused Ion Beam (FIB) that, in principle, would allow us to select and isolate individual areas with gyroid microstructure, Figure 3.32 showing an early attempt.

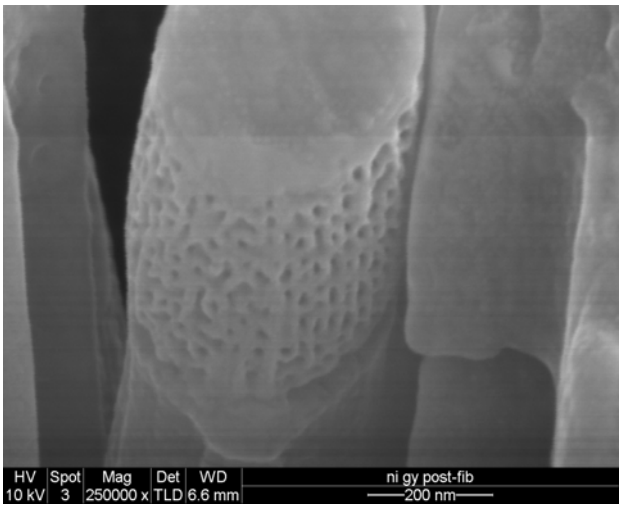

Figure 3.32: SEM micrograph of FIB-milled gyroidal nickel.

A primary concern during ion beam milling is the damage done to the sample. By necessity, a large amount of energy is imparted into the target due to ion impacts. This effect has the potential to cause smearing, coarsening or filling of voids of a nanoporous structure. In experiments with nickel, it was observed that the nanoporous microstructure did not suffer significant damage beyond light surface smearing. However, the degree of control over the quality of the FIB-isolated region was limited.

This is due to the FIB orientation – initial experiments set the FIB to mill perpendicular to the sample surface such that the topmost layer was the continuous solid nickel layer above the porous region. Considering the voids that were present in the porous regions, as discussed earlier, it was impossible to predict whether a target region would have foam or void. As such, a different orientation was selected to improve controllability.

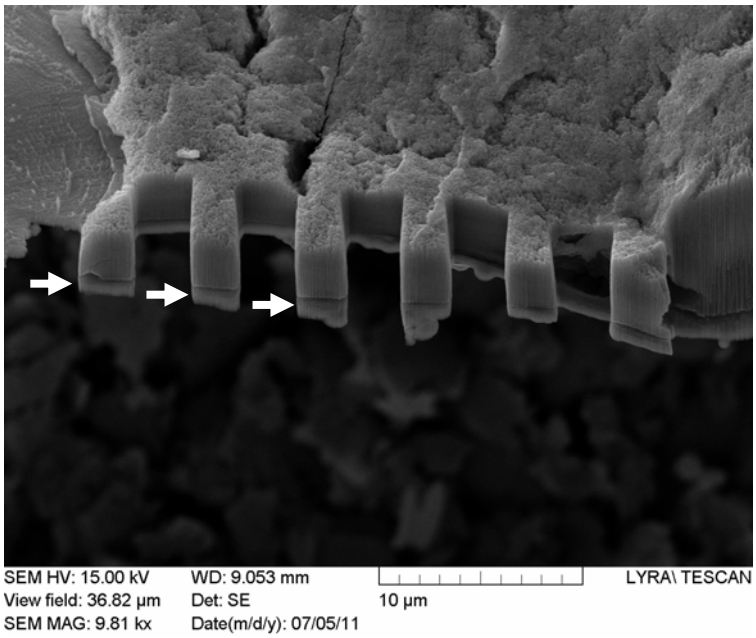

Figure 3.33: SEM micrograph of gyroidal nickel sample edge. Continuous solid nickel layer is visible.

As shown in Figure 3.33, by orienting the ion beam to face the edge of the sample, it was possible to expose and select full gyroidal regions with much greater reliability. With the degree of control that the FIB offers, it was, in fact, possible to mill away the continuous solid nickel layer, leaving only teeth of gyroidal nickel. These could then be milled into even more controllable structures.

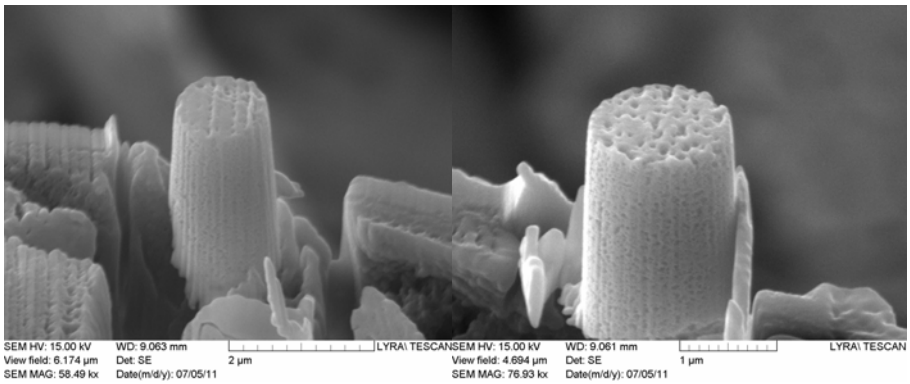

Figure 3.34: SEM micrograph of cylindrical pillars of gyroidal nickel.

The ability to mill gyroidal nickel into cylindrical pillars of a variety of dimensions was demonstrated (Figure 3.34). Pillars were mechanically stable, not suffering any noticeable alterations or effects when stored in normal atmosphere conditions at room temperature. Diameter control was very high, such that pillars with submicron diameter could be produced. However, below ~150nm pillars began to suffer from smearing much more severely and it was not feasible to produce pillars fit for experimentation at that point.

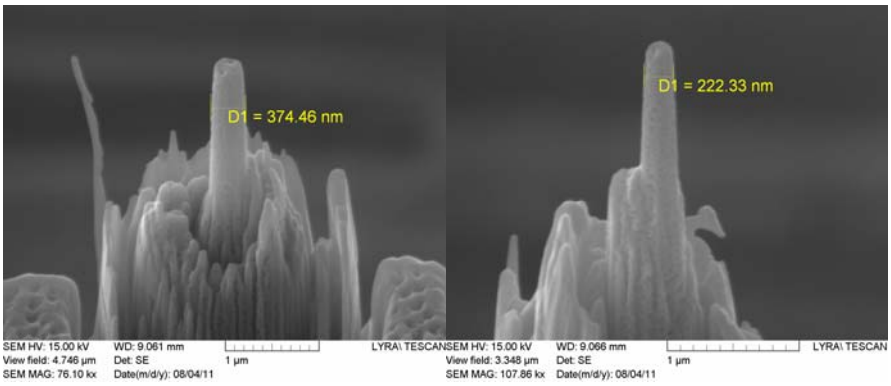

Figure 3.35: SEM micrograph of cylindrical pillars of gyroidal nickel.

Due to the orientation of the ion beam and the peculiarities of the ion beam emission, a taper angle developed in the pillars in all experiments, such that the pillar's diameter was greater at its base than its tip, seen in Figure 3.35. This would play a highly important role in experiments discussed later. Despite the increased sample reliability that ion milling offered, it was not possible to evaluate the actuation properties of the features milled due to the extremely low length scales involved. As it was impossible to perform electrochemical experiments *in-situ* in an SEM or AFM, actuation experiments were discontinued.

3.7 Picoindentation

The use of the FIB to fabricate pillars with a controlled shape and known microstructure opened the possibility for the mechanical characterization of the material through the use of specialized picoindentation equipment.

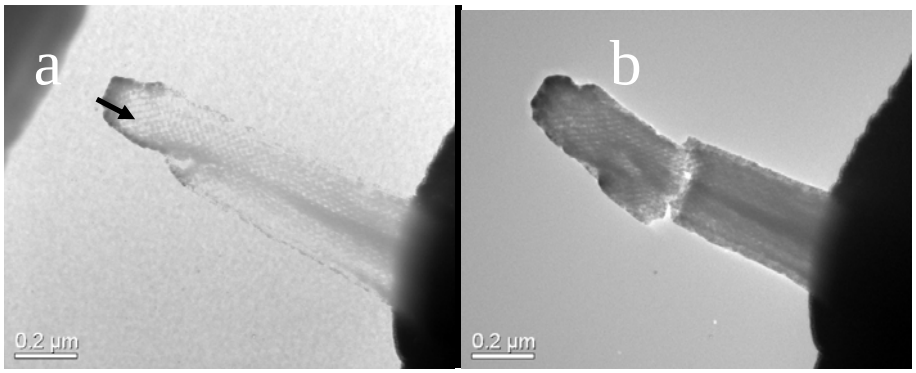

Figure 3.36: TEM micrograph of gyroidal nickel pillar (a) and subsequent fracture after indentation (b). Indentation direction is indicated.

As mentioned previously, a major issue regarding the indentation of freestanding pillars as shown in Figure 3.36 is the tapering due to the orientation of the ion beam. To combat this, a new procedure was implemented to mill pillars in such a way as to prevent tapering.

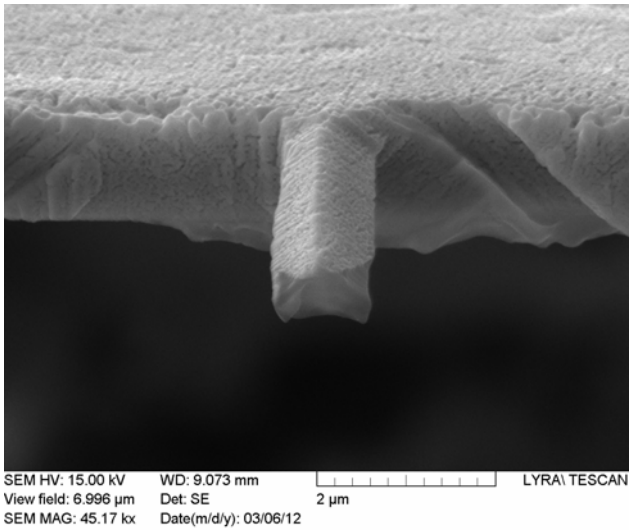

Figure 3.37: SEM micrograph of non-tapered nanoporous metal pillar.

The use of non-tapered pillars (Figure 3.37) prevents localization effects due to variation in diameter across the compression axis.

Indentation experiments were carried out on the freestanding non-tapered nanoporous metal pillars. Pillars were produced from both disordered nanoporous Au as well as ordered nanoporous Ni. Pillars produced in such a manner fully retained their porosity, as well as quality of ordering, as shown in Figure 3.38.

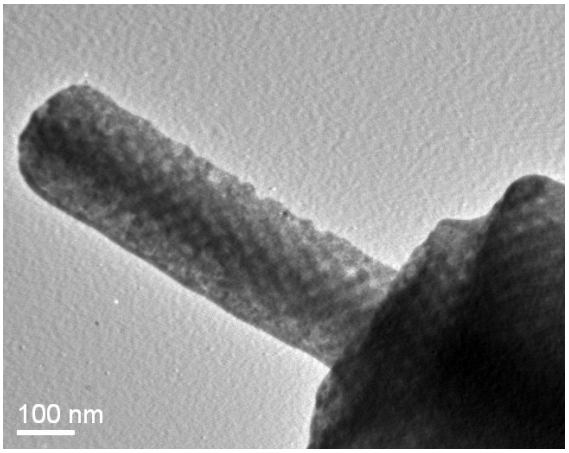

Figure 3.38: TEM micrograph of non-tapered gyroidal nickel pillar.

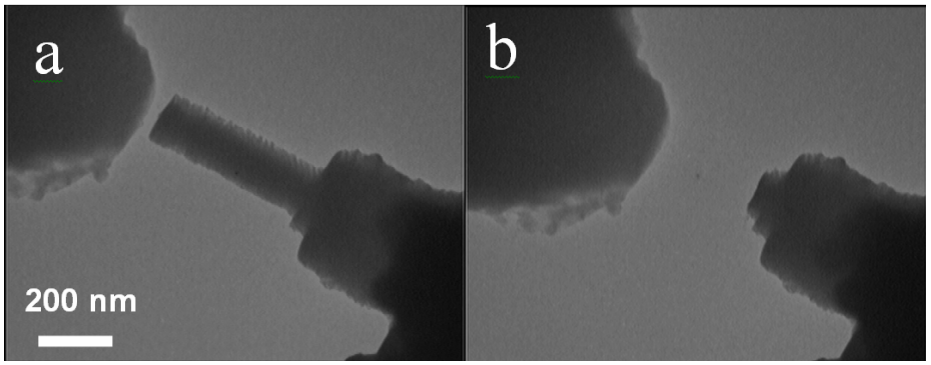

Figure 3.39: TEM micrograph of gyroidal nickel pillar before (a) and after (b) indentation. Brittle fracture observed.

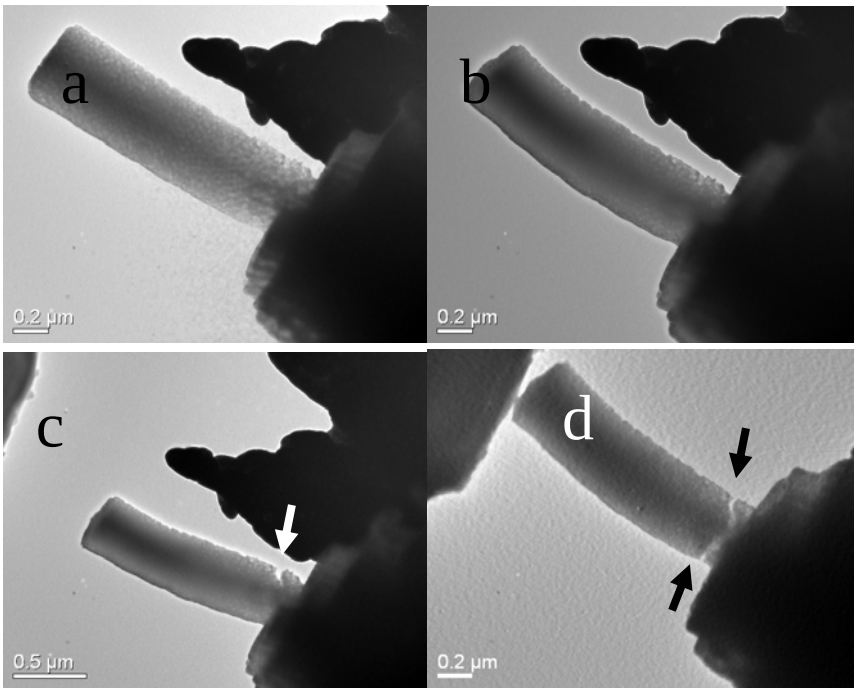

Figure 3.40: TEM micrograph of initial pillar (a), during loading (b), after loading with recovery and after subsequent loads (d). Minor fracture after initial load is visible, and the expansion thereof after subsequent loading.

Two modes of deformation were observed during indentation: brittle fracture (Figure 3.49) and ductile deformation with limited recovery (Figure 3.40). In the former, the pillar would spontaneously fracture at a particular load without developing any significant deformation prior.

In the latter, the pillar would be observed to undergo a gradual bend without fracture until load release, where the pillar would partially regain its original shape. Full recovery was not observed due to the development of minor fracture regions during initial loading. Subsequent loads on the same pillar after recovery would increase the size of the fracture, leading to stress localization in subsequent loads and eventual spontaneous fracture nucleating from the affected area.

It was observed that the tendency towards gradual deformation over spontaneous fracture was dependent on pillar diameter such that thinner pillars would deform gradually. Typically, pillars under 300-400nm diameter would be thin enough for such behaviour, and thicker pillars would be more likely to undergo spontaneous fracture.

It is worth emphasizing that in all indentation experiments where gradual deformation was the mode of deformation the nature of deformation was a bending, as opposed to a pure compression as would be expected from an indentation test. This tendency made for challenging prediction on the true behaviour of nanoporous pillars under compression, as bending adds additional deformation components to the otherwise simple cell wall buckling model of the effects of the compression of porous media.

This bending stemmed from the specific design of the Hysitron Picoindenter, where the indentation tip is aligned such that, if a sample is sufficiently small, there is only a very specific set of sample positions and orientations that would allow for pure compression.

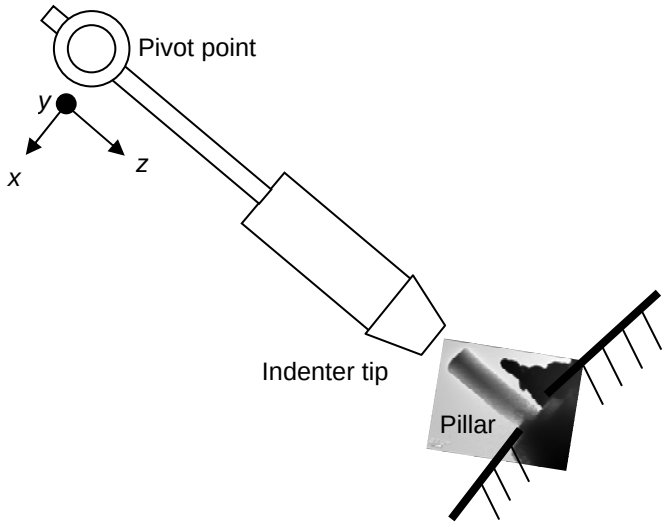

Figure 3.41: Schematic illustration of Hysitron Picoindenter indentation mechanism.

Processing and manufacturing

As is shown in Figure 3.41, instead of sitting on a translation axis that would allow free movement along a 3-dimensional Cartesian axis, the indenter tip is connected at its base to a pivot mechanism that has 2-dimensional translation capacity only in the *y* and *z* directions. Reorientation in the *x* direction is, instead, handled by a rotation along the pivot point. The result is that perfect pure compression is only possible when the pillar is perfectly aligned with the indenter tip, which itself is at its x-axis 0 point.

Discussion

Diblock copolymer templates offer an excellent and stable platform for the production of ordered metallic foams by means of inverse templating. In their initial state, they are strong and flexible, allowing them to be handled and used in more agitated conditions than nanosphere templates. The surface treatment that occurs during the production of these templates mitigates the severe wetting problem that nanosphere templates experience during metal deposition – the wetting properties of di- and triblock copolymers used for templating are far superior to the nanosphere templates' [7]. Finally, by virtue of being composed of non-cross-linked organic polymers the block copolymer templates decompose easily at elevated temperatures or in the presence of organic solvents.

All in all, block copolymer templates, at least in theory, offer a superior templating platform than polymer or silica nanospheres. In practice, however, some major issues are still present that limit the utility of resultant metal foams. The first of these are the dimensions and shape of the gyroid unit cell that provide channels of approximately 30-50 nanometres. Whilst this is excellent for a comparison to disordered nanoporous Au produced by dealloying, the reality of the issue is that a plating solution needs to first penetrate the extremely complex channel arrangements in a gyroidal block copolymer template before such a comparison can be made. We have repeatedly observed the failure of full penetration of a plating solution to a satisfactory depth within a

template, which, in a remarkably similar process to that of nanosphere templating leads to the presence of large voids within an end-product nanoporous metal.

Even the smallest degree of non-penetration will lead to discontinuity in a foam, leading to stress concentration during light handling and, subsequently, cracking. This cracking will occur even outside of handling: previous work on nanoporous Au produced by dealloying showed that the Au lattice would undergo significant shrinkage during the removal of the Ag component [11].

We can expect this lattice relaxation to occur as well in a metal-polymer composite during the removal of the polymer. While in a perfect, defect-free lattice the stress during this process should be fully hydrostatic, any discontinuities by means of voids will lead to localization events. The presence of cracks and voids severely weakens the ability of the metal foam to actuate. This comes as a result of the voids being able to "absorb" deformation, as is illustrated in Figure 3.42.

The nature of the deformation during the actuation of porous metals is a full expansion or contraction depending on the nature of the charge injected into the metal. Where a perfect, void-free foam will experience a single expansion/contraction event, a foam with multiple voids will, in effect, experience a multitude of such events, each one on a much smaller scale.

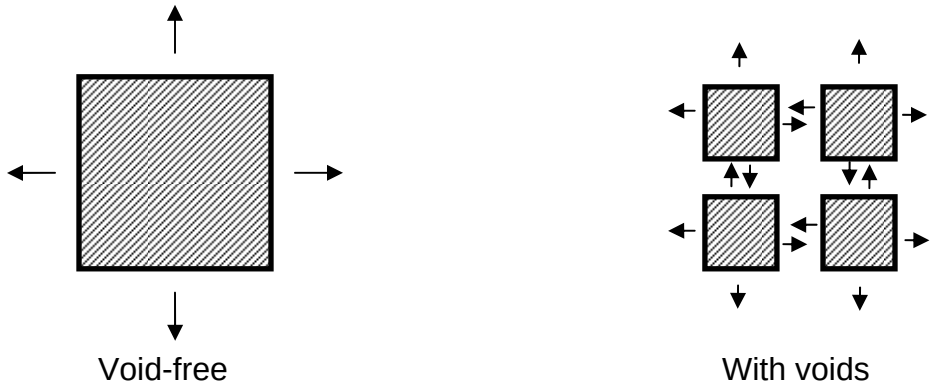

Figure 3.42: Schematic illustration of effects of voids on nanoporous foam deformation during actuation.

The second issue follows from the consideration of the use of ordered nanoporous foams to achieve an anisotropic response during actuation. To restate, it was proposed that an ordered foam would have preferential deformation orientations, such that deformation during actuation would be enhanced in a particular set of directions compared to the isotropic deformation observed in a disordered metallic foam.

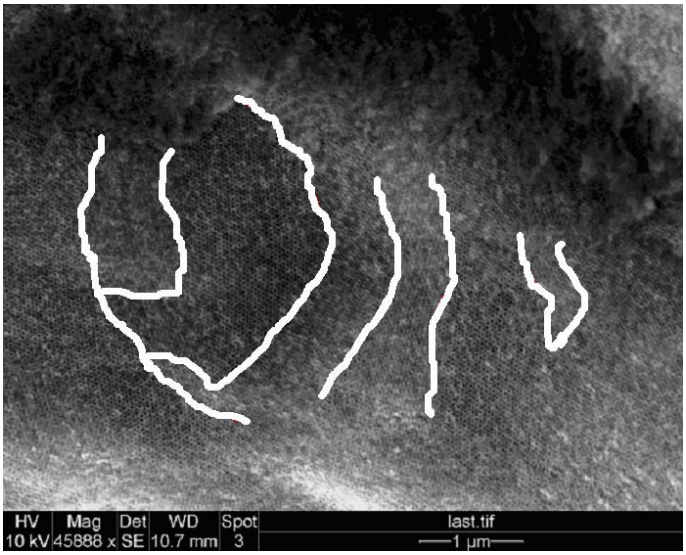

Figure 3.43: SEM micrograph of multigranular structure of a gyroidal nickel foam. Grains separated in white.

As can be seen in Figure 3.43, the typical diblock copolymer template forms through multiple nucleation events which lead to the formation of a granular structure. By necessity, such a granular microstructure is passed on to the templated metal foam. In our experiments, we have never observed the formation of a truly single-crystalline template or product foam. It is clear that no anisotropic response can be achieved with a highly multigranular microstructure as seen in the Figure, as any enhancement of deformation along a preferential orientation would be limited to a single oriented grain.

Over a sufficiently large number of grains, the full foam's response would approximate to an isotropic one. A variety of metals are available that are compatible with the electroless plating technique: gold, copper and nickel. Of these, nickel has been demonstrated to be superior for its excellent shape and porosity retention during heating in Figures 3.25-3.28.

As mentioned earlier, we have repeatedly observed that pyrolysis is the most reliable method for template removal, hence our preference to use this technique over chemical methods involving soaking in toluene or chloroform. We attribute nickel's stability to the quick formation of a protective oxide layer. It bears mentioning that this oxide layer should not affect the actuation properties of the material, as an oxide layer observed on Au in previous experiments [11] and no meaningful change was observed in Au's actuation behaviour. We can be sure that, in the case of nickel, the oxide is only a surface layer, with the majority of the material remaining unoxidised, as the electrochemical response during cyclic voltammetry and subsequent actuation shows a characteristic metallic nickel response.

The FIB offered a very powerful and versatile technique for the selective shaping of gyroidal nickel. As mentioned above, the polycrystallinity of the gyroid grains severely limited the possibility of an enhanced anisotropic response. By milling out a feature out of a single grain we can force a single-crystalline structure. Indeed, gyroidal

grains have been observed to be between 500nm and up to 5μm in diameter, so if a grain is well-selected, then a fully monocrystalline feature can be produced. This is demonstrated in Figure 3.38.

The tapering induced by ion milling stems from the way the apparatus itself is arranged. Specifically, ions are emitted from a point source and pass through a series of lenses, much akin to an electron beam. However, at the smallest scales, imperfections in beam alignment lead to a gradual divergence of the electron beam as it travels away from the source, leading to the tapering effect.

While it is possible to produce pillars with diameter under 150nm, at such scales the ion beam does not have guaranteed stability. Minor drift or dwell time discrepancies begin to have a greater influence such that porosity is damaged and, in the worst case, the pillar can be destroyed.

The procedure to produce non-tapered pillars as is described before mitigates the problems with ion beam stability somewhat. As the side-milling procedure allows for very gradual successive sweeps with highly-controlled ion exposure areas, smaller pillars became feasible. However, it was still impractical to go under 150nm due to mechanical stability issues: considering that pore size is around 30-50nm, pillars at such dimensions would be only 3-5 unit cells in diameter, and extremely fragile during handling. In addition, a peculiar deformation phenomenon prevented the fabrication of straight pillars under this diameter. This phenomenon will be discussed in detail in further chapters.

The most interesting results were observed in indentation experiments that led to gradual deformation with light recovery. Where cell wall buckling would be a dominant mechanism in pillars with large diameters, in pillars with small diameters surface effects become much more influential.

In the latter case, the free volume present due to the porosity of the material offers a large degree of freedom for deformation, where shifting ligaments are unconstrained by surrounding material. This behaviour has been predicted and observed by Volkert and Biener [12,13]. Unfortunately, due to the alignment problems that our picoindentation apparatus experienced, we were unable to examine this phenomenon further using classical methods.

3.8 Transition into Ion-Beam-Induced Bending

As mentioned in the previous section, a peculiar deformation phenomenon was observed when using the FIB to fabricate porous pillars with diameter under 150nm. Specifically, after milling, pillars were observed to be bent without fracture, but, rather, as a single, continuous bend. Initially this effect considered as a hindrance to experimentation, as pre-bent pillars would obviously continue bending in the already difficult-to-control picoindentation equipment as opposed to responding with pure compression deformation. However, this effect was observed to be consistent and reproducible, not only in pillars, but also in free-standing nanoporous Au sheet, as shown in Figure 3.44.

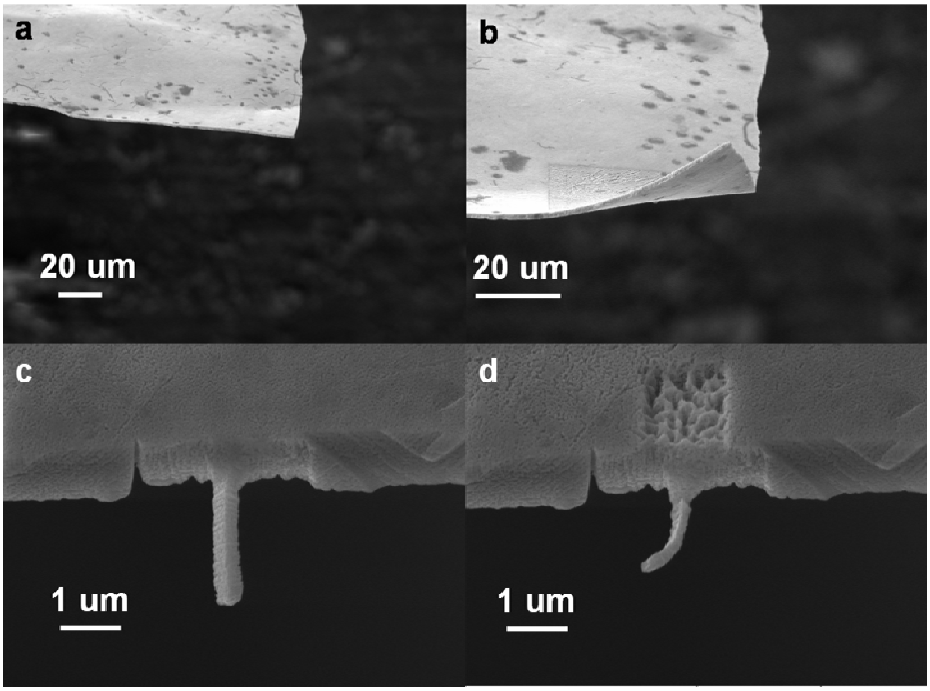

Figure 3.44: SEM micrographs of nanoporous Au foil before (a) and after (b) continuous ion beam exposure and of nanoporous Au pillar before (a) and after (b) repeated ion milling.

Further experiments demonstrated that this effect only occurred during exposure to an ion beam, never when similar exposure occurred under an electron beam, as shown in Figure 3.45.

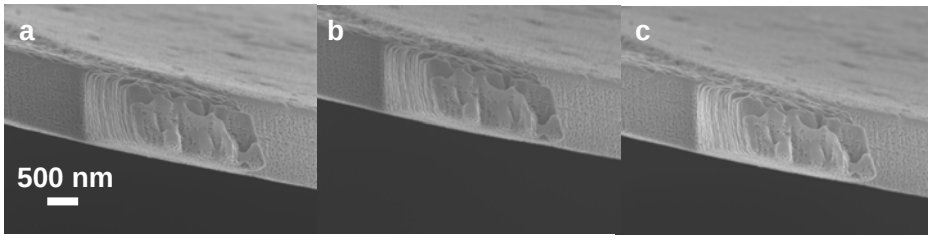

Figure 3.45: SEM micrograph of nanoporous Au feature before (a), during (b) and after (c) a 10-minute electron beam exposure at 30kV. No deformation was observed.

Furthermore, the lack of recovery of the deformed areas suggested that this was a deformation induced by permanent effects induced by the ion beam itself. Provided that this effect could be demonstrated to be controllable and reproducible, it could offer possibilities of mechanical characterization of the pillars under investigation that our picoindentation apparatus fell short of.

3.9 References

[1] H Gleiter, J Weissmuller, O Wollersheim, R Wurshum, Acta mater. 49 (2001) 737-745

[2] J Weissmuller, R N Viswanath, D Kramer, P Zimmer, R Wurschum, H Gleiter, Science 300, 312 (2003)

[3] D Kramer, R N Viswanath, J Weissmuller, Nano Lett., Vol. 4, No. 5, 2004

[4] I A Rahman, V Padavettan, Journal of Nanomaterials, 132424, 2012

[5] H K Kammler, L Madler, S E Pratsinis, Chem. Eng. Technol. 24 (2001) 6

[6] P Bagwe, C Yang, L R Hilliard, W Tan, Langmuir 2004, 20, 8336-8342

[7] I Vukovic, Block Copolymer Template-Directed Synthesis of Well-Ordered Metallic Nanostructures, Groningen University Press, Groningen, 2013

[8] N P Johnson, D W McComb, A Richel, B M Treble, R M De La Rue, Synthetic Metals, Volume 116, Issues 1–3, 1 January 2001, Pages 469-473

[9] W Jiang, W Yang, X Zeng, S Fu, J. Polym. Sci. A Polym. Chem. Volume 42, Issue 3, pages 733–741, 1 February 2004

[10] S Palzer, Influence of Supra-Molecular Structure and Storage Conditions on the Caking of Powders, Conference proceedings of 2006 Spring Meeting & 2nd Global Congress on Process Safety.

[11] E Detsi, Metallic Muscles: Enhanced Strain and Electrolyte-Free Actuation, Groningen University Press, Groningen, 2012

[12] J Biener, A M Hodge, J R Hayes, C A Volkert, L A Zepeda-Ruiz, A. V. Hamza, F. F. Abraham, Nano Letters 2006 Vol. 6, No. 10 2379-2382

[13] C A Volkert, E T Lilleodden, D Kramer, J Weissmuller, Appl. Phys. Lett. 89 061920 (2006)

Chapter 4

THE ORIGIN OF ION-BEAM-INDUCED BENDING

We have applied a novel approach to the investigation of deformation of nanoporous metals at the nanoscale by exposing nanoporous nanopillars to a Ga+ ion beam. We will show the results we have obtained with Au nanopillars but we have also observed similar behavior in Cu, Al and Ni nanopillars, i.e. a gradual massive deformation effect of the pillar during Ga ion beam exposure, where the pillar bends towards the ion beam. We derive a relationship between the formation of defects due to ion collisions in the nanopillar and the pillar's deformation and find that the deflection is linearly related to ion fluence. SRIM models have shown that deflection rate can be varied through change in acceleration voltage. This occurs due to the dual influence of a decreasing bending arm which reduces the associated bending moment, as well as the lowering ion concentration and thus defect concentration at the peak stress point. The high degree of control over deflection and the variables that influence it open an opportunity for use of IIB as a characterization technique.

4.1 Introduction

The investigation of ion-beam-induced bending starts with the search for its origins. In our own experiments, we have found that IIB first cropped up during work with submicron-scale pillars of nanoporous Au. These pillars were first produced for investigation into the mechanical properties of the metal by means of *in-situ* TEM picoindentation. During the shaping of these pillars, especially at the lowest length

scales, we frequently observed that, after milling was complete, pillars would end up deformed, bent. This was observed to be so consistent that a question arose on whether this deformation phenomenon could be controlled. Indeed, other groups had come to the same question and have performed remarkable experiments in high-precision deformation of nanowires and cantilevers [1-5].

The principle behind the process, however, remained mostly unexplored. Amongst the groups above, the most common explanation of the cause of the deformation was that it was an effect induced by ion beam treatment. It is worth noting that thermal or charge-based effects were discarded: similar experiments in a TEM, where thermal and charge conditions could surpass the FIB in intensity, no deformation of similar samples was observed. The explanation that Rajput *et al*. presented following an investigation into strips of crystalline silver was that the deformation is likely caused by the presence of defects introduced into the material during ion beam exposure and the subsequent knock-on effects produced as ions traveled within their target material [5]. While they did coin the term Ion Beam Induced Bending, or IIB, no further investigation into the mechanics of the effect followed.

Our own academic interest fueled the investigation into the properties and limits of IIB. As we performed more and more bending experiments, we came to the realization that, should a deterministic mechanical model be presented for the relationship between the ion beam input and the bending deformation output, then the IIB effect could be considered highly similar to any mechanical deformation through a conventional contact-based device. Our first objective then became the search for this model as, if the IIB could be adapted as an experimental tool, it could offer our investigation into ordered and disordered nanoporous material a degree of finesse and precision that other equipment simply could not provide.
In this study we focus on using IIB to investigate the ability of submicron size nanoporous gold to deform in a ductile manner. At first,

we report on extreme deflections in porous gold nanopillars having ligament and pore sizes of ~30nm. Second, we propose a quantitative model to account for these deformations. Our quantification approach considers the formation of a vacancy-rich region that induces a compressive stress that leads to a deflection. In this chapter we will present the results on nanoporous Au but have observed similar behavior on Cu, Al and Ni materials, i.e. a gradual massive deformation effect of the pillar during Ga ion beam exposure, where the pillar bends towards the ion beam.

4.2 Experimental method

Porous nanopillars were cut from a thin sheet of nanoporous Au, made by free corrosion of Au-Ag binary alloy foil with composition $Au_{35}Ag_{65}$ at% [6]. The resultant sheet of nanoporous Au is considered to be homogeneously porous, provided that the source material is a high-quality alloy. The porosity of the sheet depends on initial composition, and, in the case of this investigation, the porosity is 60%. Pillars then cut from this sheet have the same pore-ligament and porosity characteristics as the source sheet. Non-tapering of the nanopillars sides was achieved by using a custom Focused Ion Beam (FIB) milling technique [7-9].

Common milling techniques introduce tapering, where the cross-sectional area of the pillar decreases as a function of the distance from the base of the pillar such that the pillar is thickest at its base and thinnest at its tip. As we are interested in the mechanical behavior of the pillar across its entire length, we wish to ensure a uniform pillar's diameter. Our procedure ensures such a taper-free pillar's geometry. A set of fully taper-free nanoporous Au pillars with diameter 500nm was fabricated by means of a dual beam FIB/scanning electron microscope (SEM) microscope (Lyra, Tescan, CZ).

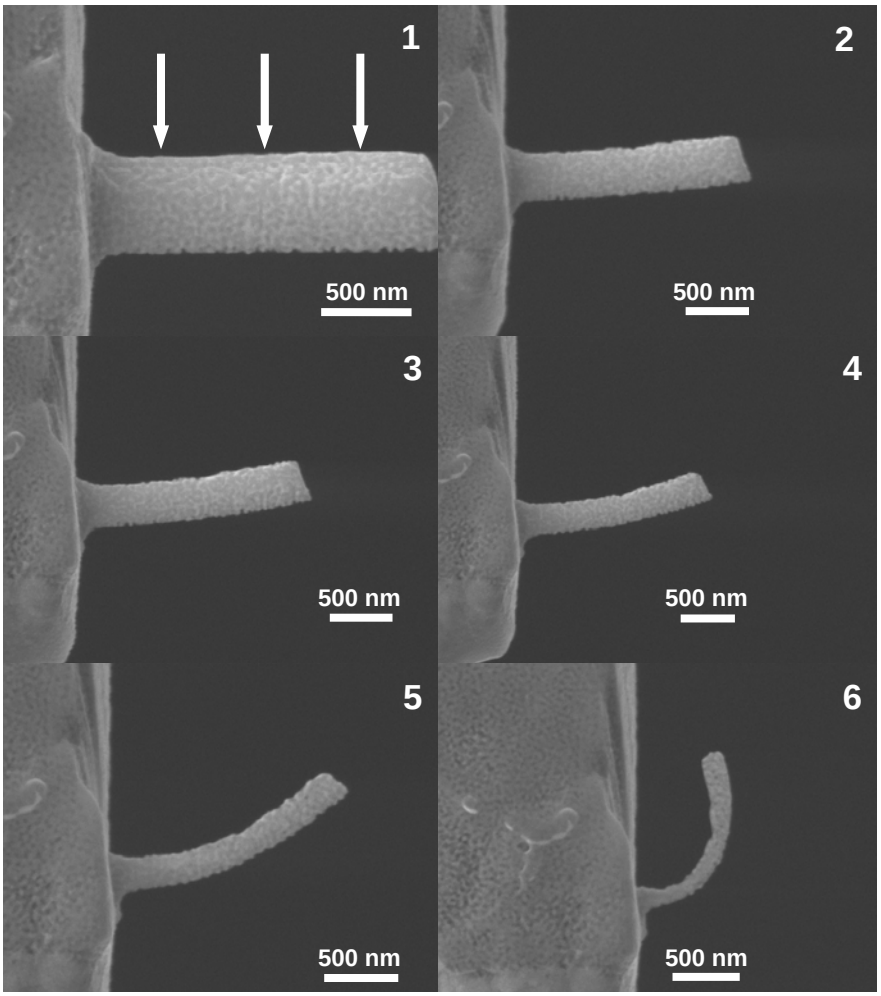

Figure 4.1: Progressive deformation of nanoporous Au pillar. Bending occurs towards the direction of the ion beam. Thick arrows indicate projected direction of beam incidence.

The aspect ratio of the pillars was initially chosen to be in the range of 2-3. We use this initial aspect ratio for simplicity: it is easy to ion mill the nanoporous Au to the correct dimensions while retaining reasonable structural stability and mechanical properties for handling. Pillar deformation was induced using the same equipment. Each pillar was aligned perpendicular to the beam to fully expose one of its faces. This leaves the opposing face in the ion beam's shadow.

Variation was possible in probe current and size of exposed area. Ion beam energy was maintained constant at 30kV, and probe currents of 1, 10, 40 and 150pA were selected for the experiment. We note that the presented values are software-controlled current presets, and may vary from the actual beam current emitted by the ion beam source. In every case, true ion beam current values are used. Irradiation was carried out for up to 2 seconds at 150pA, up to 5 seconds at 40pA, up to 20 seconds at 10pA and up to 200 seconds at 1pA for high fluence conditions of 10^{17} ions/cm^2. When a pillar is exposed to the ion beam, a gradual deformation towards the direction of the incident ion beam takes place as shown in Figure 4.1. A Cartesian coordinate system (x, y, z) is used to indicate the respective directions of the ion beam and the pillars: the ion beam is incident from the y-direction under an angle of 55 degrees up from the y-axis and non-deformed pillars are initially oriented in the x-direction.

4.3 IIB in action

As illustrated in Figure 4.1, a pillar with initial diameter ~500nm does not undergo noticeable deformation upon ion beam exposure. Rather, a gradual reduction of the pillar's diameter is observed. As a consequence, the pillar's aspect ratio will increase up to 8-10 as diameter decreases. As the pillar's diameter becomes small, a massive deformation of the pillar is observed, from the initial orientation in the x-direction (see sequence 1 in Figure 4.1) to a different orientation in the y-direction (see sequence 6 in Figure 4.1).

This large deformation in microscopic nanoporous Au samples is intriguing in the sense that it cannot be achieved in their macroscopic bulk counterparts, which are known for their highly brittle nature [10]. The ion beam technique turns out to be a suitable tool to manipulate microscopic pillars and can therefore be exploited to investigate the mechanical behavior of microscopic samples, provided that a quantitative relationship is established between the ion beam radiation and the deformation of these microscopic samples.

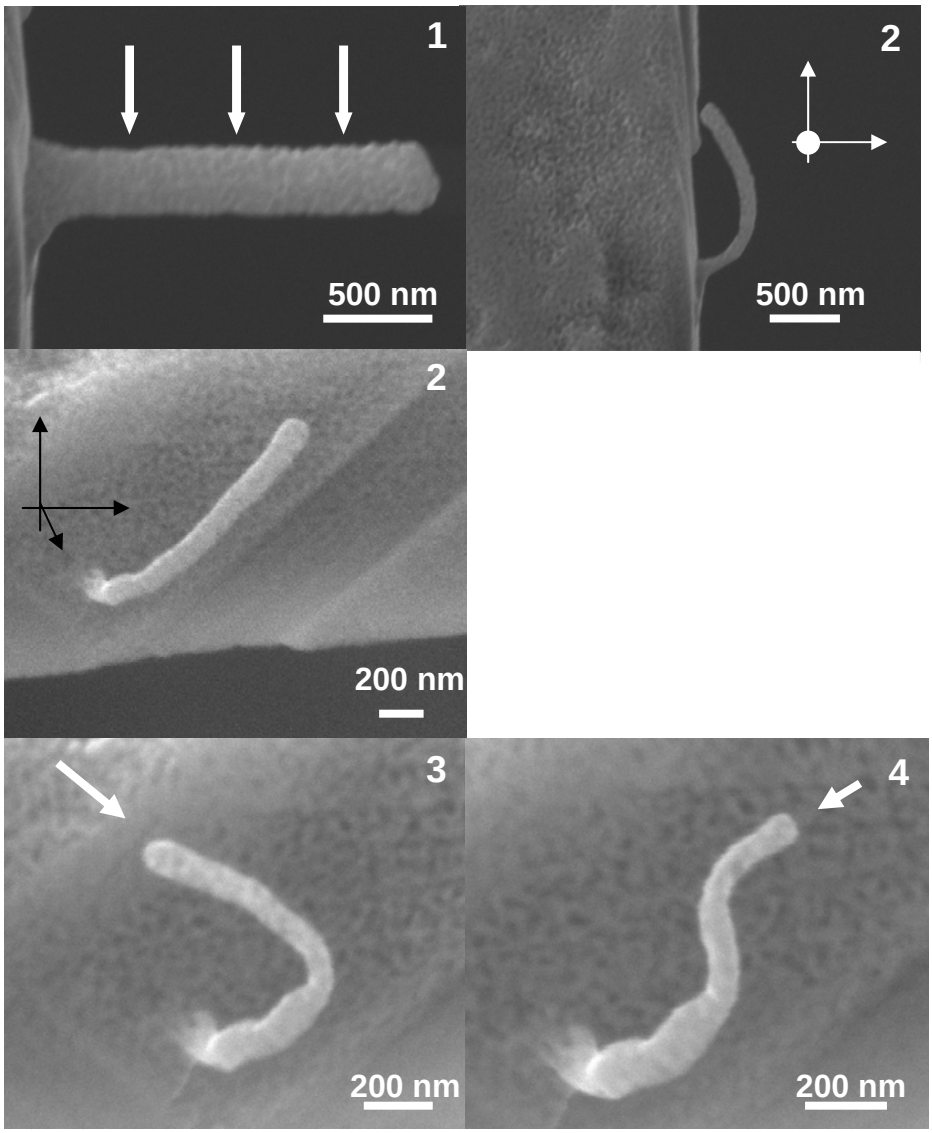

Figure 4.2: Preparation (upper row) and precision bending (lower row) of Au nanoporous pillar to form a complex shape. Arrows indicate projected direction of beam incidence. Co-ordinate systems apply to their respective rows.

A first step towards such a relationship will be presented in a later section. In fact, the usage of ion beam radiation as an experimental tool or the study of the mechanical behavior of microscopic test specimens is further motivated by the high precision of this technique, which

makes it possible to locally deform microscopic samples as we demonstrate in our next experiment: here a pillar with a starting cross-section diameter of ~70nm is partially exposed to ion beam radiation, rather than a full exposure as in the previous experiment, in other words, where before we had irradiated an entire pillar face with ions, in this experiment we focus the beam on a small area along the pillar's length.

The pillar adopts a sharp bend and only the exposed part bends towards the beam. Due to the localization of the bending, it is possible to micro-manipulate the pillar into a shape of our choosing by virtue of altering irradiation angles. In this case, we form the pillar into an S-shape by bending it at two points as demonstrated in Figure 4.2. All deformations seen were achieved by changing the relative orientations of the pillar and the beam, as the pillar is only capable of bending towards the beam.

4.4 The origin model

It has been postulated that the bending effect in nanopillars stems from stresses arising from defects formed in the material during ion beam radiation [5]. For such a bending even to occur, a bending moment has to be present to cause a deflection.

Considering mechanics

Stopping Range of Ions in Matter (SRIM, version 2012.03, [11]) simulations allow us to see the effects of ions impinging upon a solid target. A typical result for SRIM of a gold surface exposed to a 30kV Ga ion beam is shown in figure 4.3.

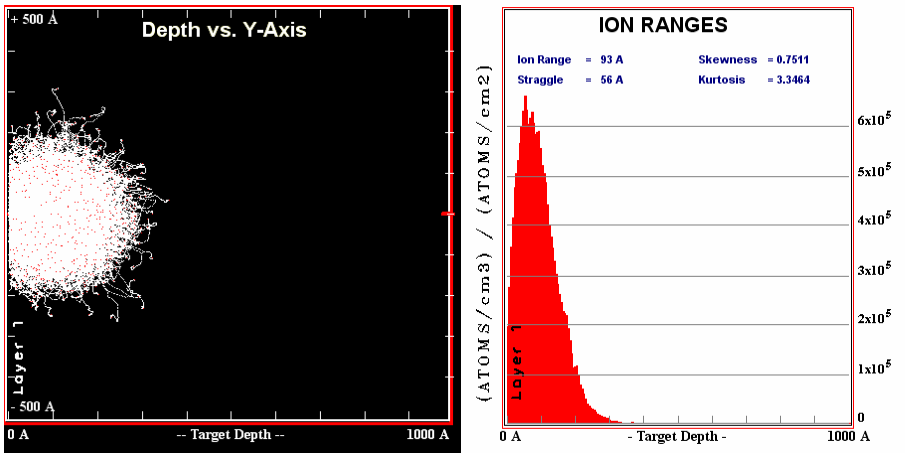

Figure 4.3: SRIM simulation of ion paths through solid matter (left) and the frequency distribution of ion penetration depth (right).

As an ion generates an approximately fixed number of vacancies, the shape of the ion penetration distribution is then the same as the shape of the distribution of defects created through ionic knock-on effects. We see that the region beneath the surface facing the ion beam holds the vast majority of defects, leading to an anisotropic defect concentration across the pillar. This has the potential to lead to the formation of a bending moment.

The defect distribution induced through ion collisions seen in figure 4.3 can be modeled as symmetrical and triangular. As the stress profile scales linearly with the defect profile, the aggregate compressive force is then the area of the stress profile. In the bilayer system of vacancy-rich and vacancy-free layers of the pillar, the pure compressive stress experienced by the vacancy-rich area translates into a bending moment M towards the ion beam through the force x arm expression, with force being the pure compressive component of the vacancy-rich area and arm the distance between the mid-point of the pillar's width and the mid-point of the stress profile, as shown in figure 4.4.

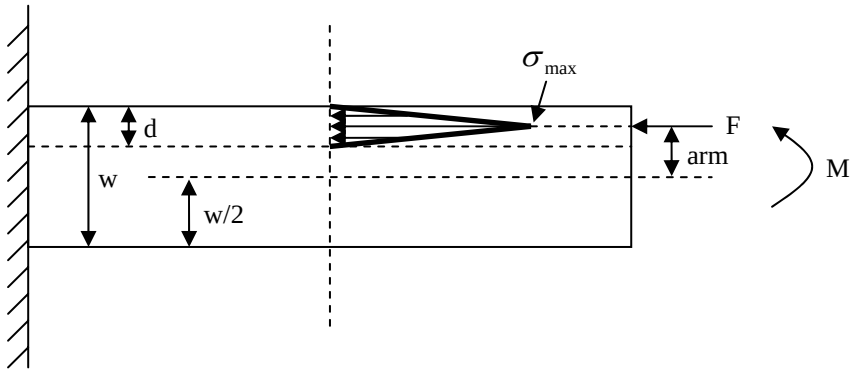

Figure 4.4: Schematic diagram of the stress profile induced in a pillar through the production of a vacancy-rich layer.

$$M = \frac{\sigma_{\max} d}{2} \cdot \left(\frac{w}{2} - \frac{d}{2} \right) = \frac{\sigma_{\max} d}{4} \cdot (w - d) \tag{4.1}$$

where M is the bending moment, $\sigma_{\max}$ is the stress at the peak of the stress profile, w is pillar width and d is the width of the stress profile.

We substitute this into the expression for the deflection $\delta(x)$ of a cantilever beam subject to a bending moment M:

$$\delta(x) = \frac{Mx^2}{2EI} = \frac{\sigma_{\max} d(w-d)x^2}{8Ew^3/12} = \frac{3}{2} \cdot \frac{\sigma_{\max}}{E} \cdot \frac{d(w-d)}{w^3} x^2 \tag{4.2}$$

thus showing the relationship between the stress at the peak of the stress profile $\sigma_{\max}$ and the resultant deflection of the pillar $\delta(x)$.

Considering physics

Taking stress ε and strain σ as related by elasticity, we relate the stress formed in the vacancy-rich region to the strain via the modulus E and Poisson's ratio ν

$$\sigma(z) = -\frac{E}{1-\nu} \cdot \varepsilon(z) \tag{4.3}$$

During ion exposure three types of defects will be formed: vacancy-interstitial pairs and Ga interstitials. Each Ga+ ion impact can form up to 300 vacancies and self-interstitials. We can express the contribution of point defects to strain as linear, and thus take the sum contribution of each type of defect.

$$\varepsilon = \frac{1}{3}\left\{ \frac{\Delta\Omega_v}{\Omega} \cdot \frac{n_v}{n} + \frac{\Delta\Omega_{\text{int}}}{\Omega} \cdot \frac{n_{\text{int}}}{n} + \frac{\Delta\Omega_{ion}}{\Omega} \cdot \frac{n_{ion}}{n} \right\} \tag{4.4}$$

where $\frac{n_x}{n}$ is the number of defects over number of all lattice sites, where v, int and ion denote vacancies, interstitials and ionic defects respectively, and $\frac{\Delta\Omega_x}{\Omega}$ is the number of specific defect types of all defects caused by ionic implantation. We note that the Au self-interstitials at room temperature are more mobile than their paired vacancies, and thus have a far greater chance to move to the surface, where they no longer contribute to the stress [12]. In addition, we consider the contribution of Ga+ ions as negligible due to there being far more vacancies than ions. As such, we can express the defect contribution to strain as

$$\varepsilon = \frac{\Delta\Omega_v}{\Omega} \cdot \frac{n_v}{n} \tag{4.5}$$

We take the distribution of vacancies as following a decaying distribution such that the number of vacancies is related to ion fluence by

$$n_v(z) = \alpha_v(z)\beta^{-1}\left(1 - e^{-\beta\Phi}\right) \tag{4.6}$$

where Φ is ion fluence, and β is a constant such that the term in the exponent becomes dimensionless. At low dose conditions, the decay function approximates to $1-\beta\Phi$ such that

$$n_v(z) = \alpha_v(z)\Phi \tag{4.7}$$

Where $\alpha_v(z)$ is the term describing the shape of the vacancy distribution, which, from SRIM, we know to be triangular. This demonstrates the linear sequence of events starting with ion impact to formation of vacancy to the induction of stress and the bending deformation.

Effects of ion energy

We are interested in the effects of the total depth of the stress profile on the resultant bending moment. This depth is influenced by the depth of the defect profile and, thus, on the penetration capability of incident gallium ions. As such, we examine the defect profiles created by incident Ga ions of varying acceleration voltages, as shown in figures 4.5-4.9. To form these profiles, we fix the number of incident ions at 10000. As penetration depth is low in Au, we use Al as a target to better demonstrate the shape of the penetration profile.

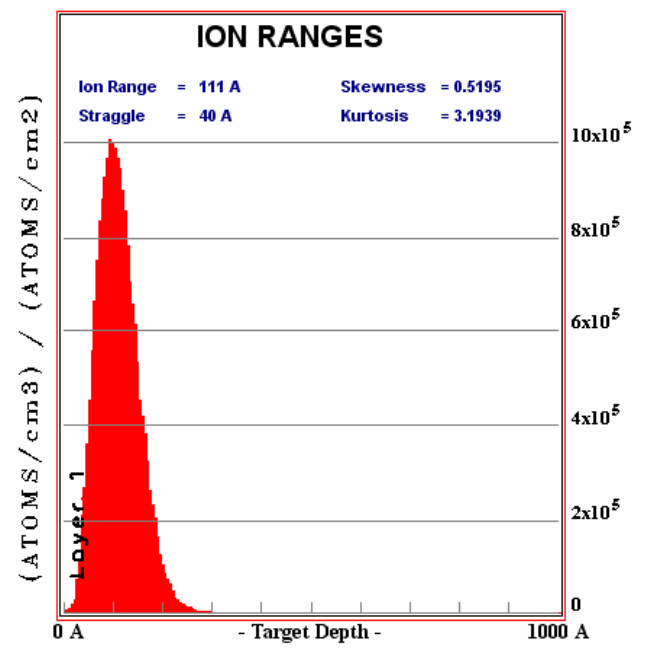

Figure 4.5: SRIM simulation of defect profile from 10kV Ga ions.

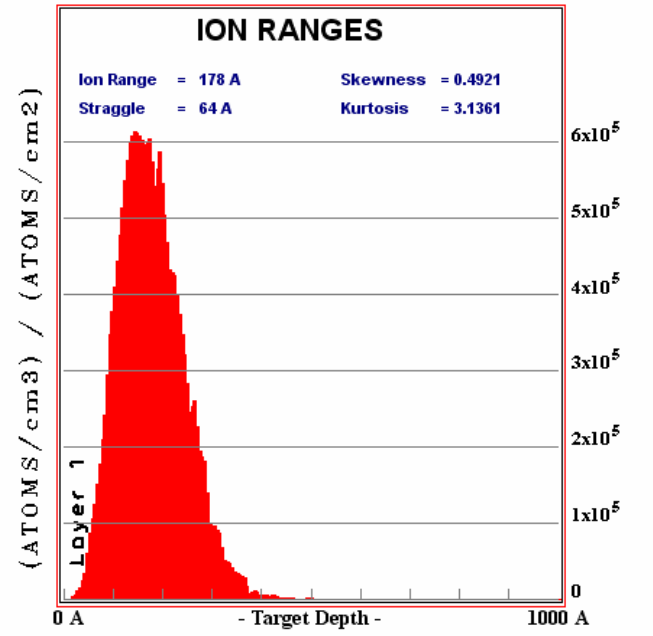

Figure 4.6: SRIM simulation of defect profile from 20kV Ga ions.

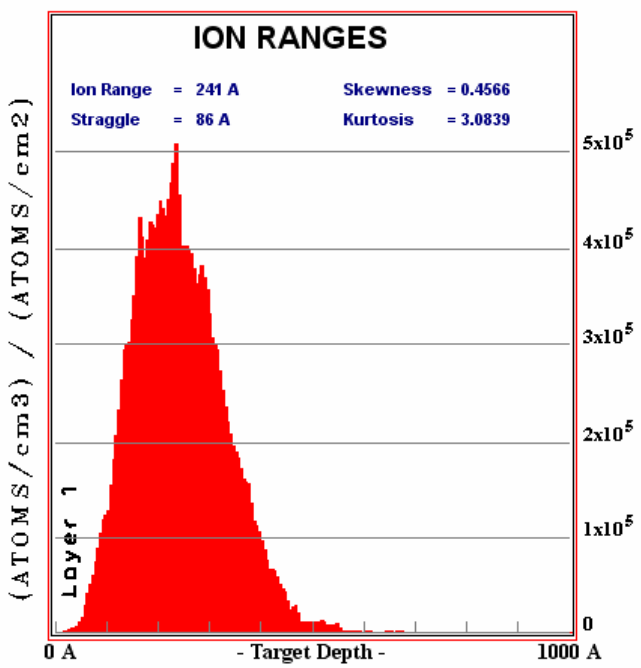

Figure 4.7: SRIM simulation of defect profile from 30kV Ga ions.

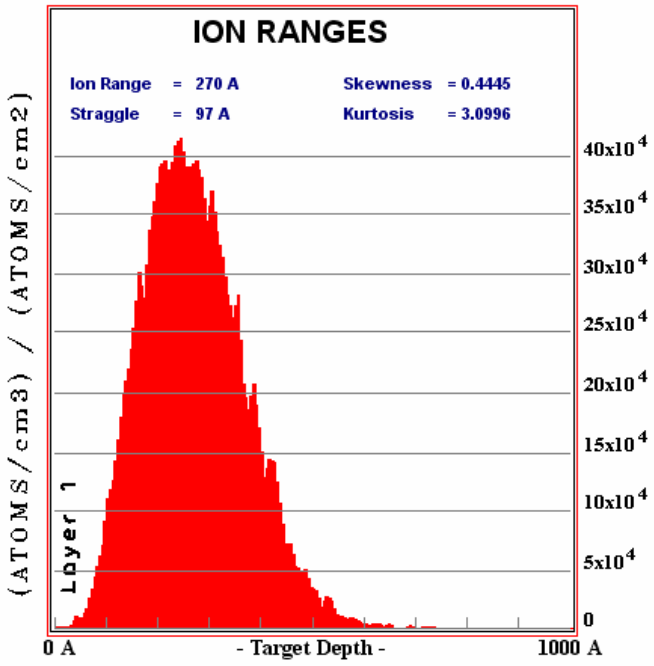

Figure 4.8: SRIM simulation of defect profile from 35kV Ga ions.

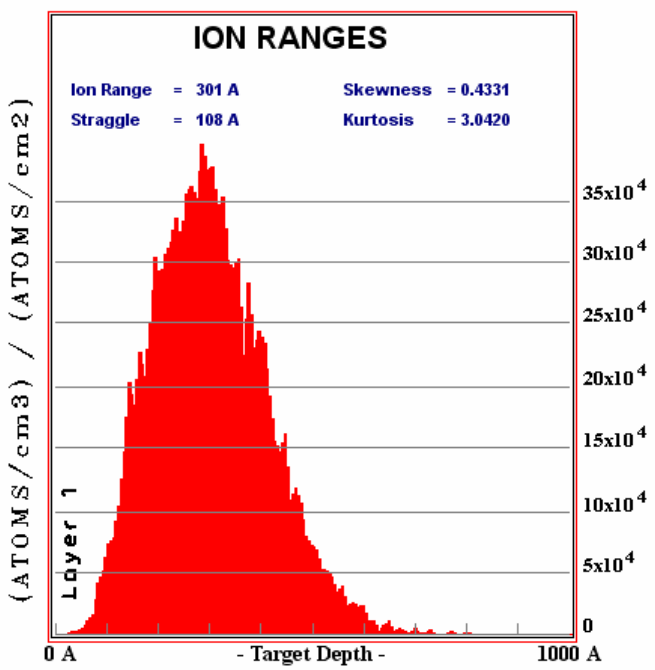

Figure 4.9: SRIM simulation of defect profile from 40kV Ga ions.

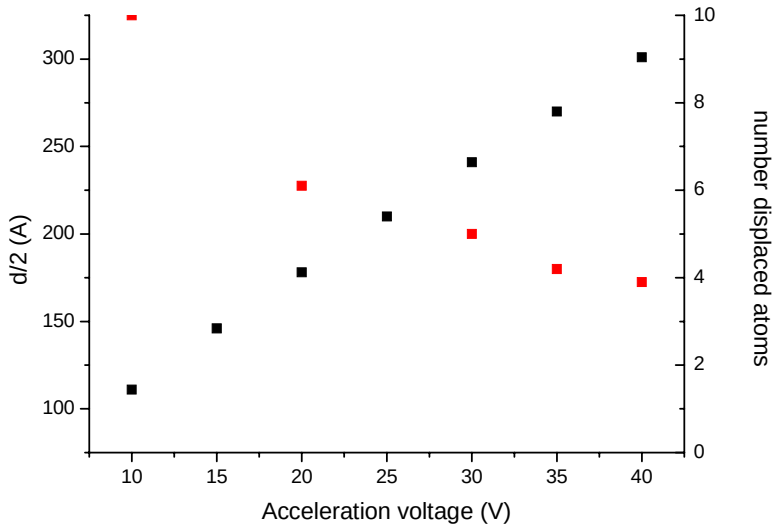

Figure 4.10: Increasing d/2 (blue) and decreasing displaced atom count at σ_{max} (red) with increasing ion energy.

As can be seen in the figures presented above, as ion energy increases, so does the penetration depth. As the bending moment is dependent upon the size of the bending arm in relation to the pillar width, and the arm decreases in size as penetration increases, then the bending moment at high ion energies for a set number of ions is lower than the moment at low ion energies. In addition, as penetration depth increases, $\sigma_{\max}$ decreases, also contributing to a reduction of $\delta(x)$. In other words, a pillar will bend quicker and sooner if acceleration energy is low.

4.5 A first estimation

We can estimate the values of the bending stress from typical deflection values observed in our pillars. We take the elastic modulus of nanoporous gold as 9GPa [13], the pillar length as 1500nm, pillar width as 150nm and a typical deflection as 500nm. In addition, SRIM models d/2 in Au at 30kV to be 10nm deep. The pillar's $\sigma_{\max}$ can be then calculated to be 1.7GPa. This is extremely high, and is likely an overestimation of the true value, as there are several factors that our models do not take into consideration.

We expect that porous microstructure will have an effect on the stress and resultant deflection, including ligament diameter, degree of porosity, cell morphology etc. Additionally, exposing a pillar to the ion beam for so long so as to achieve such a large deflection may involve additional influences caused by removal of material due to the ion beam. We leave these influences as a question open for further studies.

From these observations we can additionally conclude that a nanoporous target applies an enhancement effect to IIB. Specifically, provided that the dimensional requirements are met, i.e. the pillar is thin enough to be deformed in the first place, a nanoporous pillar will prove easier to bend than a bulk one for a given pillar diameter. This is due to the softness that we observe in nanoporous nanopillars that stems from the weak contribution from surface ligaments.

4.6 Conclusion

In conclusion, in our work we demonstrate the capacity of nanoporous Au to deform in a ductile manner. We have applied a novel approach to the investigation of this deformation of nanoporous Au at the nanoscale by exposing nanoporous Au nanopillars to a Ga+ ion beam. We observed a gradual massive deformation effect of the Au pillar (and similar results in Cu, Ni and Al) during Ga ion beam exposure, where the pillar bends towards the ion beam up to extremely high deflections.

The deformation is influenced by the ion fluence, and is a permanent effect. This deformation only occurs in pillars with an aspect ratio of 8-10, and requires a pillar diameter of 200-300nm. At greater diameters no or very little deformation occurs. We attribute the emerging ductile properties to the nanopillars' surface contributing weakly under compression and tension. With an estimated surface depth of 60nm, at 200-300nm the pillars are composed of majority surface. We derive a relationship between the formation of defects due to ion collisions in the nanopillar, the resultant formation of a stress profile due to vacancies and the pillar's deformation and find that a high acceleration voltage induces a deeper defect profile which in turn reduces the maximum stress and thus the strength of the bending moment.

We have shown the linear relationships between ion collision, defect formation and the resultant development of a stress profile. The effects of an ion beam on a pillar can therefore be predicted and the ion beam can be finely controlled in both shape and area of incidence, which opens options for the use of the Focused Ion Beam apparatus as a destructive but contact-free method for mechanical characterization of materials.

4.7 References

[1] Y -R Kim, P Chen, M J Aziz, D Branton, J J Vlassak, Journal of Applied Physics 100, 104322 (2006)

[2] T van Dillen, A Polman, C M van Kats, A van Blaaderen, Appl. Phys. Lett. 83 4315 (2003)

[3] B C Park, K Y Jung, W Y Song, B-h O, S J Ahn, Adv. Mater 18, 95 (2006)

[4] S K Tripathi, N Shukla, S Dhamodaran, V N Kulkarni, Nanotechnology 19, 205302 (2008)

[5] N S Rajput, A Banerjee, H C Verma, Nanotechnology 22 485302 (2011)

[6] E Detsi, Z G Chen, W P Vellinga, P R Onck, J Th M De Hosson, Applied Physics Letters 99, 083104 (2011).

[7] J R Greer, J Th M De Hosson, Progress in Materials Science 56, 654 (2011).

[8] C Q Chen, Y T Pei, O Kuzmin, Z Zhang, E Ma, J Th M De Hosson, Physical Review B 83, 180201 (2011).

[9] O V Kuzmin, Y T Pei, J Th M De Hosson, Applied Physics Letters 98,233104 (2011).

[10] J Biener, A Hodge, A Hamza, L Hsiung, J Satcher, Journal of Applied Physics 97, 024301 (2005)

[11] J F Ziegler, M D Ziegler, J P Biersack, Nuclear Instruments and Methods in Physics Research Section B: Beam Interactions with Materials and Atoms, Volume 268, Issues 11–12, June 2010, Pages 1818-1823

[12] J Th M De Hosson, A Van Veen, Encyclopedia of Nanoscience and Nanotechnology, American Scientific Publishers, volume VII, 2004, pp.297-349. and reference therein.

[13] D Lee, X Wei, X Chen, M Zhao, S C Jun, J Hone, E G Herbert, W C Oliver, J K Kysar, Scripta Materialia 56 ,437 (2007)

Chapter 5

SOLID METALLIC NANOPILLARS UNDER ION-BEAM-INDUCED-BENDING

We have observed two different modes of bending in metallic nanopillars when exposed to an ion beam: homogeneous and point-bending. We show that different metals tend towards one or the other behaviour and attribute this tendency to inhomogeneities in the nanopillars itself: bending will be stronger in crystalline areas and weaker in areas amorphised during ion beam processing. We see that aluminium shows homogeneous bending due to a strong tendency to amorphise, copper shows strong point-bending tendencies due to clear variations in its microstructure that we observe in TEM and gold tends to point-bend due to microstructural inhomogeneities at the grain level. We use the Kinchin-Pease model to calculate the number of defects formed due to ion collisions and connect this with a penetration profile produced through SRIM to predict a defect concentration profile produced during IIB. Finally, by associating the defect profile to a resultant stress profile that leads to bending we are able to show a growing stress profile as a function of depth and ion exposure time.

5.1 Introduction

A model is now in place for the underlying principles of ion-beam-induced bending (IIB): as a defect-rich layer builds up through continuous ion exposure, the lattice stress of each point defect

contributes linearly to an aggregate stress across the defect-rich region. A bilayer effect is the result, where the defect-rich region experiences compressive stress and the defect-free region – where the ions have not penetrated – remains stress-neutral, with the overall effect being a bending deformation in the direction of the ion beam's source. In the previous chapter we have shown that there exists a linear relationship between the properties of an ion impact event, the development of defects during its propagation through the material and the nature of the resultant stress profile. This linearity allows for quantitative predictions in a deterministic manner of the mechanical properties of a material, provided the properties of the FIB are known. We are interested in further empirical data to expand our comprehension of the full effects of IIB, however, as the stronger a comparative baseline we can provide, the stronger our case for the use of IIB as a mechanical characterization tool would be.

The importance of investigating the IIB response characteristics of solid metals stems from the well-known properties of these metals. To reiterate, our final objective is to investigate the properties of nanoporous metals and to make a comparative analysis between ordered and disordered nanopores morphologies. In addition, we want to use IIB to do so, as the precision and control that it potentially offers could be extremely useful. However, nanoporous metals are far more complex than their solid counterparts, and the behaviour difference between the classical bulk crystalline morphology and the nanoporous pore-ligament morphology has been observed to be so significant that current scaling laws need readjustment before being applied to a nanoporous system [1].

Therefore, a comparison must be drawn between the IIB response of a nanoporous system and its crystalline bulk counterpart with as many different metallic systems as possible. We note that, in a bulk crystalline material, intrinsic material properties will be a major influence on the bending behaviour of a structure. Ions will have a preferential direction of travel within a crystalline lattice depending on

crystal orientation, which can lead to an anisotropic distribution of stress fields within the defect-filled layer. This manner of anisotropy can lead to preferential bending directions during IIB or even localized bending events. At a larger scale, any microstructural defects at the surface of the sample, induced through preparation or in the FIB, can strongly influence behaviour during IIB.

For this investigation we perform IIB on the most common crystalline materials that have the potential to be also produced as a nanoporous system: Au, Cu and Al. By finding commonalities between the behaviour of these pillars we hope to be able to develop a procedure that can be applied to any type of pillar without prior reference.

5.2 Experimental method

Au and Cu shot of high purity (99.99+%) were purchased from Alfa Aesar. Pure metal buttons were produced by melting together Au or Cu shot inside an arc furnace. Buttons were then each cold-rolled into thin sheets of approximate thickness 20-50μm. They were then annealed in a furnace at 400°C overnight to permit recrystallization to happen. Al foil of 99.6% purity with initial thickness of 750nm was purchased from Goodfellow Metals.

Nanopillars were cut from prepared material. Non-tapering of the nanopillar sides was achieved by using a custom FIB milling technique. Common milling techniques introduce tapering, during which the cross-sectional area across the length gradually becomes thicker towards its base. As we are interested in the bending behavior of the pillar across its entire length, we wish to ensure a uniform diameter. Our procedure ensures such geometry. A set of fully taper-free pillars with diameter ~250nm was fabricated by means of a dual beam FIB/SEM microscope (Lyra, Tescan, CZ). The aspect ratio of the pillars was initially chosen to be in the range of 2-3 for ease of production and further mechanical stability.

Pillar deformation was induced using a dual beam FIB/SEM microscope (Lyra, Tescan, CZ). Each pillar was aligned perpendicular to the beam to fully expose one of its faces. This leaves the opposing face in the ion beam's shadow.

Aluminium was prepared for TEM by means of electropolishing using a TENUPOL III electrochemical polishing apparatus. 3-mm diameter discs are affixed in a specialized holder that allows an electrolyte to be sprayed at a single point from diametrically opposing sides of the disc. A voltage is applied in order to produce a current due to anodic dissolution of the disc and thus develop a polished surface. Voltage is set to 20V, with electrolyte composition of 10% nitric acid and 90% methanol. The electrolyte was cooled to -30°C to ensure a more controlled polishing process.

5.3 Results

Aluminium pillars

Electropolishing of the aluminium foil yields an electron-transparent region suitable for TEM observation. As shown in Figure 5.1, prior to FIB treatment the foil is highly crystalline with large grains.

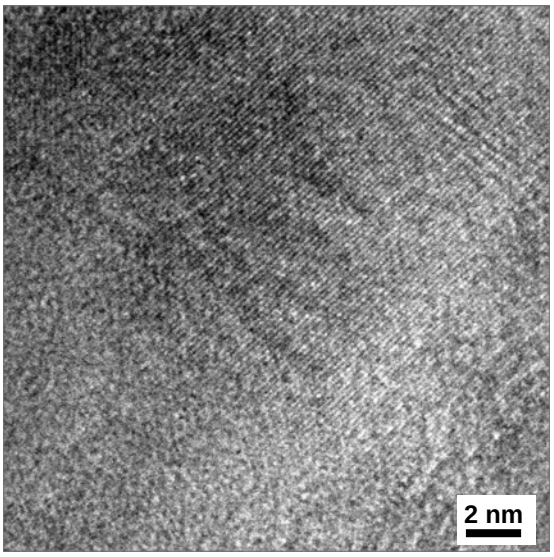

Figure 5.1: TEM micrograph of lattice fringes in Al foil.

A typical grain might be several dozen up to a hundred nm wide [2]. Considering that the initial pillar width is around 200nm it can be concluded that pillars will be polycrystalline.

TEM observation also shows amorphous regions of aluminium oxide in some locations in the electropolished areas, amongst them the extreme edges of the foil. The typical thickness of an oxide layer in Al is approximately 3-4 nm [3], and can also be observed figure 5.4.

The foil has been observed to be generally defect-free, with few, if any, defects to be found under TEM. As such, it will be considered that, in their initial state, pillars made from the aluminium foil will also be free from defects.

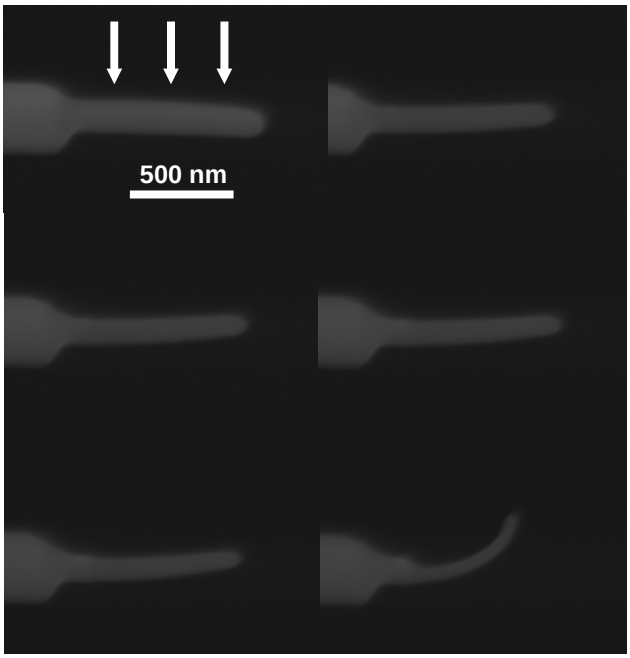

Figure 5.2: SEM micrograph of IIB of an aluminium pillar.

The expected result during IIB of a pillar is a homogeneous bend, such that the shape of the pillar follows a single radius of curvature from base to tip. However, two different modes of bending were observed during experimentation, as demonstrated in Figure 5.3.

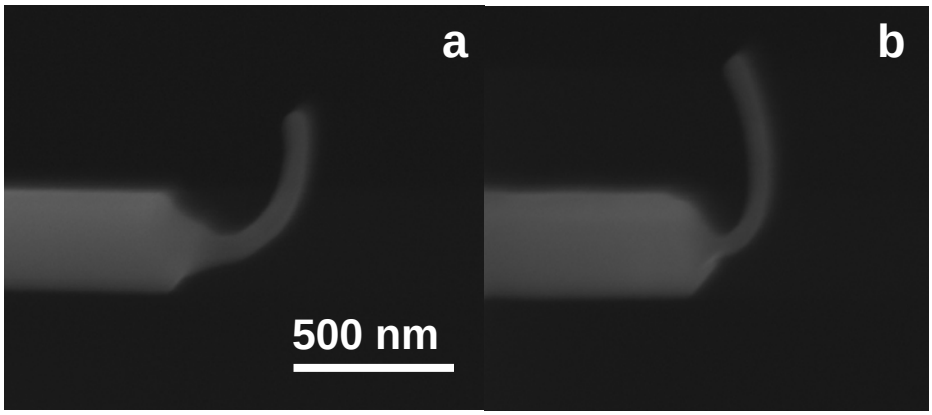

Figure 5.3: Modes of pillar bending: homogeneous (a) or point-bend (b).

Pillars have been observed to either undergo a slow homogeneous bend, characterized by a singular radius of curvature at all times, as well as a constant cross-sectional diameter at every point in the pillar during beam exposure, or a fast point-bend, where the pillar remains mostly straight throughout beam exposure except for a singular point along the length of the pillar whose radius of curvature rapidly decreases. The nucleation point of a point-bend can be at any place along the pillar length, and varies from pillar to pillar.

TEM observation was performed on both pillars that have undergone homogeneous bending as well as point-bending. Whereas the initial foil is clearly crystalline, large amorphous regions are visible in pillars that are clearly beyond the size of the expected aluminium oxide region. These amorphous areas are attributed to the effects of the ion beam itself, which is known to induce amorphisation through ion impact. The extent of the amorphisation is expected to be approximately similar across the pillar's diameter, as the production method requires that the beam touch every face of the pillar.

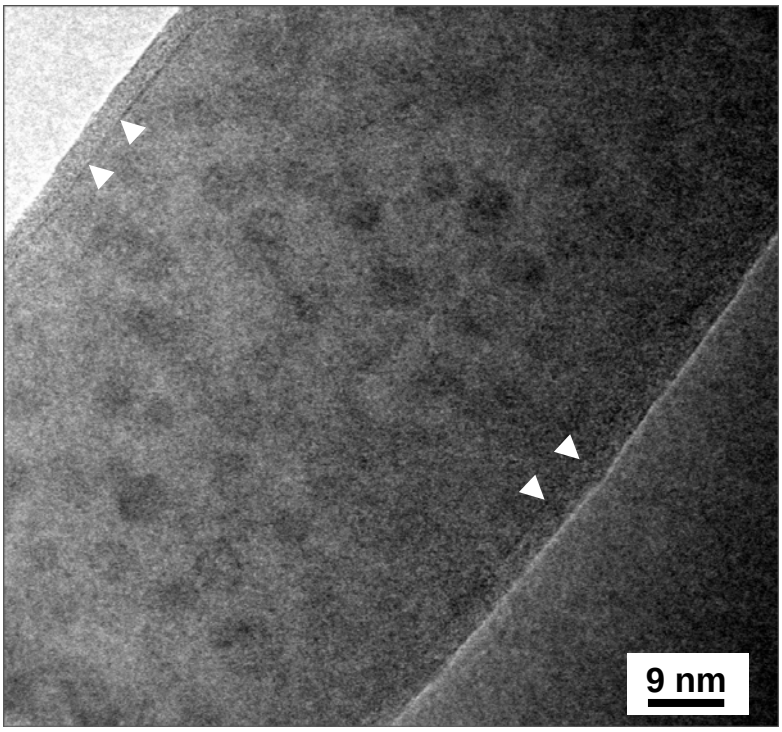

Figure 5.4: Amorphisation across a pillar. Oxide layer denoted by arrows.

.

Amorphous regions such as those shown in Figure 5.4 also consistently share a feature in the darker spherical shapes of varying diameters scattered throughout. These are likely recrystallized areas formed due to agglomeration of atoms induced by ion impacts. In a pillar that undergoes homogeneous bending, such amorphisation is homogeneous throughout the pillar. Diffraction was unable to clearly identify crystalline regions, as pillar thickness was already at the stage where TEM observation became very difficult.

There is, however, a clear inhomogeneity expected and visible in pillars that have undergone point-bending, demonstrated in Figure 5.5.

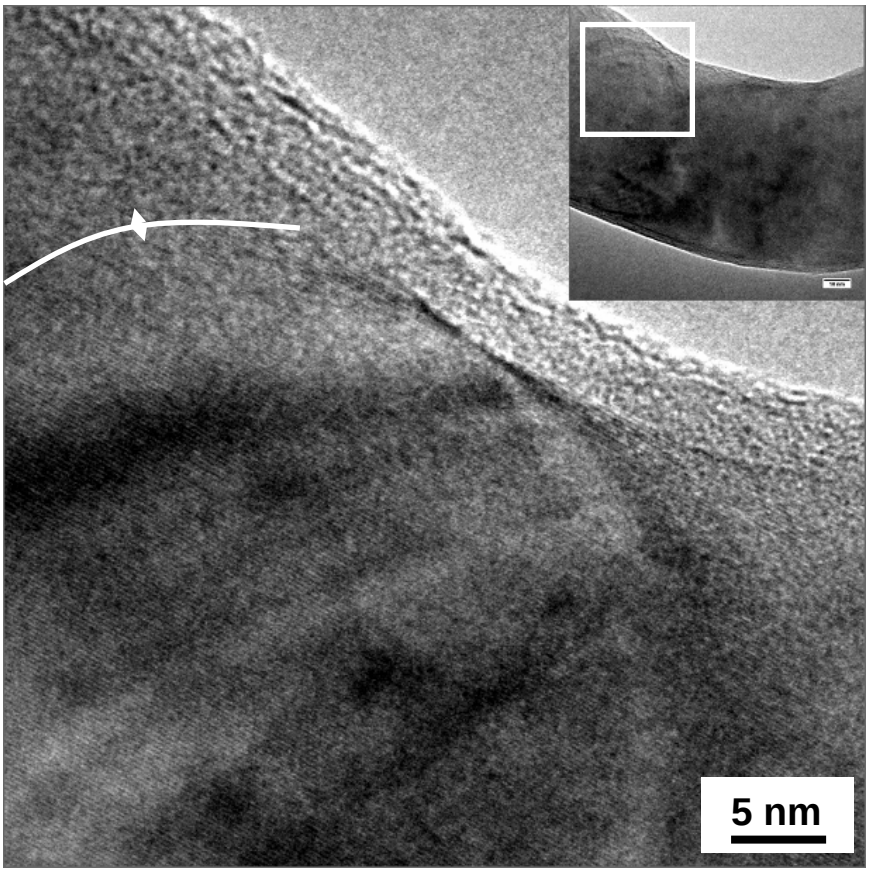

Figure 5.5: Demarcation line between amorphous (up) and crystalline (down) regions in Al. Circular patterns bounding region of point-bend (inset).

In all cases of point-bending, pillars have preferentially deformed around a crystalline region bounded by amorphised areas. The dark patterns encircling the outside of the pillar are likely defect agglomerations formed as a result of the pillar's bending. It can be concluded that the homogeneity of a structure strongly affects the result of IIB, and that crystalline regions make a far greater contribution to IIB than amorphous ones. This becomes clear when we consider that the bending effect stems from the formation of crystalline vacancies that induce a compressive stress across a specific face of the pillar.

Copper pillars

IIB of copper showed a far stronger tendency towards point-bending than aluminium, as demonstrated in Figure 5.6.

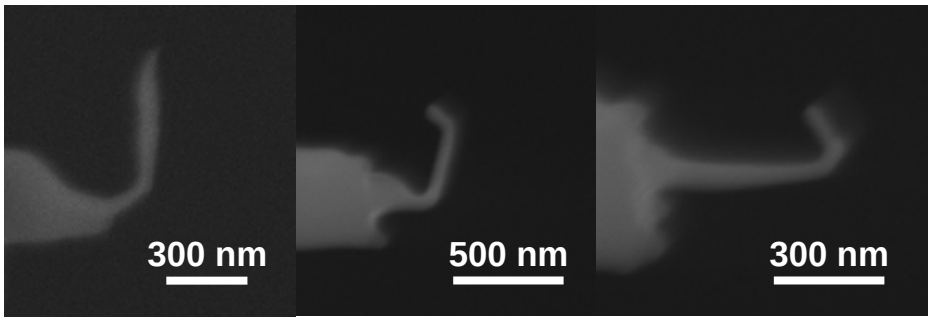

Figure 5.6: Point-bending of solid Cu pillars.

TEM observation of point-bend locations, seen in Figure 5.7, produced results correlating with the behaviour seen in aluminium: preferential bending occurred in crystalline areas that have not been amorphised during pillar processing and IIB.

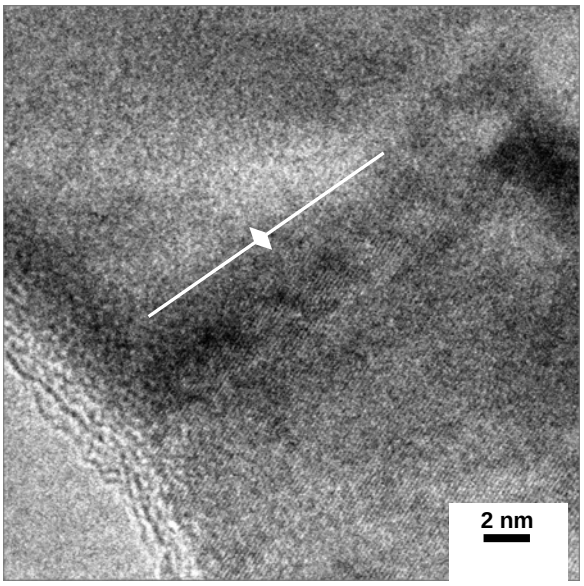

Figure 5.7: Demarcation between amorphous (up) and crystalline (down) regions in Cu.

This particular bending behaviour reinforces our postulation that bending occurs preferentially around crystalline regions in a pillar, and will display point-bending behaviour if the majority of the pillar is amorphous.

Gold pillars

Investigation of Au pillars shows types bending behaviour, shown in Figure 5.8, similar to those observed in Al and Cu. In addition, however, Figure 5.8a shows bending occurring as a result of a section of pillar being thinner than the rest of the pillar.

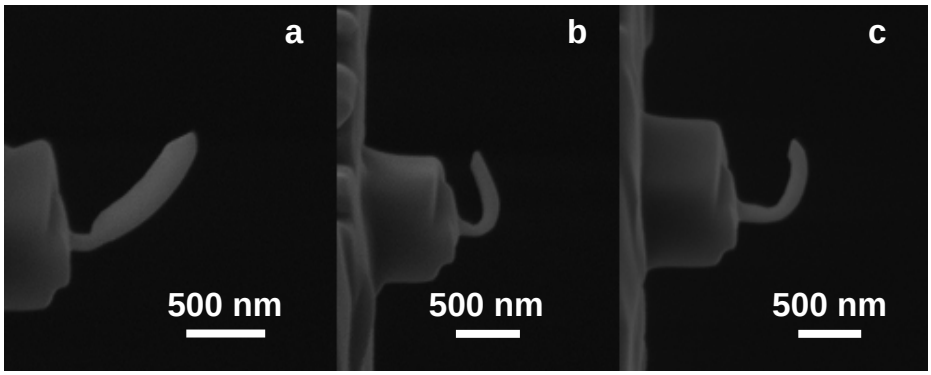

Figure 5.8: Preferential thinning (a), point-bending (b) and homogeneous bending (c) in Au.

TEM observation has shown the conservation of crystallinity throughout the entirety of the pillar despite processing and subsequent IIB, as shown in Figure 5.9, which suggests that preferential bending in Au pillars occurs due to more subtle inhomogeneities in the material where defects can nucleate and agglomerate to exert a compressive strain.

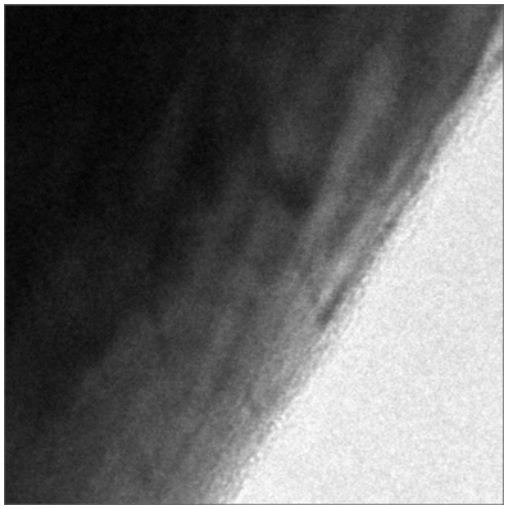

Figure 5.9: Crystalline fringes are faintly visible at the edge of a FIB-processed Au pillar.

5.4 Discussion

Aluminium pillars

Amorphisation is a common form of radiation damage in crystalline metals, characterized by loss of long-range ordering of a crystalline lattice caused by displacement of atoms by high-energy collisions. We expect that Al pillars would be easily amorphised due to the low energy required to displace an atom from its lattice site (the displacement energy E_d term will be presented in equation 5.1). For the case of an ionic impact, this low displacement energy contributes both to the total number of defects that will be formed along the ion's path, but also the total depth of the ion's penetration before it stops. In other words, for a material as easily amorphised as Al, a 100nm pillar is likely to be almost completely amorphous after processing but prior to bending. This presents an unexpected benefit to working with aluminium pillars. Specifically, we have mentioned that inhomogeneities within a pillar can have an influence on the pillar's bending behaviour, and crystalline orientation can lead to preferential propagation directions of ions along loosely-packed crystalline planes.

In the case of polycrystalline aluminium pillars, the penetration profile of a given ion will not be constant throughout the pillar, and thus it would be impossible to predict a pillar's bending behaviour without extensive investigation of its crystalline structure before, after and during IIB. However, such issues are not present in an amorphous pillar, where the material can be expected to be homogeneous at all points. As can be seen from our results, aluminium pillars are the most likely to bend homogeneously, and this is an obvious consequence of homogenization through amorphisation. This point is reinforced by the observation of point-bending in an aluminium pillar that has not fully undergone amorphisation. In the case of Figure 5.5 we see that the bending effect is strongest in a crystalline region. This stems from mechanisms of point defect production that occur during ion impact

events in varying between crystalline and amorphous regions. We have established that in a crystalline region defects are formed as a direct result of atoms leaving their lattice sites due to ion knock-on. In an amorphous region, however, there is no clear demarcation of lattice sites and, therefore, the formation of point defects is a much more limited process that involves the gradual aggregation of voids. As such, the bending effect in an amorphous pillar will be slower and more limited.

With this we are forced to consider the immediate limitations of IIB: while still entirely applicable as a tool for localized mechanical deformation of submicron features in a wide variety of metals, it cannot be used in a predictive manner for the characterization of all polycrystalline metals. Those metals that do not amorphise as easily as copper during production, or those whose crystallinity is a fundamental aspect of their nature such that amorphisation would drastically change that are incompatible with IIB. In such cases, single-crystallinity would have to be ensured prior to experimentation. Otherwise, for cases where amorphisation can be performed easily and without consequences, aluminium pillars present a strong baseline of comparison, as they are not affected by plastic effects and bend entirely elastically.

Copper pillars

A notable difference between copper and aluminium pillars is the far greater tendency of copper pillars to point-bend: all copper pillars in a batch of 20 examined showed point-bending. In terms of ion collisions, copper has the higher displacement energy term of the two metals so the degree of amorphisation at equal ion fluence for copper will be lower, leading to there being more and larger crystalline regions. For the case of a metallic pillar with both amorphous and crystalline regions we know that the most likely response will be point-bending due to bending in crystalline regions being the dominant behaviour.

Gold pillars

For the case of gold, whose displacement energy term is far higher than that of copper and aluminium, and where the partial amorphisation has not been observed, the tendency towards preferential point-bending comes from different sources. In Figure 5.8a a rapid reduction in diameter can be observed at the very base of the pillar. This is a unique case, as no such reductions are visible in other gold pillars.

In our previous work we have discussed the presence of a critical diameter that has to be reached before a pillar begins to bend under IIB. It then stands to reason that if a pillar reaches such a diameter locally then bending will be preferential in that area. For Figure 5.8a, then, the bending stems from this local reduction in diameter.

The source of this event is a certain peculiarity within the ion beam that is independent of sample and its properties and has been observed over multiple experiments where the beam over-scans a certain area within its selection. In other words, in this particular case, the thinner part of the pillar experienced a greater fluence than other parts. Although this is not a desirable case as we are interested in homogeneous bending, this is a clear demonstration of controllable localized bending that can be achieved if an ion beam is focused on a much more limited area than the full size of the pillar.

Point-bending events, such as the one shown in Figure 5.8(b) are less pronounced than in copper, i.e. the entirety of the pillar shows a slight bend, and the point-bend angle is not as severe compared to copper, demonstrating the lower influence of localization effects that are not caused by a mixed amorphous-crystalline microstructure. In the case of gold, the point-bending will come as a result of the polycrystallinity of the sample, where certain grain orientations will allow for easier ion propagation than others. Despite this variation in propagation capacity, the mechanism for the development of a stress field through formation

of point defects is the same for the whole pillar, which is why the point-bending effect is weaker than in copper.

Atomic considerations

We can take into consideration the atomic effects during ion collisions to further shed light on the mechanics of IIB across multiple metals. The Kinchin-Pease model, relating the formation of Frenkel pairs (FPs) to the energy of incident particles [4], as well as the model's variations, establishes a primary intrinsic factor that plays a role in particle collisions: the displacement energy of a particular atom.

This term is defined as the energy required to form a single stable interstitial-vacancy pair in a crystalline lattice. Values for this term are readily available in the literature, and many experiments have been performed to correlate theory with empirical information regarding these values [5]. Specifically, agreed displacement energy values for Aluminium and Copper are 16eV and 19eV respectively. The higher displacement value for Cu means that fewer FPs will be formed from a single incident ion than with Al, and thus a smaller stress will be exerted due to point defects provided a constant fluence. Coupled with the higher stiffness of Cu (~120GPa for Cu versus ~70GPa for Al) it is evident that an Al pillar will bend far more readily than its Cu counterpart.

We can use the data we have acquired, as well as that readily available to compare the contributions of intrinsic material properties to the induced effects of ion collisions. The classic Kinchin-Pease model allows us to estimate the number N_d of displacement defects formed from the impact of one ion:

$$N_d = \frac{E}{2E_d} \tag{5.1}$$

where E is the energy available to generate atomic displacements by elastic collisions and E_d is the displacement energy of the target. E_d is mostly measured empirically, and a large amount of literature is available on experiments to measure E_d of various materials [5]. Using displacement energies of 16, 19 and 34eV for Al, Cu and Au respectively, we can estimate the approximate amount of defect pairs formed by a single ionic impact at 30kV:

- Aluminium: 938
- Copper: 789
- Gold: 441

If we estimate the ion emission parameter of the FIB apparatus used at $2.08 \cdot 10^7$ ions per second to achieve an ionic current of 10pA, we can state that approximately $1.64 \cdot 10^{10}$ defects will be formed per second in copper, $1.95 \cdot 10^{10}$ in aluminium and $1.08 \cdot 10^{10}$ in Au. We have demonstrated in the previous chapter that ionic fluence is the singular defining parameter during IIB, in other words, the total number of ions incident on a sample over the course of an entire experiment. As a result, the effective value we are interested in is the point defect fluence, which is simply a linear function of ion fluence.

Due to the complex considerations required for polycrystalline systems, we assume that defects are formed in the same way regardless of target material and that, regardless of material, they contribute in the same way towards a stress state that induces bending. In this manner, in a homogeneous material, it is clear that a particular amount of defects is required to overcome the material's stiffness and induce bending, and that in a material with a lower displacement energy and lower stiffness bending will onset much earlier than in a stiffer one with higher displacement energy. In addition, we do not consider the differences between amorphous and crystalline systems when making our initial estimations.

While impossible in copper due to the tendency towards inhomogeneous bending, we can estimate the force exerted by a single defect in an aluminium pillar. We take a pillar that has shown the first signs of bending at 12s exposure to an ion current of ~10pA (Figure 5.10).

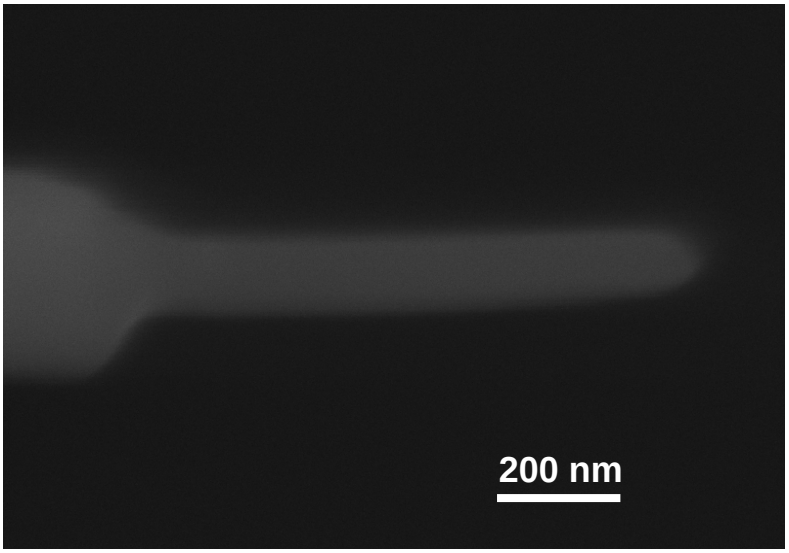

Figure 5.10: Aluminium pillar at bending onset.

Estimating deflection as approximately 34nm, pillar length as 860nm, width as 133nm and the ion penetration depth into Al at 30kV as 50nm, we use the mechanical model presented in chapter 4 to deduce that such a deflection requires a $\sigma_{\max}$ peak of $1.22 \cdot 10^{9} Pa$. At 12 seconds, the amount of defects present in the pillar due to ion beam irradiation is approximately $2.34 \cdot 10^{11}$, or $9.3 \cdot 10^{9}$ at the point of $\sigma_{\max}$. A simple calculation places the stress induced by each individual defect at 0.13 Pa.

We use a computational model to verify our empirical results. Calculations were graciously provided by S. Saane. The Embedded Atom Potential (EAM) method, developed by Daw and Baskes [6] accounts for the behaviour of an atom placed in a defined electron

density. Using the embedding potential for an atom an expression is used to derive the total energy of a metal, and from this a variety of ground-state properties can be obtained such as lattice constant, elastic constants and defect formation energy. For the purpose of our calculations, EAM achieves a sufficiently realistic estimation of metallic bonding.

Using EAM calculations for the simulation of our conditions, i.e. the introduction of a single vacancy into an infinitely large lattice, show a far greater stress induced by the vacancy: $1.85 \cdot 10^5$ Pa. It is clear that the discrepancy comes from the assumption that every single vacancy formed through ionic knock-on contributes to the stress state – rather, we have to consider the mutual compensation of the stress fields created by these point defects, and only the non-compensated fields contribute to the effective stress state. In addition, we must consider that EAM models the pure compressive stress experienced by a lattice with a single vacancy, whereas we base our observations on a bending behaviour, which is far easier to induce than pure compression. Finally, we have to consider that EAM functions through modeling a crystalline metal, whereas our experiment involves a metal that is at least partially amorphous. Assuming linear contribution to $\sigma_{\max}$, the number of defects required to generate the stress for the observed deflection is $6.59 \cdot 10^3$ defects, or $7.9 \cdot 10^{-7}$ of the initial defect total at $\sigma_{\max}$.

We will use this black-box adjustment in our further experiments with the assumption that it will remain valid through the linear dependencies involved in all ion collision events. Further work on understanding the components of the black box and, eventually, achieving full parity between empirical and computational data, is warranted, but beyond the scope of this investigation.

In the previous chapter, we have discussed the shape of the defect profile induced by SRIM and, by association, the shape of the stress profile.

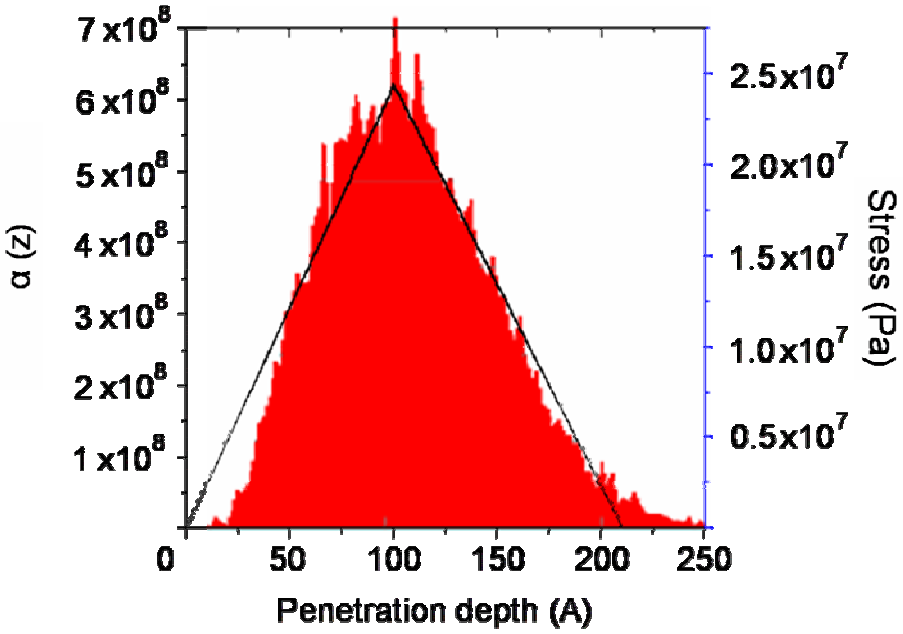

Figure 5.11: Number of defects and resultant stress in Al as a function of ion penetration depth at 12 seconds.

Figure 5.11 shows the ion penetration distribution during IIB as simulated through SRIM. Although simplistic, using this projection we can estimate, by using the linear evaluation presented earlier, the concentration of defects across the profile as well as the distribution of the stress they impart on the pillar at 12 seconds, i.e. the time of bending onset in an Al pillar. By adjusting defect numbers, we can calculate defect concentrations – and, as a result, predict the stress profile - at any time during a pillar's bending period, as shown in Figure 5.12.

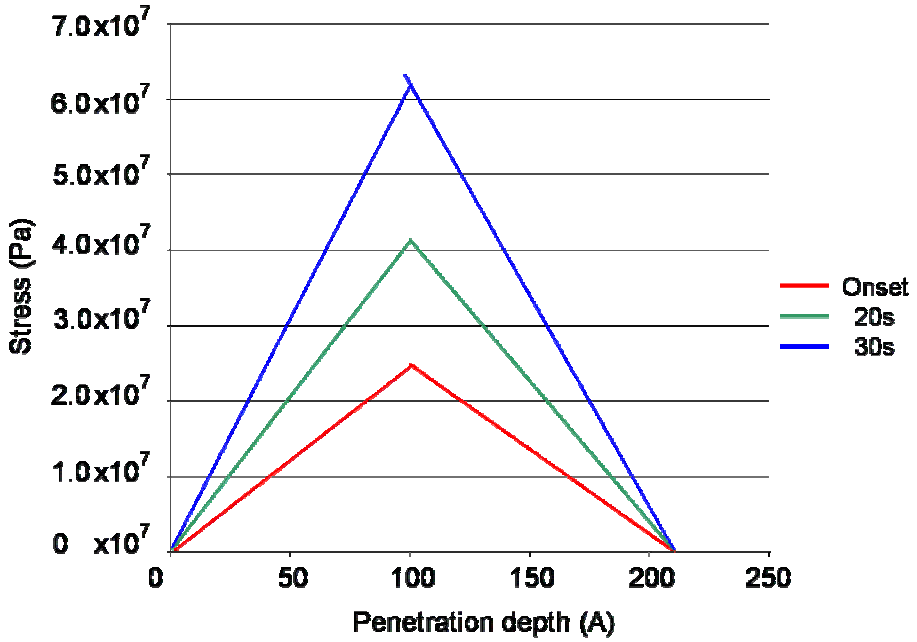

Figure 5.12: Growing stress profile during IIB.

Although simplistic and using a black-box approximation, the model presented here allows for a predictive quantitative analysis of a material, provided that IIB parameters and an EAM potential are known.

5.5 Conclusions

We have determined that ion-beam-induced bending of solid metallic pillars will yield identifiably different responses, mainly divisible into homogeneous and point bending. The former is described as a bend where the radius of curvature remains constant across the entire pillar for the duration of the bend. The latter instead develops a rapidly decreasing radius of curvature at a specific point on the pillar and the rest of the pillar remains mostly straight. The tendency towards one or the other form of bending, assuming that the original material used to make the pillars is otherwise homogeneous, stems from the material's ability to amorphise during ion-beam-assisted production and its subsequent structure when IIB is performed.

We have shown that aluminium displays the capacity for both homogeneous and point-bending. The material tends to amorphise readily during production, and, if the amorphisation is consistent throughout the pillar, the bend will be homogeneous. If significant crystalline regions still remain in a pillar, then bending will occur preferentially at these points due to the strong stress fields generated due to the presence of crystalline point defects.

Copper pillars show a very strong tendency towards point-bending, likely due to a greater ability to retain crystallinity during processing and thus having larger and more frequent crystalline areas amidst amorphous regions.

In the case of gold the point-bending behaviour of the material stems from the crystalline grain microstructure. As certain grain orientations permit a deeper penetration of ions than others, an anisotropic stress profile will form during ion beam exposure. This can lead to stress localization and, therefore, to localized bending. We have, indeed, observed that point-bending in Au is weaker and slower than in Cu.

We have used the Kinchin-Pease model to estimate the number of defects formed in a pillar during IIB. Coupled with the consideration of a defect profile that leads to a bending deflection of the pillar, we were able to estimate the concentration of defects in a pillar after bending onset as well as the shape of the distribution of these defects. As we expect stress to scale linearly with the distribution of defects in the pillar, we can then present a simplified quantitative stress distribution at the surface of a pillar that leads to bending behavior. With this in mind, it becomes possible to evaluate the mechanical behaviour of metallic nanostructures without the use of indentation equipment provided that a pillar of the metal can be made to bend homogeneously.

In this study we have attempted to demonstrate the potency of IIB, coupled with advanced microscopy techniques like TEM, to investigate and characterize the behaviour of a wide variety of metals at the

submicron scale. Although strongly tied to the FIB, both in terms of sample preparation and subsequent testing, the technique shows unparalleled consistency and versatility in its application.

5.6 References

[1] J Biener, A M Hodge, J R Hayes, C A Volkert, L A Zepeda-Ruiz, A V Hamza, F F Abraham, *Nano Letters* 2006 Vol. 6, No. 10 2379-2382

[2] M-J de Haas, Grain boundary phenomena and failure of aluminium alloys, University of Groningen, 2002

[3] L P H Jeurgens, W G Sloof, F D Tichelaar, C G Borsboom, E J Mittemeijer, Applied Surface Science, Volumes 144–145, April 1999, Pages 11-15

[4] G H Kinchin, R S Pease 1955 Rep. Prog. Phys. 18 1

[5] P Jung, Phys. Rev. B, 23, 664 (1981)

[6] M S Daw, M.I. Baskes, Phys. Rev. B, 29, 6443 (1984)

Chapter 6

ION-BEAM INDUCED BENDING OF NANOPOROUS METALLIC PILLARS

We have investigated the behaviour of nanoporous metallic pillars under ion-beam-induced bending (IIB) and compared it to that of solid pillars of similar dimensions. We observe consistent homogeneous bending in nanoporous pillars and we attribute this predominant behaviour to a homogenizing effect of porosity. We examine the bending rates of Au and Cu nanoporous pillars and determine that pillars bend under a constant rate under IIB with the exception of cases where a pillar bends long enough that its diameter decreases significantly due to ion milling. In such a case, bending rate increases as diameter decreases. Using values for the formation of point defects in Cu and Au, as well as that of the contribution of a single point defect to lattice stress, we are able to make quantitative predictions about the stiffness modulus of Cu and Au nanoporous pillars.

6.1 Introduction

In the previous chapter we have implemented IIB on solid nanopillar structures. There, we found that IIB will yield identifiably different responses when implemented on a solid structure that we have termed homogeneous bending and point-bending. The former describes a condition where a pillar maintains a continuous bend throughout the experiment and the latter instead involves a localized bend where the pillar will preferentially bend at a single point, with the rest of the pillar

remaining mostly straight. This point-bending occurs due to crystalline inhomogeneities within a pillar's structure present at the grain level. Conversely, homogeneous bending will occur if a pillar is microstructurally homogeneous. As point-bending is an unpredictable, plastic effect, it is detrimental to any experimentation done using IIB: the ideal sample for IIB is homogeneous that bends linearly and predictably. Indeed, it was only possible to form a quantitative analysis using IIB on aluminium, as it was the only material that did not point-bend.

This observation brings us to a broader consideration of the great differences reported between solid and nanoporous systems of the same material [1-4, 6]. In the context of our investigation, we have repeatedly mentioned that the properties of nanoporous metals vary greatly from their solid bulk counterparts, to the point that classical scaling laws have to be adjusted to predict their behaviors [3]. A question arises: how different will a solid gold nanopillar of diameter 200 nanometres be from a gold nanopillar with the same diameter, but with a porous microstructure with pore-ligament sizes of 20-30 nanometres? In chapters 4 and 5 we have demonstrated that IIB has the potential to answer this question.

In this chapter we perform ion-beam-induced bending experiments on nanoporous gold, copper and a copper-nickel alloy. The purpose of this investigation is twofold: first, by investigating gold and copper we are able to make a comparative analysis between the behaviors of these metals both in solid and nanoporous form by taking into account results from chapter 5 and, second, by investigating materials with a markedly different microstructure from the typical solid crystalline we broaden the scope of knowledge of the effects of IIB as a mechanical characterization tool.

6.2 Experimental method

Disordered nanoporous Gold, Copper and Copper-Nickel alloy were prepared through electrochemical dealloying. AuAg ingots of composition $Au_{0.35}Agn_{0.65}$ at.% were prepared by arc-melting *6n* Au and Ag. Ingots were sealed in quartz tubes and homogenized at 1223 K over several days. Dealloying was carried out using a standard three-electrode Potentiostat electrochemical cell (*µAutolab type III/ Fra2- Eco Chimie)*, with the AuAg foil at the working electrode, platinum mesh at the counter electrode and Ag-AgCl as a reference electrode. Dealloying was performed in 1M HNO_3 at ~ 600mV over several days until dealloying current was negligible.

CuMn ingots of $Cu_{0.3}Mn_{0.7}$ at.% were prepared by arc-melting *6n* Cu and Mn. Afterwards the ingots were vacuum-sealed inside quartz tubes and homogenized over several days at 1173K. Ingots were then rapidly quenched to prevent formation of secondary phase in an otherwise CuMn solid solution. Dealloying was carried out using a standard three-electrode electrochemical cell (*µAutolab type III/ Fra2- Eco Chimie)*, with the CuMn alloy at the working electrode, platinum mesh at the counter electrode and Ag-AgCl as a reference electrode. Dealloying was performed in 0.05M HCl at -550mV for up to 4 hours until dealloying current was negligible.

Ingots of $Ni_{0.25}Cu_{0.25}Mn_{0.5}$ were prepared by arc-melting high-purity Ni, Cu and Mn. The ingots were homogenized at 1173K for 24 hours and then rapidly quenched in water. Dealloying was carried out using the same apparatus as above in 0.1M $(NH_4)SO_4$ at -0.65V vs. SCE for 1 hour [5].

Porous nanopillars were cut from prepared material. Non-tapering of the nanopillar sides was achieved by using a custom FIB milling technique. Common milling techniques introduce tapering, during which the cross-sectional area across the length gradually becomes thicker towards its base. As we are interested in the bending behavior

of the pillar across its entire length, we wish to ensure a uniform diameter. Our procedure ensures such geometry. A set of fully taper-free pillars with diameter ~250nm was fabricated by means of a dual beam FIB/SEM microscope (Lyra, Tescan, CZ). The aspect ratio of the pillars was initially chosen to be in the range of 2-3 for ease of production and further mechanical stability.

Pillar deformation was induced using a dual beam FIB/SEM microscope (Lyra, Tescan, CZ). Each pillar was aligned perpendicular to the beam to fully expose one of its faces. This leaves the opposing face in the ion beam's shadow. TEM images were acquired using a JEOL 4000 EX/II Transmission Electron Microscope.

6.3 Results

Bending behaviors

IIB behaviour of nanoporous Au pillars showed a tendency towards homogeneous bending, i.e. where a bend is continuous along the entirety of the pillar as opposed to being localized to a single point as in the case of point-bending (Figure 6.1).

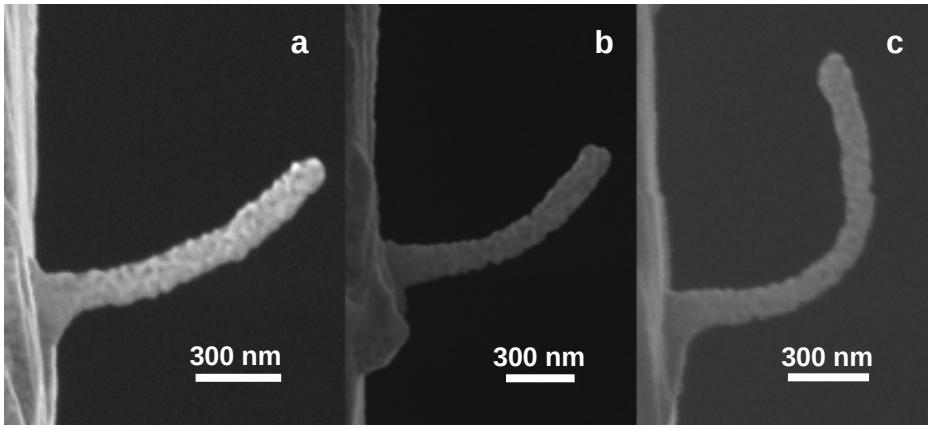

Figure 6.1: Homogeneous bending in different pillars in nanoporous Au.

IIB performed on solid Au pillars showed a possibility of point-bending, where the pillar would deform around a single point, developing a rapidly-decreasing radius of curvature there. This behaviour was never observed in nanoporous Au pillars despite preparation and bending method remaining otherwise the same. For comparison, IIB was performed on nanoporous Cu pillars. Solid Cu was shown to have a severe tendency towards point-bending, such that homogeneous bending was never observed during IIB of solid Cu pillars.

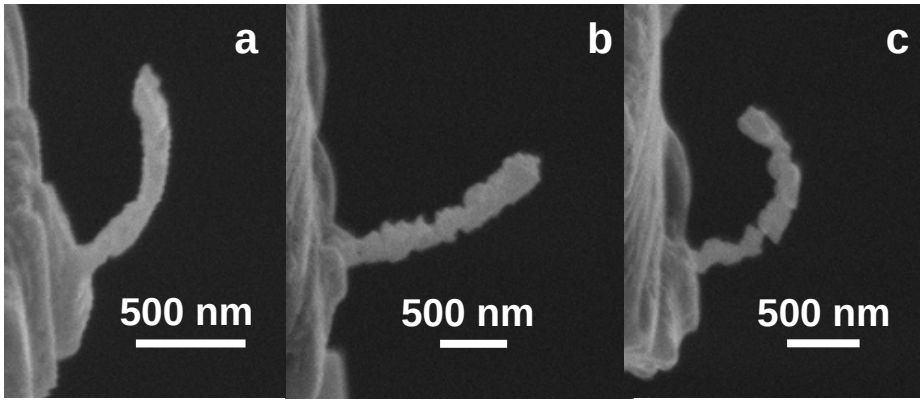

Figure 6.2: Homogeneous bending in different pillars in nanoporous Cu.

As seen in Figure 6.2, nanoporous Cu pillars bend readily and homogeneously. We note that, despite visible variations in thickness along pillar 2c, the pillar still assumes a constant radius of curvature along its length. Localized reduction in diameter can be observed in most IIB experiments. This is caused by either errors in ion beam scanning or due to microstructural peculiarities within the pillar itself. Specifically, the former refers to an effect sometimes observed during FIB work where the beam overscans a particular area within a selection by dwelling at the start of a line scan.

This leads to an overmilling in the dwell region, which leads to the pillar becoming thinner in the affected area than everywhere else. This effect is specific to our apparatus, and is not fully controllable or

reproducible. However, we have successfully compensated for this extra dwell time by ensuring that the dwell region lies outside of the pillar, deeper beyond the pillar's base.

The latter comes as a result of flaws present in the pillar after dealloying, where voids or unusually large or small ligaments might form. Although preferential thinning occurs in all pillars during IIB, the same can be seen to occur in both nanoporous Au and Cu pillars where, despite it, bending is homogeneous, and thus can be concluded to not be a significant factor affecting bending behaviour.

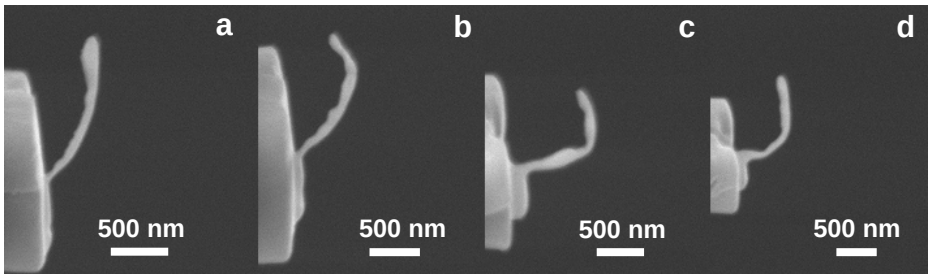

Figure 6.3: Homogeneous bending (a) and various forms of point-bending (b, c, d) in nanoporous CuNi alloy.

As illustrated in Figure 6.3, pillars from nanoporous Cu-Ni show bending behaviors unlike those of Au and Cu. Nanoporous CuNi alloy shows a strong tendency towards point-bending. While in some cases point-bending occurs around areas where localized reduction of diameter has occurred, this is not universally true. For example, in pillar 3b the most prominent point-bend occurs at an otherwise thick region. Conversely, localized reduction of diameter does not necessarily mean that a point-bend will occur at that region.

Bending rates

The homogeneous bending behaviour of nanoporous Au and Cu pillars allows us to draw conclusions regarding the intrinsic material properties' influence on IIB response. All nanoporous pillars made from Au and Cu followed a specific rate of bending depending on material.

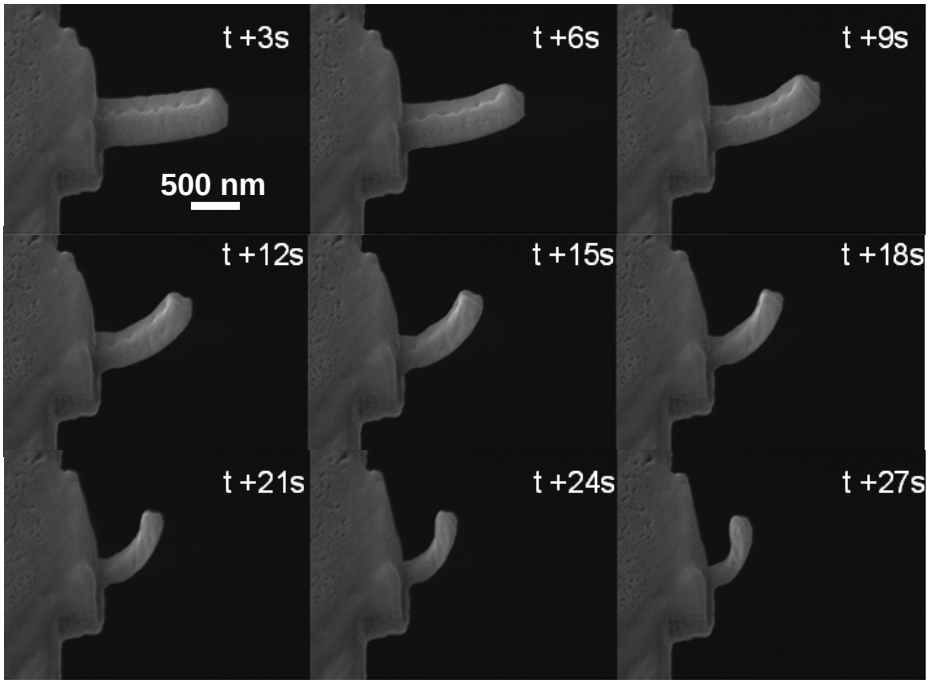

Figure 6.4: Bending rate in a nanoporous Au pillar.

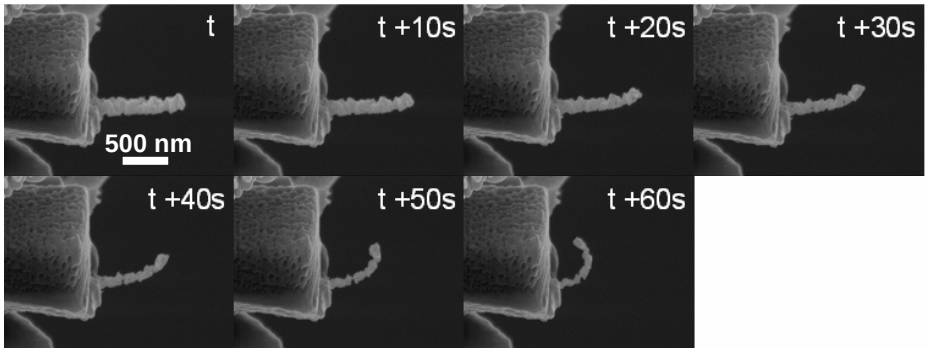

Figure 6.5: Bending rates in a nanoporous Cu pillar. Ion current is the same as for nanoporous Au pillars.

In Figure 6.4 we see that once bending has begun, it proceeds continuously until the ion beam is shut off. With the ion beam off, no recovery is observed, and the pillar remains in its deformed position until the beam is switched back on and the pillar continues to deform. If any relaxation occurred at all, it is too small to be observable. While a certain degree of localized diameter reduction through overmilling is observed, no tendency towards point-bending is observed.

In Figure 6.5 bending is homogeneous, but the rate is clearly not constant – bending is much faster in the last 30 seconds of the experiment. Inhomogeneities in diameter are even more stark than in Au, but, regardless, bending is homogeneous. It should be noted that no bending is observed in a pillar until a certain critical diameter is reached. As such, in this experiment bending rates were only recorded once bending is first observed in a pillar. Due to this certain error will be present due to bending events being judged by eye. In addition, error will be present due to the difference in angles of incidence of the ion and electron beams – in other words, Figures 6.4 and 6.5 are observing a projection of the pillar 55 degrees away from the perpendicular.

IIB occurring in Figures 6.4 and 6.5 was carried out in the same conditions at a constant ion current of 10pA. It is clear that the more compliant Au pillar bends far more readily than the Cu pillar.

In Chapter 5, we were unable to make quantitative comparisons between the bending rates of different species of metallic pillar – and, thus, their mechanical properties on the submicron scale - due to the tendency towards point-bending of both Cu and Au solid pillars. As a defect-dominated mode of plastic deformation, point-bending is challenging to evaluate in the scope of this investigation. Here, however, we see consistent homogeneous bending in both copper and gold pillars, and, as such, we can make stronger comparisons.

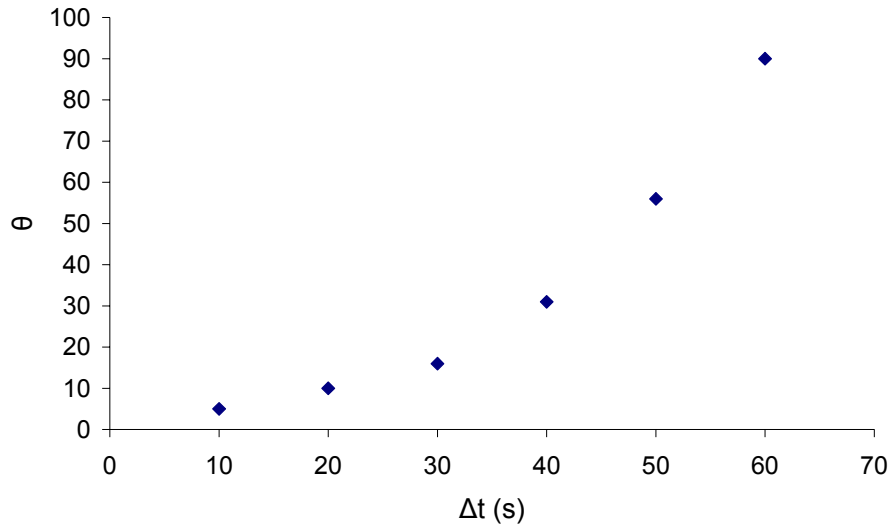

Figure 6.6: (Nanoporous copper) During homogeneous bending, rate of displacement increase at any point on the pillar follows a power law growth.

For rate-based calculations we choose a specific distance from a pillar's base and measure its angular deflection θ away from its neutral position, i.e. prior to IIB. (Figure 6.6) Measurements are taken every constant time interval Δt to yield a deflection progression. The time prior to bending onset falls outside of our considerations, as this period is when the pillar is too thick for the bilayer effect induced by the defect gradient caused by the presence of point defects, and we only start measurement after we observe bending onset at time t.

Upon reaching a critical diameter, the pillar starts to bend. The factors affecting the bending rate at this point will be the compressive stress induced by the point defects present in the pillar surface and the pillar's stiffness. As number of point defects increases linearly, so should the bending itself proceed at a constant rate.

In the case of copper, however, the pillar grows steadily thinner throughout the bending period due to the milling effect of the ion beam. If we can determine the rate of milling, we can examine it and compare it to the milling rate.

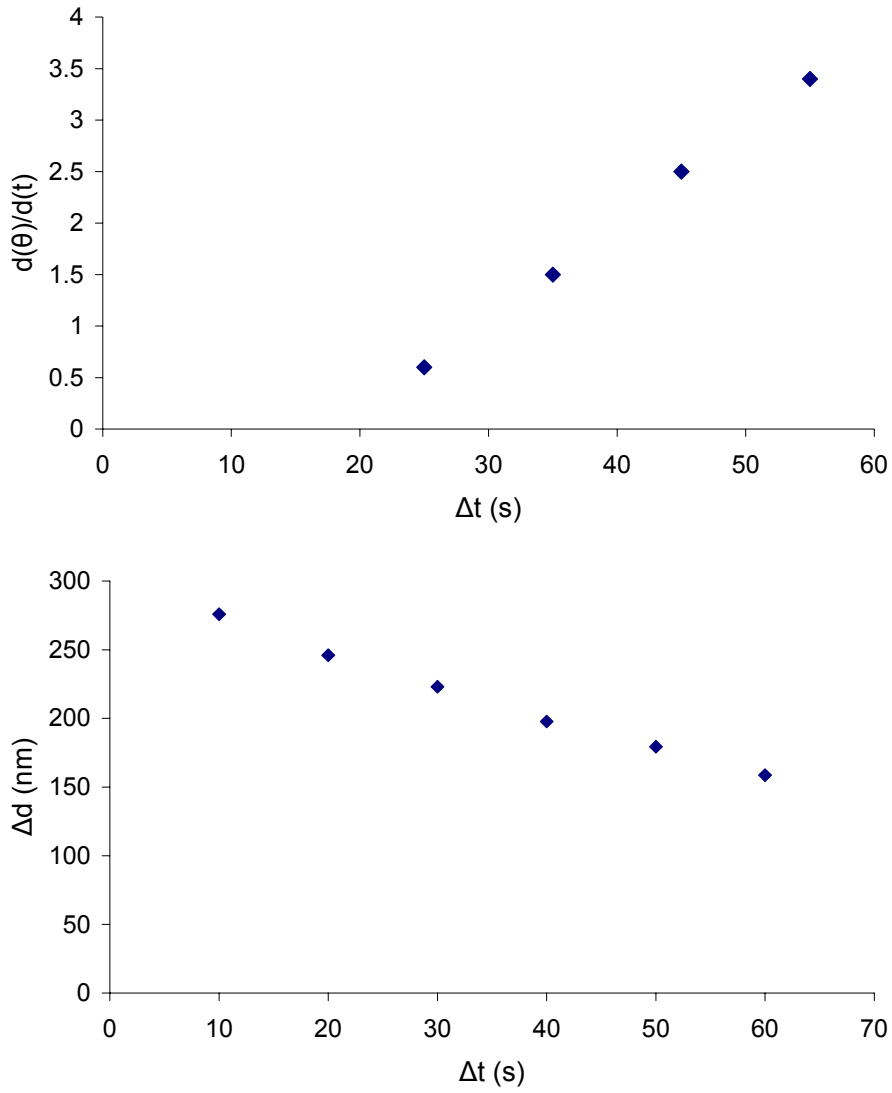

Figure 6.7: (Nanoporous copper) Linear dependencies of bending rate and diameter to time past bending onset.

We can see from the linear relationships in Figure 6.7 that the speed of bending of a copper pillar is influenced by the pillar's diameter. The bending behaviour of gold is different, however, to that of copper.

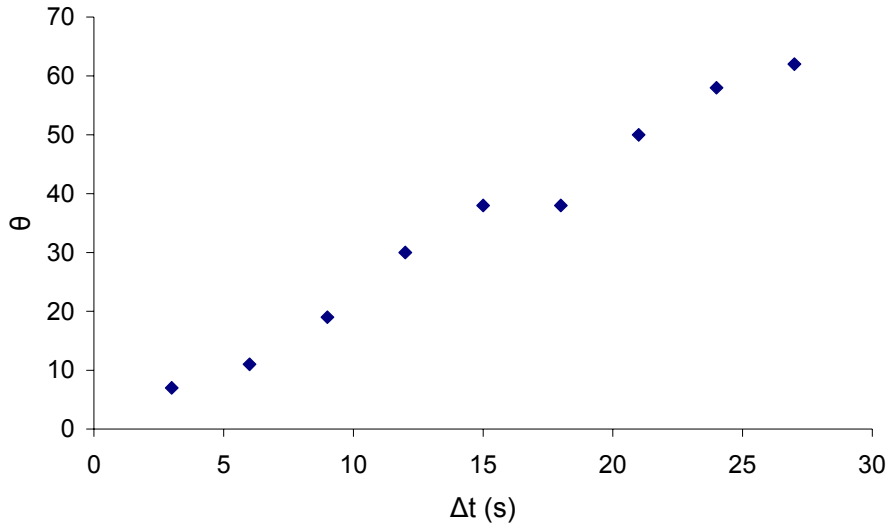

Figure 6.8: (Nanoporous gold) Unlike in nanoporous Copper, bending in a nanoporous Gold pillar is linear regardless of changes in pillar diameter.

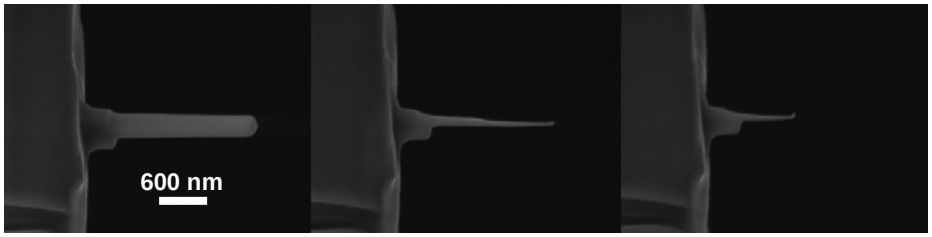

Figure 6.9: A solid Au pillar exhibits very little bending behaviour.

Figure 6.8 shows a linear deformation progression that reaches maximum deflection far quicker than copper does.

We can attribute this to the effect of Au's compliance: the stiffness of Au is low enough that the pillar's bending onset happens almost immediately and the pillar proceeds to bend quickly. Effectively, the pillar completes bending before its diameter is meaningfully reduced by ion beam milling.

When we attempt to compare the behaviour of porous Au to that of a solid Au pillar we are faced with a peculiarity: if the pillar does not point-bend due to some localized defect, it does not bend at all, as shown in Figure 6.9.

This phenomenon stems from the presence of a critical diameter before a pillar starts to bend: such a diameter must be so low for Au that the pillar is milled away by the ion beam completely as it approaches the required thickness. Indeed, we can see a small bend at the tip of the pillar in the rightmost image. In Chapter 5, we observed the point-bending of solid copper pillar that was attributed to crystalline-amorphous inhomogeneities within each pillar. We expect that, were a fully homogeneous solid Cu pillar subjected to IIB, a similar phenomenon to that seen in Figure 6.6 would be observed in it as well, as ion penetration depth is similar for both metals: SRIM shows 44 and 47 Angstroms' penetration for Au and Cu respectively.

6.4 Discussion

Bending behaviour

It is critical to note the differences in bending behaviour between solid and porous pillars. In Chapter 5 we have observed both homogeneous and point-bending in solid aluminium pillars, and point-bending only in solid copper and solid gold pillars. We have discussed that for a pillar to bend homogeneously, it must itself be homogeneous and, conversely, any inhomogeneities within a pillar will lead to point-bending and the exact mechanics of this can vary, leading to variations within point-bending behaviour itself.

We have observed that, during processing and experimentation, a solid aluminium pillar is likely to undergo a certain degree of amorphisation. Those pillars that have amorphised fully would bend homogeneously,

while partial amorphisation where crystalline regions would still be present would lead to preferential bending in the crystalline regions. In gold, where amorphisation was low, point-bending instead came as a result of variation in crystal orientation, presenting avenues of preferential propagation of incident ions, leading to variations within the resultant stress profile. In the cases of nanoporous Au and Cu, however, bending is clearly homogeneous, with any localization effects minor enough to be negligible.

There is no basis to assume that the nanoporous pillars in question do not have any microstructural inhomogeneities, as polycrystallinity is retained post-dealloying in the fabrication of a nanoporous metal. We then have to attribute this change in bending mode to the induction of porosity changing the dominant microstructural feature in a pillar. Specifically, in a solid, the crystalline microstructure and any inhomogeneities that resulted from it was what determined whether the pillar would bend homogeneously or not. With the induction of nanoporousity it is the pore-ligament microstructure that determines a pillar's bending behaviour.

Indentation experiments on nanoporous gold have shown that deformation is confined to the contact area with pore structure adjacent being undisturbed, indicating the absence of long-range stress fields [3]. In other words, ligaments not immediately adjacent to one another do not "see" each other. Due to this, effects of large-grain polycrystallinity as seen in solid gold or amorphous-crystalline microstructure mixtures as seen in solid copper, are effectively negated, and the material can be treated as a polycrystalline material with grain size equal to the diameter of a single ligament, approximately 30nm.

Considering the random orientation of ligaments and the total surface area of a pillar exposed to ion fluence (several hundred thousand nm^2) compared to the size of a single ligament which serves as the material's defining microstructural feature, a nanoporous pillar can be considered fully homogeneous.

The behaviour of nanoporous CuNi is markedly different from that of nanoporous Au and Cu by showing a strong tendency towards point-bending. The chief difference between nanoporous CuNi and its Au and Cu counterparts is the pore size and distribution: pores are under 10nm in diameter and are non-interconnected. In this manner, the homogenizing effect of porosity on the material is significantly weaker – the emphasis of grains becomes more important, and localized stress fields are no longer broken up by voids and thus become longer-ranged.

Bending rates

Nanoporous Au and Cu pillars have characteristically different homogeneous bending rates and behaviors. As seen in the results, Au bends at a constant rate throughout IIB, while Cu undergoes accelerated bending towards the end of an IIB experiment. The origin of this discrepancy comes from the milling effect of the FIB. Of course, one should always keep in mind that IIB is a destructive technique, and that the longer an experiment proceeds, the greater the fundamental change that will be induced in the material under investigation.

In this case, whether a pillar bends at a constant or at an increasing rate depends on the competition between base bending rate and the rate of milling. The latter is significant as a thinner pillar has a greater volume ratio of defect -rich compressive region to ion-unaffected neutral region. In other words, the bilayer effect – and, thus, the resultant bending response – is stronger in a thinner pillar. The base bending rate in this consideration, provided that bending is homogeneous, is influenced only by the material stiffness and the rate of formation of point defects during ion beam exposure.

The milling rate is only dependent on bond strength and the ability of an ion to knock a surface atom completely clear of the target. Barring any peculiarities that might be unique to a sample, milling rates between Au and Cu will not vary significantly. This leads us to the

conclusion that a soft material like Au will undergo bending faster than ion milling will lead to a meaningful reduction in diameter. On the other hand, Cu is significantly stiffer than Au and will thus bend much more slowly, allowing diameter reduction to have an influence on bending rate. The conclusion emerges that all deflection-based calculations have to be performed on pillars at early stages of bending onset, prior to rate-dependent effects becoming influential.

It is clear that a baseline comparison is required to fully evaluate the mechanical differences between a solid and porous pillar. Due to the challenges inherent in acquiring reliable results from experiments, we turn to atomistic simulation. We require an intrinsic material property that is true for both porous and solid pillars, and a good candidate is the lattice stress caused by the presence of a single point defect.

In our previous work we have used the embedded atom potential (EAM) simulation, developed by Daw and Baskes, to calculate this lattice stress. EAM uses the embedding potential for an atom to derive the total energy for a metal, which allows for a variety of ground-state properties to be obtained, amongst them lattice constant and point defect formation energy.

We have used embedded atom potential (EAM) simulations to generate such a value for Al in Chapter 5, and the same method can be used for Cu and Au. In addition, we have earlier made a comparison between single-point defect lattice stresses determined empirically through back-calculation of experimental values and stresses determined through EAM, and have found a major difference between the resultant values. The discrepancy comes from a limited consideration of all factors present, such as stress field compensation between several point defects. However, we assume that, when considered across the entire defect-rich volume, defects contribute to stress linearly.

Using this assumption, we have formulated a “black-box” adjustment, where, if the EAM value for lattice stress of a single defect in a

particular metal is used, only a small fraction of the total number of point defects contribute to the overall stress state. This adjustment will function for as long as the assumptions that all relationships between defect formation and total stress state hold, and that defects are formed in the same way in all metals considered. The former we have determined to be material-independent and the latter holds as Al, Cu and Au are all FCC metals, meaning that effects of ion collisions will approximately be the same. With this known, we can make quantitative prediction about mechanical properties of our pillars.

To do so, we use the displacement energy term E_d of a metal in the Kinchin-Pease equation that relates accelerated ion energy to amount of point defects formed through E_d.

$$N_d = \frac{E}{2E_d} \tag{6.1}$$

If ion emission parameters are known, we can calculate the amount of point defects formed per second and, thus, the overall ion fluence and defect count for the entirety of the exposure time. We then apply the black-box adjustment to make our data compatible with EAM calculations and use these calculations to determine the aggregate lattice stress that is induced by the point-defects. Finally, we measure the displacement strain from SEM images and, using classical beam-bending considerations, we determine a value for Young's Modulus.

We take a nanoporous Au pillar under IIB for 12 seconds (Figure 6.4). Assuming a constant ion current of 10pA and constant ion energy of 30kV, we can estimate the formation of $1.08 \cdot 10^{10}$ defects per second in Au. At 12 seconds this becomes $1.3 \cdot 10^{11}$ defects total. As determined by the black-box adjustment presented in our work with aluminium, of the total number of defects, $9.2 \cdot 10^{4}$ will contribute to a stress field, of these, the number of defects at $\sigma_{\max}$ (d/2 where d is 20nm) is $9.2 \cdot 10^{3}$. According to EAM, a single point defect induces a stress of

$6.25 \cdot 10^5$ Pa. Assuming a linear contribution of point defects to stress, the stress at σ_{max} is 5.8 GPa.

At 12 seconds the dimensions of the nanoporous Au pillar are as follows: $\delta(x)$ is 657nm, w is 434nm, x is 1220nm (see Figure 6.4). Ion penetration depth d into Au is 20nm. Using the beam-bending model presented in chapter 4, this results in a modulus value of 2GPa. In a material with 50% porosity, 50% of the surface will consist of voids, with surface beginning a ligament's depth beneath the surface, extending the potential penetration depth to 50nm and thus an alternative resultant modulus value of 4.6GPa. This is very close to the experimentally-determined value of ~11 GPa seen in literature [3]. The slight discrepancy in values comes from multiple approximations in the IIB model, chiefly the exact count of incident ions and point defects formed, as well as the measurement of deflection angle as leading into a strain value. In addition, at 12 seconds bending is strong enough where plastic effects have to be taken into consideration within the pillar's microstructure, i.e. unit cell buckling or coarsening of ligaments. With this in mind, the result is realistic enough to validate the black-box adjustment that we have proposed.

For comparison, we take a nanoporous Cu pillar under IIB for 40 seconds (Figure 6.5). Assuming a constant ion current of 10pA and constant ion energy, we can estimate the formation of $1.64 \cdot 10^{10}$ defects per second in copper. At 40 seconds this becomes $6.6 \cdot 10^{11}$ defects total. Following the black-box adjustment, only $4.6 \cdot 10^5$ defects will contribute to the compressive stress field, with $2.3 \cdot 10^4$ at σ_{max} (d is 20nm). According to EAM, a single point defect induces a stress of $3.45 \cdot 10^5$ Pa. Assuming a linear contribution of point defects to stress, the total stress at σ_{max} becomes 7.9GPa.

At 40 seconds the dimensions of the nanoporous Cu pillar are as follows: $\delta(x)$ is 255nm, w is 106nm, x is 642nm (see Figure 6.5). Ion

penetration depth d into Cu is 20nm. Using the beam-bending model presented in chapter 4, this results in a modulus value of 27GPa.

This is significantly smaller than the known literature value for solid copper, and clearly corresponds with the far higher compliance observed in nanoporous copper pillars. As there is a lack of literature data on the mechanical characteristics of nanoporous copper, we can use scaling laws to determine a predicted modulus value for nanoporous copper. It has been demonstrated that scaling law calculations are capable of making accurate predictions in this context [3]. Nanoporous Cu is an open-cell foam, so its Young's Modulus E can be described as

$$E = C_2 E_s (\rho_{np} / \rho_s)^n \qquad (6.2)$$

Where E_s is the modulus of solid Cu and (ρ_{np} / ρ_s) is the relative density of the foam [3]. C and n are proportionality and density constants respectively that describe cell geometry and elastic cell deformation, and experimental data obtained from open-cell foam materials has shown that the constants can usually be well-fitted by C_2 =1 and $n = 2$.

Assuming that our nanoporous Cu has a relative density of 30% and using the modulus of Cu at 110-128GPa, the scaling law predicts a modulus value of 9.9-11.52 GPa. While in the same magnitude as the IIB prediction, the discrepancy is non-negligible. This variation likely stems from the effects that we have described that occur due to prolonged exposure to the ion beam, for example pore closure and ligament coarsening that might lead to reduced porosity, and the power-law growth of the displacement observed in the pillar.

As with Au, we can clearly see that a nanoporous metal – with interconnected pore microstructure – is far more compliant than its solid counterpart. This effect stems from the great difference in free

surface – the nanoporous metal has vastly more free surface that permits easy deformation until such a point where deformation would have to proceed through unit cell buckling and later solid-like compression. In this experiment, cell buckling behaviour was not observed, so we can conclude that the nanoporous Au and Cu investigated have a far higher yield to fracture than their solid counterparts.

With the black-box adjustment validated, a comparative baseline exists for the use of IIB as a mechanical characterization tool. With this investigation, the behaviour of a variety of FCC metals has been compared and we can confidently say that their response to IIB is predictable and quantifiable. Currently the issue of point-bending exists, which limits the applicability of IIB if the microstructure of a particular submicron-sized feature cannot be controlled, but the problem is only present in solid metals. IIB for the characterization of nanoporous metals shows a lot of potential if used in concert with EAM.

6.5 Conclusions

We have observed a strong difference in bending behaviour between a solid and a porous pillar of the same material. Where solid pillars of Cu and Au tend to show point-bending, no such behaviour is seen in porous pillars. Instead, porous Cu and Au pillars bend homogeneously with predictable bending rates.

This phenomenon is attributed to a homogenizing effect of porosity: due to pore-ligament being the dominating microstructure that is consistent and homogeneous throughout the pillar, the contribution of any inhomogeneities in the source material is lessened. Considering the presence of point-bending in a CuNi alloy with a very small pore size we have concluded that there exists an optimal pore-ligament size where such a microstructure dominates and contributes its homogenizing effect. The exact size range where the pore-ligament

microstructure dominates is beyond the scope of this particular investigation and is still open for discussion.

We have examined the homogeneous bending behaviour of nanoporous Cu and Au pillars. We have observed that Cu pillars underwent bending at a constantly increasing rate, and have attributed this to the linear reduction of the pillar's diameter during IIB as the ion beam mills away the exposed pillar surface. Such behaviour was not observed in Au, where bending rate was constant. This is likely due to the extremely low stiffness of the pillar – the pillar bends faster than the diameter reduction effect of the ion beam.

One of the strongest aspects of IIB is its potential as a contact-free method to evaluate the mechanical properties of a material provided that a comparative baseline is available. We have used our experiments with Al from our previous work, along with embedded atom potential simulations to acquire values for the compressive stress induced by a single point defect in a crystalline lattice, as well as the point defect formation behaviour due to ion beam treatment for a variety of metals.

With these values known, we become able to evaluate such properties as the Young's modulus for our nanoporous metallic pillars, which are complex composite materials in their own right, without resorting to physical indentation or tension experiments.

6.6 References

[1] J. Biener, A. M. Hodge, J. R. Hayes, C. A. Volkert, L. A. Zepeda-Ruiz, A. V. Hamza, F. F. Abraham, *Nano Letters* 2006 Vol. 6, No. 10 2379-2382

[2] R Li, K Sieradzki, Au. Phys. Rev. Lett. 68, 1168-1171 (1992)

[3] J Biener, A M Hodge, A V Hamza, L M Hsiung, J H Satcher, J. Appl. Phys. 97, 024301 (2005)

[4] C A Volkert, E T Lilleodden, D Kramer, J Weissmuller, Appl. Phys. Lett. 89 061920 (2006)

[5] M Hakamada, M Mabuchi, Journal of Alloys and Compounds 485 (2009) 583-587

[6] L J Gibson, M F Ashby, Cellular Solids: Structure and Properties, 2nd ed. (Cambridge University Press, Cambridge, 1997)

Chapter 7

A COMPARATIVE STUDY: ION-BEAM INDUCED BENDING OF SOLID AND ORDERED NICKEL

We investigated bulk solid and nanoporous nickel pillars with inverse gyroid morphology using Ion-Beam-Induced Bending (IIB). Solid nickel pillars exhibited preferential point-bending, whereas porous pillars bent homogeneously. Using the Kinchin-Pease model and the information acquired from embedded atom potential (EAM) modeling we were able to apply a mechanical model of beam bending to estimate the Young's modulus of nanoporous nickel pillars with inverse gyroid morphology without the use of contact-based pico- or nano-indentation systems. We observed an effective modulus of 2.4GPa, which is far lower than the modulus of solid nickel - 200GPa. We attribute this large difference in modulus to the weaker porous microstructure and to the presence of anisotropic preferential bending directions that facilitate far easier bending than in an isotropic disordered nanoporous microstructure.

7.1 Introduction

Disordered nanoporous metals have been seen to show many interesting mechanical properties, amongst them ductility under compressive stress and the capacity to approach the intrinsic yield strength of gold [1]. In the previous chapter, we have observed that

nanoporous gold and copper produced by dealloying, regardless of their initial crystal structure or any internal defects, behave as isotropic materials. This is due to a homogenization effect caused by the lack of long-range stress fields being able to form in the material. In other words, ligaments not adjacent to one another do not "see" each other when it comes to the propagation of stress fields.

Modern methods allow for the fabrication of ordered porous metals, where repeating unit cells of pores and ligaments can be clearly identified and form crystalline networks [2-4]. At the submicron scale, where shape and form factors become increasingly important, the degree of ordering of a nanoporous structure can have a strong influence on the structure's material properties. Where porosity leads to a homogenization of the material, by ordering the porosity the material is once again made anisotropic, allowing for the emergence of preferred deformation directions that would lead to variation in behaviour depending on stress orientation.

We have demonstrated the reproducibility and degree of control that IIB offers as a characterization technique on solid and disordered nanoporous metals, giving us a comparative baseline with which we can make judgments on other, more complex metals. As such, the behaviour of solid and ordered porous systems can be correlated to the behaviour of disordered porous systems. However, characterization by means of IIB is still in its infancy. Previous experiments have yielded results that closely correlated to literature values, empirical and computational comparisons are still required such that the experimental method can be calibrated to a wide variety of materials.

In this chapter we compare the bending behaviour of solid and ordered nanoporous nickel pillars under an ion beam. By using known values for radiation damage in nickel, we are able to make conclusions about the differences between the two types of pillars investigated.

7.2 Experimental method

Ordered nanoporous nickel

Nanoporous nickel foams with an ordered gyroid morphology were produced using electroless plating of a diblock copolymer template. Supramolecular complex films were formed by dissolving diblock copolymer films of polystyrene and poly(4-vinyl-pyridine) in chloroform with 3-Pentadecylphynol. The resulting solution was allowed to set in a Petri dish in a saturated chloroform atmosphere. The chloroform was allowed to evaporate over several days and, subsequently, the resultant product was vacuum-dried and annealed in nitrogen atmosphere. A more detailed procedure is available in the thesis by I. Vukovic [5].

Once the diblock copolymer template was formed a three-stage process was followed to form a nanoporous metal network. The template is soaked in a stirred $SnCl_2$ and HCl solution to adsorb Sn^{2+} ions onto the template surface. Afterwards, the template is moved to a $PdCl_2$ and HCl solution to facilitate the $Sn^{2+} + Pd^{2+} \rightarrow Sn^{4+} + Pd^{0}$ reaction. The atomic palladium is used as a catalyst for the plating reaction, which is carried out in a solution that contains:

- $NiCl_2$ x $6H_2O$
- NaH_2PO_2 x H_2O
- $HOOCCH_2OH$
- 1M NaOH (used to adjust pH to ≈4.5)

Plating occurred for 30 minutes in an agitated solution at 95ºC. The template is then removed through furnace heating at 350ºC overnight.

Preparation of submicron-scale pillars

Porous nanopillars were cut from prepared material. Non-tapering of the nanopillar sides was achieved by using a custom FIB milling technique. Common milling techniques introduce tapering, during which the cross-sectional area across the length gradually becomes thicker towards its base. As we are interested in the bending behavior of the pillar across its entire length, we wish to ensure a uniform pillar's diameter. Our procedure ensures such a taper-free pillar's geometry. A set of fully taper-free pillars with diameter 500 nm was fabricated by means of a dual beam FIB/SEM microscope (Lyra, Tescan, CZ). The aspect ratio of the pillars was initially chosen to be in the range of 2-3.

Pillar deformation was induced using a dual beam FIB/SEM microscope (Lyra, Tescan, CZ). Each pillar was aligned perpendicular to the beam to fully expose one of its faces. This leaves the opposing face in the ion beam's shadow.

7.3 Results

Solid nickel pillars

In all experiments, solid nickel pillars experienced point-bending as a response to IIB. An extremely high aspect ratio was developed as a result of ion milling. No homogeneous bending was observed in any experiments, showing a clear similarity to the behaviour of other crystalline metals investigated in this manner - Cu and Au. Point-bending was observed both at the base of the pillar, which has been noted to be characteristic of a fault in the ion beam itself, and at arbitrary points along the length of the pillar, which is more characteristic of a typical point-bend caused by crystalline inhomogeneity within the pillar itself.

Ordered nanoporous nickel pillars

Unlike their solid counterparts, nanoporous nickel pillars showed a much more homogeneous bend. As seen in previous experiments with Cu and Au, this behaviour is characteristic of the homogenization effect that porosity induces in an anisotropic crystalline material. Pitting and the formation of voids in the exposed surface have been observed during experiments.

At time *t* where the pillar is first observed to respond to IIB a point is chosen arbitrarily along the length of the pillar. A normal is drawn through this point perpendicular to the pillar's length axis, with angular deviation established as θ. At time *t*, θ is assumed to be 0. At even time intervals during the pillar's bending process, the normal is redrawn through the same point and the angular deviation is measured. The resultant bending rate can then be used to evaluate the quality of the pillar's response to IIB. In the case of ordered nanoporous nickel pillars, bending rate was observed to grow during the experiment.

7.4 Discussion

Solid nickel pillars

Previous experiments have demonstrated the capacity of solid metallic pillars to exhibit both homogeneous and point-bending behaviors during IIB. Homogeneous bending is the process where a pillar undergoes a continuous bend along its entire length. In this mode the bending can be considered as elastic deformation, and, in general, the behaviour in this mode is uniform, allowing for a quantitative model to be built and used to analyze and predict the pillar's behaviour and material properties.

Point-bending is a plastic phenomenon, where a pillar bends rapidly and locally at a single preferential point at an arbitrary point along the

pillar with the remainder of the pillar remaining mostly undeformed. Point-bending in multiple points has been observed, but the amount of simultaneous point-bending events in one pillar has never been seen to be above three. Whether a pillar will bend homogeneously or locally depends on the microstructure of the pillar. We have attributed point-bending to microstructural inhomogeneities within a pillar. Conversely, a fully homogeneous pillar will bend homogeneously. We have observed such behaviour in Chapter 5 in a fully amorphised solid aluminium pillar, where amorphisation was induced by ion beam processing. We also expect a monocrystalline pillar to bend homogeneously. On the other hand, point-bending was observed in solid copper pillars where amorphisation did not occur fully and crystalline regions were still present – the pillar underwent preferential bending in these crystalline regions.

In addition, point-bending was observed in fully crystalline solid gold pillars. In the case of copper, point-bending had occurred due to the different IIB dynamics between amorphous and crystalline material, where bending is much more rapid in the crystalline part. In the case of gold, we have attributed point-bending to the polycrystallinity of the pillar, as different crystal orientations allow for varying degrees of ion penetration, and thus an inhomogeneous ion distribution profile will be formed, and from it an inhomogeneous stress distribution which will lead to preferential bending.

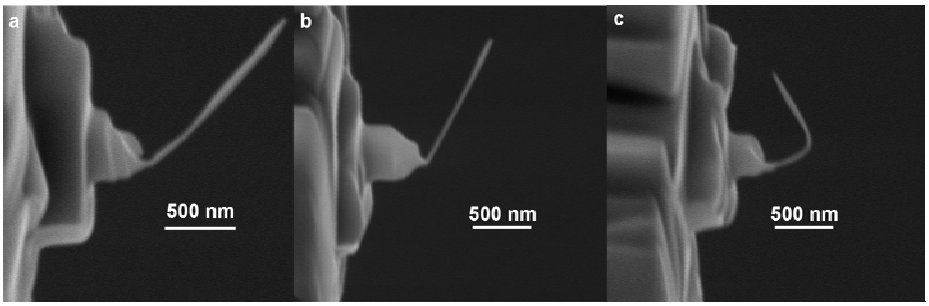

Figure 7.1: Various bending behaviors of solid nickel pillars.

For solid nickel, with its comparatively high displacement energy and stiffness, point-bending comes very late: as can be seen in Figure 7.1, pillars achieve a very high aspect ratio prior to bending. In 1a and 1b, point-bending occurs at the base of the pillar, which we attribute to a fault in the FIB itself – it has been observed that the ion beam will dwell in certain regions longer than others during its scan time. This dwell time will lead to a stronger reduction in diameter in the dwell region and thus a preferential bending around that point. In 1c, however, the bend occurs in the middle of the pillar, and is not as sharp as that observed in 1a and 1b.

This is behaviour similar to that of solid gold pillars, in other words the inhomogeneity comes from the pillar's crystal structure in that particular point. Due to our limited ability to control the microstructure of a solid pillar we are unable to make quantitative judgments on the behaviour of solid nickel pillars.

A strongly homogenized Au pillar has been observed not to bend at all under IIB until moments before the ion beam mills it away completely. Upon reaching an extremely small diameter as a result of ion beam milling, a small bend was observed at the very tip of the pillar, where the diameter was smallest. This had reinforced our statement that crystalline inhomogeneities are the cause of point-bending. If the ion beam fault had not occurred in nickel pillar 1b, it is likely that the pillar would behave in the same way that the aforementioned gold one did.

Ordered nanoporous nickel pillars

Previous experiments on disordered nanoporous Au and Cu have repeatedly demonstrated the increased compliance of porous pillars compared to their solid counterparts. Furthermore, in all cases, disordered nanoporous pillars exhibited homogeneous bending, even if solid pillars made from the same metal showed tendencies towards point-bending. This is a particularly interesting property and we have

attributed this to the interaction dynamics of ligaments in a nanoporous lattice under stress.

Specifically, reports in literature on indentation experiments on nanoporous gold have shown that no long-range stress fields are observed between ligaments. In other words, ligaments not immediately adjacent to each other do not "see" each other, and this causes a weakening of any localization effects and an overall homogenization of the pillar's response to IIB.

We expect Ni to follow the same overall behavioral pattern – through homogenization induced by the nanoporousity in the system the pillar will undergo homogeneous bending much more rapidly and continuously than its solid counterpart. It is in our interest to investigate potential changes in bending behaviour that ordering of microstructure can cause. For this purpose we have used ordered nanoporous nickel produced through templating [5].

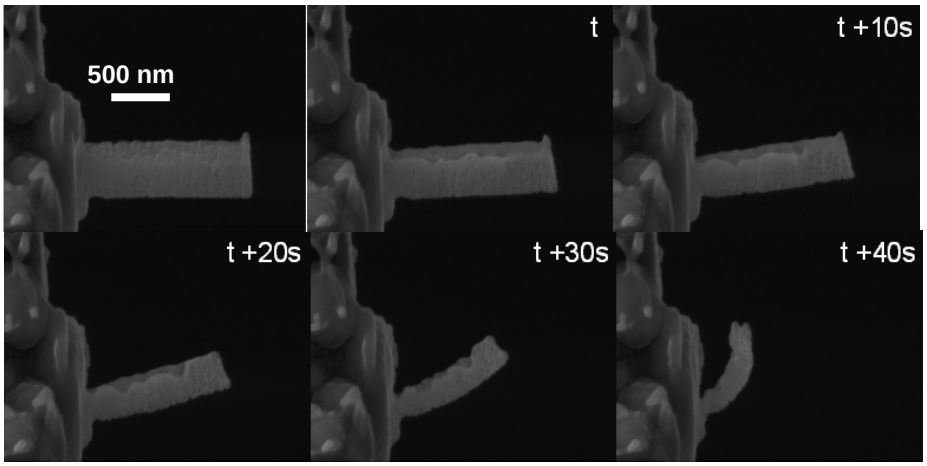

Figure 7.2: IIB of an ordered nanoporous Ni pillar. Example areas of preferential reduction of diameter are highlighted.

The pillar shown in Figure 7.2 displays, for the most part, a homogeneous bend. Areas of preferential reduction in diameter and pitting are observable, and are likely due to imperfections in the source

material – voids can be present in the pillar as the inverse templating process of production of the ordered nanoporous nickel is not perfect.

Specifically, the inverse templating process relies on the complete infiltration of a material into a template such that, once the template is removed, the result is a three-dimensional "negative" of the template. It stands to reason that any flaws with the infiltration process will lead to flaws in the end product. In this particular case of nickel inverse templating using a gyroid template, issues may arise due to surface tension preventing full infiltration across the entire template such that when plating is induced, areas where no infiltration had occurred will not undergo plating and, thus, when the template is removed, would result in a void.

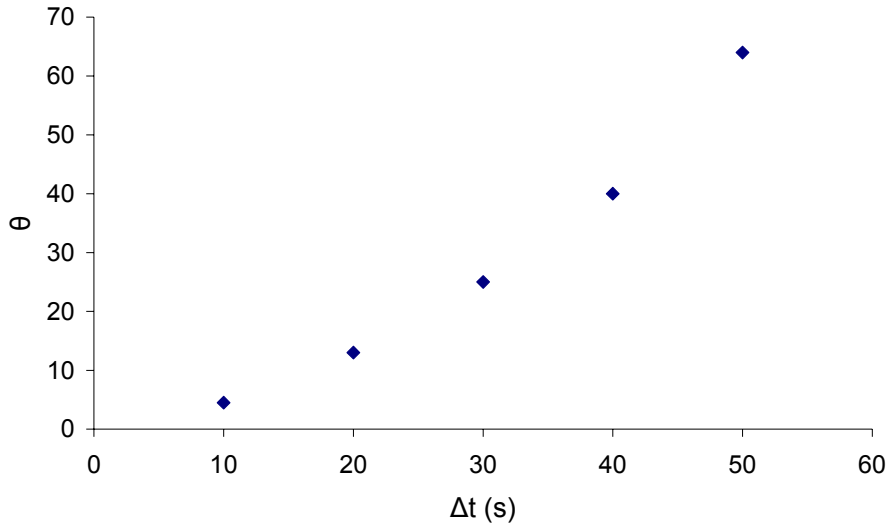

Figure 7.3: Nanoporous Ni pillar bending rate under IIB.

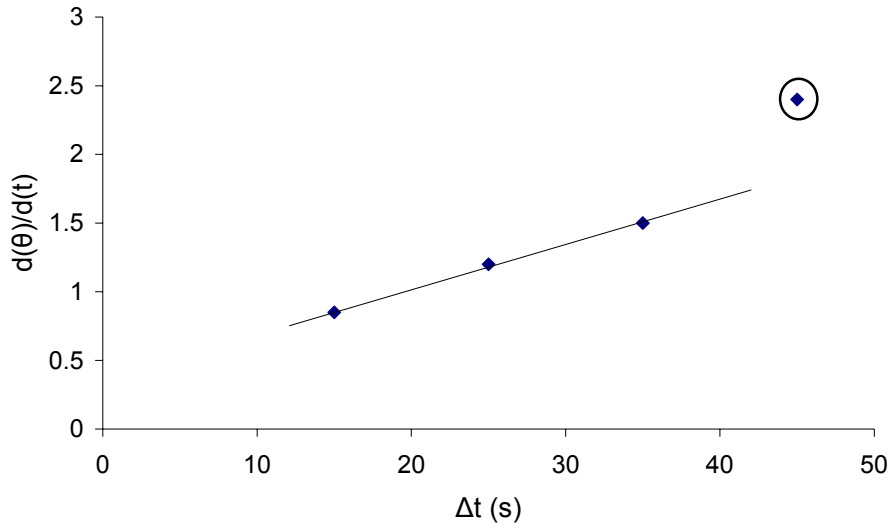

Figure 7.4: Growing bending rate of the nanoporous Ni pillar under IIB.

The same can be achieved if regions might form within the template where all of the metal within a particular volume of plating solution might deposit preferentially – for example, near the surface of the template due to inhomogeneous nucleation - and thus deplete the solution deeper within the template of nickel, preventing plating from occurring. In Figure 7.2, then, pitting observed in the pillar may come from the exposure of voids within the microstructure.

We arrive at Figure 7.4 by taking the deflection angle θ away from the normal, where the normal is defined as 0 when the pillar has not responded to IIB, at even time intervals Δt. Figure 7.3 shows the same typical growing bending rate that has been reported during the IIB of Al and Cu. No meaningful difference was observed in homogeneous bending behaviour across a series of pillars. This effect has been attributed to the reduction of diameter due to ion milling.

Experiments on nanoporous Au and Cu have shown that pillars under IIB, when being homogeneously, show two different behaviors depending on how quickly the pillar responds to IIB. In the case of Au,

the pillar begins to bend quickly and undergoes a large deformation within 20 seconds. With Cu, however, the pillar only achieves a similar deformation by up to one minute. This is meaningful due to the milling effect of the ion beam that induces a gradual and linear over time reduction of a pillar's diameter – this diameter reduction leads to a strengthening of the vacancy-rich/neutral bilayer effect that leads to bending. As the milling rate is approximately the same for all metals investigated, we have concluded that a quick response to IIB will yield a linear bending rate due to effects of milling being low, whereas a slow response gives more time for milling to take place and thus bending rate will more accurately fit a power law.

A linear rate change correlates with the linear reduction of diameter due to milling. For the most part, this holds true for the behaviour of the nanoporous Ni pillars, and only the end of the IIB response is different. This deviation is due to the pitting observed towards the end of the IIB process, which would lead to an inhomogeneous bending response. Therefore, the end part of the IIB deformation in the nanoporous nickel pillar cannot be used for quantitative analysis. However, we observe that no significant pitting develops in the first 25 seconds, and, by association, bending is homogeneous and the power law fit holds. By using the results from the first 25 seconds, we can evaluate the mechanical properties of the pillar.

Atomic considerations

We have used the Kinchin-Pease model to evaluate the total amount of vacancies formed for a given ion flux. Using Embedded Atom Potential (EAM) modeling we were able to determine the contribution of a single vacancy to the lattice stress of an infinitely large crystalline lattice. By back-calculating empirical data acquired in experiments with aluminium, we have developed a "black-box" adjustment that considers that not all vacancies contribute equally to the bending stress, but, rather, mutually compensate, with only a small fraction contributing to stress.

The adjustment assumes that vacancies will behave in a similar manner across all metals investigated – Au, Al, Cu and Ni – and makes EAM data compatible with the empirical data acquired in the FIB. With vacancy count known and the contribution of each vacancy to compressive stress, by measuring the pillar's strain at a known time, we can use Hooke's Law to evaluate the pillar's Young's Modulus.

We take an ordered nanoporous Ni pillar under IIB for 20 seconds (Figure 7.2). We can use the Kinchin-Pease model to estimate the amount of vacancies formed due to ion impacts [6]. With a known displacement energy of 23eV [7] we calculate that approximately 652 vacancies are formed per ion impact in nickel. Assuming a constant ion current of 10pA and constant ion energy of 30kV, we can estimate $1.4 \cdot 10^{10}$ defects per second in nickel. At 20 seconds this becomes $2.8 \cdot 10^{11}$ defects total.

As seen in our previous experiments with Al (Chapter 5) a very low amount of defects contribute to the formation of the compressive stress field if EAM values are considered. We assume that the process of vacancy formation is the same for all metals investigated, so only $2 \cdot 10^5$ defects will contribute to the compressive stress field. Of these, the number of defects at σ_{max} (d/2 where d is 20nm) is $1 \cdot 10^4$. According to EAM, a single vacancy induces a stress of $2.32 \cdot 10^5$ Pa. Assuming a linear contribution of point defects to stress, the total stress becomes 2.3GPa.

At 20 seconds the dimensions of the nanoporous Ni pillar are as follows: $\delta(x)$ is 318nm, w is 321nm, x is 1112nm (see Figure 7.2). Ion penetration depth d into Ni is 20nm. Using the beam-bending model presented in chapter 4, this results in a modulus value of 2.44 GPa.

This is far lower than the known value for the stiffness of nickel at around 200GPa, and is also far lower than expected when compared to the stiffness reduction seen in disordered nanoporous Au and Cu.

Scaling laws have been shown to be able to make accurate predictions of the value of a nanoporous metal's modulus value [1]. As it is known that nanoporous ordered Ni is an open-celled foam, its modulus can be expressed as

$$E = C_2 E_s (\rho_{np} / \rho_s)^n \qquad (7.1)$$

Where E_s is the modulus of solid Ni and (ρ_{np} / ρ_s) is the relative density of the foam . C and *n* are proportionality and density constants respectively that describe cell geometry and elastic cell deformation, and experimental data obtained from open-cell foam materials has shown that the constants can usually be well-fitted by C_2 =1 and *n* = 2. Assuming that our nanoporous ordered Ni has a relative density of 50% and using the modulus of Ni at 200GPa, the scaling law predicts a modulus value of 40 GPa.

A very large discrepancy is observable between the modulus prediction of the nickel nanopillar from scaling laws and from IIB projections. This is due to the contribution of inconsistent microstructure, i.e. whilst we assume a completely homogeneous pore-ligament microstructure, in earlier chapters we have demonstrated that voids can be present in the gyroidal nickel; to the contribution of a not fully homogeneous bend, as we can see that the pillar in figure 7.2 does not have a fully continuous bend profile, which suggests preferential bending, likely at its base. The most interesting contribution, however, comes from the ordering of the pillar's nanoporous microstructure.

Introduction of anisotropy leads to significant behaviour changes in a material. For the purposes of this discussion, we can consider a disordered nanoporous material as isotropic due to the implied random orientation of the pore-ligament microstructure, where a pillar made from such a material would respond in the same way regardless of the pillar's orientation to the ion beam and, consequently, regardless of the face in which the resulting compressive force is generated.

This is not the case for the three-dimensionally ordered nanoporous nickel. We initially assume that the gyroidal microstructure is monocrystalline – in other words, the gyroidal unit cell is constantly oriented throughout the entirety of the pillar. This assumption is necessary as any polycrystallinity in the gyroid moves the pillar towards isotropic behaviour. This is to say that enough sufficiently small unit cell grains with each having their own particular orientation would sum up to a randomly-oriented material. In a fully isotropic material with a particular orientation or texture an applied force will have varying effects depending on the relative orientation of the force to the sample. We postulate that the pillars investigated in this study were able to bend along a particular preferential deformation direction, hence the unexpectedly low effective stiffness.

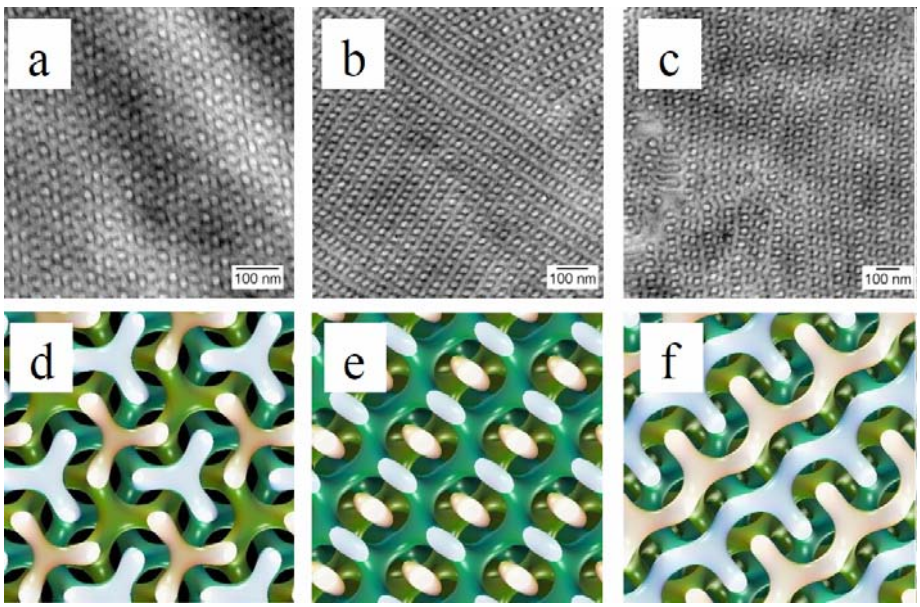

Figure 7.5: Bright-field TEM of polystyrene gyroid template. Panels a, b and c represent the <111>, <110> and <211> projections respectively. Panels d, e and f are the appropriate TEM-simulated projections, shown for comparison [5].

Cross-sections through the gyroid microstructure show very characteristic patterns in several crystalline projections, as shown in Figure 7.5. The typical gyroid microstructure exhibits planes with varying degrees of packing, with less dense planes offering more degrees of freedom for deformation as opposed to more dense planes. In this manner, by choosing a specific deformation orientation to align with a specific plane, the deformation properties of a nickel pillar can be made to vary.

7.5 Conclusions

We have observed the behaviour of both solid and ordered nanoporous nickel pillars produced through reverse templating when exposed to a 30kV ion beam. The behaviour of both was consistent with previous experiments on similar materials and microstructures – point-bending was observed in solid nickel and homogeneous bending was observed in porous nickel. Discrepancies were present, however – areas of preferential diameter reduction were seen in the nanoporous nickel, and we postulate that these are present due to large voids already being present in the source material prior to pillar formation as we have shown in Chapter 3. However, this preferential diameter reduction did not influence the homogeneous bend of the nickel pillar until the very final stages of the process. Being able to attribute homogeneity to the bending behaviour of the nanoporous nickel pillar allowed us to use IIB as a characterization tool by comparing the behaviour of the pillar to that of our previous experiments, where the Kinchin-Pease model was used in conjunction with embedded atom potential modeling and Hooke's Law to estimate the pillar's Young's modulus. The result was far lower than the value for the Young's modulus of bulk nickel, and we attributed this phenomenon to the anisotropy present in the nickel pillar. Nanoporous gyroidal nickel pillars with clear ordering throughout the entire pillar can be seen in TEM micrographs in Chapter 3.

7.6 References

[1] J Biener, A M Hodge, A V Hamza, L M Hsiung, J H Satcher, J. Appl. Phys. 97, 024301 (2005)

[2] B Van Eerdenbrugh, G Van den Mooter, P Augustijns, International Journal of Pharmaceutics 364 (2008) 64-75

[3] C C Koch, *Rev. Adv. Mater. Sci.* 5 (2003) 91-99

[4] Y Yan, Z Hu, X Zhao, T Sun, S Dong, X Li, Small 2010, *6*, No. 6, 724-728

[5] I Vukovic, Block Copolymer Template-Directed Synthesis of Well-Ordered Metallic Nanostructures (Groningen University Press, Groningen)

[6] G H Kinchin, R S Pease 1955 Rep. Prog. Phys. 18 1

[7] P Jung, Phys. Rev. B, 23, 664 (1981)

Chapter 8

SUMMARY AND OUTLOOK

8.1 Summary

The nanoporous metal foam sits at the centrepoint of a myriad engineering disciplines coming together to form a highly versatile material effective in a variety of applications. As a porous material, it boasts excellent surface-area-to-volume ratio and attractive commercial properties such as energy absorption capacity and being low-cost to produce. As a nanostructured material, it offers the properties often sought-for in industries that can make use of them: electrical and thermal conductivity, strong capacity as catalyst and catalyst carrier, potentially exploitable optical properties, etc. As a metal it boasts the robust mechanical properties required of a structural material: strength, impact and resistance to age and the environment.

As far as functional properties are concerned modern actuating materials – materials that have the capacity for controlled deformation under an applied electric current – would be used as moving parts in micromechanical devices, and nanoporous metals make the ideal candidates for such roles. Actuation in nanoporous metals is permitted by the fact that injection of charge into a metal causes a change of surface charge states, which is amplified due to the significant fraction

of surface-to-volume present in a nanoporous metal which ultimately leads to measurable deformation.

The typical nanoporous foam is produced through dealloying, and is thus considered to be disordered. A fascinating question arises on whether an ordered foam microstructure would have a meaningful effect on actuation-based deformation. After all, crystalline metals have preferential deformation directions and the same principle might apply to an ordered nanoporous metal. The initial purpose of this work was to investigate this very possibility.

Indeed, while a single-crystalline structure might well experience amplification in actuation, the reality of the situation is that the templates that are used in the production of ordered nanofoams themselves nucleate across a series of separate events, forming ordered unit cell grains, much akin to a bulk polycrystalline material. As a result, the nanoporous foams produced from these templates are themselves polycrystalline. As ordered grains have random orientations relative to each other, the sum effect is a randomization of the microstructure, leading to a statistical self-averaging property. Essentially, with the production method produced it is impossible to produce ordered nanoporous metals that can give a concrete demonstration of any amplification of actuation that ordering can offer.

Matters are different at the nanoscale, however. By using a Focused Ion Beam apparatus (FIB) it is possible to shape submicron-sized features. In other words, it is possible to recover full anisotropy by milling out features that are smaller than the grain size in a foam. The characterization of such features, then, requires an alternative approach.

Mechanical indentation by means of a Hysitron picoindenter *in-situ* inside a TEM was shown to lack the necessary accuracy for the sample size used, coupled with the uncertain orientation of the sample itself. Instead, a mostly unexplored technique that yet offered a lot of potential was used: Ion-Beam-Induced-Bending (IIB). IIB was shown

to have a high accuracy and reproducibility using nothing more than the FIB apparatus. It also had the added benefit of requiring no mechanical contact between a deformation apparatus and the sample: under IIB a sample bends due to the influence of the incident ion beam.

As IIB is still considered in its infancy, and many of its aspects are still unknown, a broad series of experiments was carried out to develop a comparative baseline for the technique. The behaviour of solid, disordered nanoporous and ordered nanoporous metals under IIB was examined and documented and, with relationships established between ion fluence, bending strain, bending rate and sample dimensions, predictions were made about the Young's modulus of submicron-sized nanoporous pillars.

We found that IIB provides an accurate indication of the modulus of nanoporous gold, where bending occurs quickly. We have observed that a rate-based phenomenon is present during IIB, where the progressive reduction in diameter due to ion milling accelerates bending rate and thus a resultant modulus prediction may deviate from actuality. This phenomenon occurs in stiffer metals, where a longer exposure is required for bending to occur. In general, however, we have observed that the induction of disordered porosity reduces the stiffness of a metal by a factor of two to four. The case was different for ordered porosity: in an ordered nanoporous nickel pillar an order of magnitude reduction in stiffness was observed. This effect stemmed from the anisotropy present in the pillar, where preferential deformation directions across loosely-packed areas would permit the pillar to deform more easily than its disordered counterpart.

8.2 Outlook

While we have taken steps to demonstrate the viability of IIB as a tool for mechanical characterization, the process still has many unknowns. Currently, a true deterministic model is lacking to show the relationship

between the ion beam and the resultant compressive force induced by vacancies. An investigation is due to learn and express the relationships between multiple point defects how much of their individual strain is canceled out and how much of it aggregates into a sample-wide compression. The power-law effect of bending acceleration due to diameter reduction is also not fully considered when making Kinchin-Pease calculations. In situations where bending becomes rate-dependent, a stronger measuring approach should be used to measure deformation of a pillar in the elastic regime before plastic effects take place. Should all these considerations be addressed, IIB has the potential to be used in many applications where extreme precision is required in the deformation of submicron-sized features. Additionally, it can be used as a first-step method of measuring mechanical properties of such features, as no equipment is required to perform IIB beyond the FIB apparatus itself and the results yielded can be quite accurate.

Considering the use of ordered nanoporous metals for actuation, it is first necessary to be able to produce single-crystalline templates, such that the final product would also have a singular grain orientation. A more reliable infiltration process is also desired such that no voids are present in an ordered nanoporous foam after template removal. For the former, procedures for forming single-crystalline metals for aerospace applications could be considered and adapted. For the latter, different carrier solvents and plating conditions can be considered to ensure a uniform plating procedure.

Chapter 9

ACKNOWLEDGEMENTS

I am already quite certain that I will never be able to express my gratitude enough to all those around me for these past four years. It is woefully insufficient to call these doctoral studies a mere chapter in my life: they are a full book unto themselves, and all of you deserve a chapter of your own in that book. Unfortunately, my greatest opponent at this time is page count, so perhaps that book is a story for another day.

I would first like to thank my thesis supervisor Professor Jeff Th. M. De Hosson. Not only for giving me the chance to participate in this unusual project in the first place, but for giving me the opportunity to learn incredible science from you and from myself. More, even, than that: *challenging* me to keep up with my colleagues and making me keenly aware of what shortcomings I need to overcome in myself. I do not know if I met expectations – goodness knows I would have done many, many things differently in this project were I sent back in time – but I can only keep expressing my gratitude for the faith you have in the so lively and exciting MK group.

I wish to thank Eric Detsi, my most literally closest colleague for the majority of these four years. Whether you intended to or not, you set a very high bar for me to meet, and your constant interest in my work made me strive to work harder and better. In this way, I feel, you will be a positive influence wherever you might go, and I am grateful, no

matter how foolish it may sound, to have been your colleague and equal for all this time. I wish you all the best in America!

I wish to thank Ivana Vukovic, with whom I have been working for the longest time in this interdisciplinary research project. Your thorough work and diligence are an inspiration, and the sheer amount of results you were able to – seemingly effortlessly – present at every ZIAM meeting was mind-boggling. What I cannot help but admire most, however, is your ability to meet every day with a smile. I certainly do not know if you faced difficulties or pressure in your work, as the impression you always gave is one of gliding along smoothly without so much as a stumble. Working with you I always felt that things would be all right in the end.

I wish to thank the members of the reading committee, Drs. Patrick Onck, Hans De Raedt and Petra Rudolf, for taking your time to evaluate my thesis.

I wish to thank the other PhD students in the ZIAM research group: Alex Zinchenko and Siva Saane. Your feats with code and equations gave an unparalleled amount of perspective on our project, and gave me a first-hand look at how a single research proposal can branch out in completely different directions. Of course, I must also thank both of you again: Alex for your 3D gyroid models which have often served as excellent illustrations for many purposes, and Siva for your insight on EAM that gave my research a needed push in the right direction.

I would be remiss to mention the ZIAM Foam group and not thank Patrick Onck, Katja Loos, Hans De Raedt and Gerrit ten Brinke. Each one of you offered an astounding volume of cross-disciplinary insight that really gave life to our project during our monthly meetings. Seeing such a wide set of knowledge bases come together in one MK VIP room kept reminding me that science is not an archipelago but a single, indivisible continent.

I wish to thank Paul Bronsveld for all your help and advice with the arc furnace, the electropolishing equipment and the TEM, amongst many other things. Working with you has been a pleasure every time!

I wish to thank Oleksii Kuzmin for our long hours spent at the FIB and TEM. You are the first who suggested making pillars out of our foams and, perhaps, without you I would never have learned about IIB and would be sitting here without half a thesis! And, of course, thank you for all your help outside of work. My best wishes and I hope for your full recovery.

I wish to thank Mikhail Dutka, who has been a well of knowledge regarding just about every piece of equipment I have used in the past four years. Thank you for your insight and certainly thank you for the variety of courses you have given me.

Thank you to all my usual suspects: Willem van Dorp, Enne Faber, Catalina Mansilla-Sanchez, Diego Martinez-Martinez, Jintao Shen, Winand Slingenbergh. Our time together was well-spent, and I always marvel at how easily all of you can hold on to whatever odd conversation topic I bring up. Most importantly, thank you for putting up with me when I was at my worst. I am hardly graceful under pressure and can easily lash out but you did not judge and offered your support regardless of anything. I have learned much from every single one of you, and I certainly hope that we will remain close regardless of any distance that might come between us.

I wish to extend my thanks to everyone else in the MK group, past and present, as well: Ismail Hemmati, Tony Kazantzis, Ondrej Nenadl, Vašek Ocelík, Yutao Pei, Anatoly Turkin, David Vainchtein and Willem-Pier Vellinga. The MK group is always full of intelligent and lively people from many corners of the world. I feel proud to have worked in such an excellent community.

I wish to thank Selma Detsi for the cover design.

I wish to thank Tamalika Banerjee for your help and coordination for my work in the cleanroom. It was an illuminating experience.

I wish to thank Maarten Vervoort for your precise and untiring work with quartz.

I wish to thank Johan Holstein for your close cooperation on the more daring parts of my experiments.

I wish to thank Hok Man Tang, Alan Parish and Thorsten Stechert. Knowing you were all hard at work on your own PhDs reminded me to pull my weight. I might be finishing before all of you, but I hope that will only inspire you to confidently clear the last stretch. Thank all of you for always being there when I needed someone to talk to, and for your company on our numerous mutual visits. May we never become strangers.

Я желаю выразить благодарность своим родителям, как бы ни было это сложно в столь нескольких словах. Вы мне дали много, очень много, но самое главное, за что я благодарен, это сам шанс учиться и работать, самому узнавать и осмыслять. Я не мог бы пожелать большего.